MATHEMATICAL MODELING OF MASS TRANSFER IN MICROVASCULAR WALL AND INTERSTITIAL SPACE

by

Daekyung Kim

Dissertation submitted to the Faculty of the Graduate School of the New Jersey Institute of Technology in partial fulfillment of the requirement for the degree of Doctor of Philosophy
1991

APPROVAL SHEET

Title of Dissertation: Mathematical Modeling of Mass Transfer in Microvascular Wall and Interstitial Space

Name of Candidate : Daekyung Kim
Doctor of Philosophy, 1991

Dissertation and Abstract Approved:

Dr. Piero M. Armenante — Date

Assistant Professor
Department of Chemical Engineering,
Chemistry and Environmental Science

Dr. Ching-Rong Huang — Date

Dr. Dana E. Knox — Date

Dr. David Kristol — Date

Dr. Walter N. Durán — Date

VITA

Name : Daekyung Kim

Degree and Date to be Conferred: Doctor of Philosophy, May 1991

Secondary Education : Seolabeol High School, 1978

Collegiate Institutions Attended	Dates	Degree	Date of Degree
Seong Kyun Kwan University	3/78-2/82	B.S.	Feb. 82
Seong Kyun Kwan University	3/82-2/84	M.S.	Feb. 84
New Jersey Institute of Technology	9/86-5/91	Ph.D.	May 91

Major: Chemical Engineering

Publications: Kim, D., Armenante, P. M., and Durán, W. N. Calibration of microvascular and tissue concentration of fluorescent tracers by digital image processing. Paper accepted for presentation at 76th annual meeting of *Federation of American Societies for Experimental Biology*. April 1991.

Armenante, P. M., Kim, D., and Durán, W. N. Experimental determination of the linear correlation between in vivo TV fluorescence intensity and vascular and tissue FITC-Dx concentrations. Paper accepted for publication. *Microvascular Research* (in press).

Kim, D., Armenante, P. M., and Durán, W. N. Mathematical Modeling of mass transfer in microvascular wall and interstitial space. *Microvascular Research.* **40**, 358-378 1990.

Kim, D., Armenante, P. M., and Durán, W. N. Convective-diffusive mass transfer across microvascular vessels. Paper accepted for presentation at 1990 annual

meeting of *American Institute of Chemical Engineers.* November 1990.

Kim, D., Armenante, P. M., and Durán, W. N. Mathematical modeling of mass transfer in microvascular wall and interstitial space. Paper accepted for presentation at 75th annual meeting of *Federation of American Societies for Experimental Biology.* April 1990.

Kim, D., Armenante, P. M., and Durán, W. N. Mathematical modeling of macromolecule transfer across microvascular vessels. Paper accepted for presentation at meeting of *American Institute of Chemical Engineers-North Jersey Section.* April 1990.

Kim, D., Armenante, P. M., and Durán, W. N. Modeling of macromolecule transfer in microvessel. Paper accepted for presentation at 16th annual *Northeast Bioengineering Conference.* March 1990.

Kim, D., Armenante, P. M., and Durán, W. N. Transient analysis of mass transfer across microvascular wall and tissue. Paper accepted for presentation at 1989 annual meeting of *American Institute of Chemical Engineers.* November 1989.

Position Held:

1988 - 1991: Teaching Assistant

Department of Chemical Engineering, Chemistry, and Environmental Science
New Jersey Institute of Technology
Newark, New Jersey

ABSTRACT

Title of Dissertation : Mathematical Modeling of Mass Transfer in Microvascular Wall and Interstitial Space

Daekyung Kim : Doctor of Philosophy, 1991

Dissertation directed by:

Piero M. Armenante, Assistant Professor, Department of Chemical Engineering, Chemistry, and Environmental Science, New Jersey Institute of Technology

Walter N. Durán, Professor, Department of Physiology, University of Medicine and Dentistry of New Jersey-New Jersey Medical School

The dynamics of macromolecular transport across the microvascular wall and into the adjoining interstitial space was studied in the hamster cheek pouch using intravital fluorescence microscopy in combination with digital image processing. Fluorescein isothiocyanate-labeled dextrans (FITC-Dx) of 70,000 and 150,000 daltons were used as tracers. In each experiment, the time-dependent extravasation of FITC-Dx from a leakage site in a blood vessel was videotaped for about 2 hours. The macromolecular transport from individual microvessels was quantified by digital video-image processing. Histograms of the light intensity distributions for selected fields at various times were obtained and then converted to the interstitial FITC-Dx concentrations using a newly developed *in vivo* calibration procedure.

A one-dimensional unsteady-state model was developed to describe the dynamics of the macromolecular transport. Both molecular

diffusion and convective transport in the microvascular wall as well as in the interstitial space were accounted for in the model.

The experimental data were correlated using a non-linear regression algorithm incorporating the mathematical model in order to determine the diffusivity coefficients and average fluid velocity terms in the two regions. The diffusivity coefficients for FITC-Dx 70 were found to be $0.90\pm0.04\times10^{-11}$ cm^2/s in the microvascular wall, and $1.29\pm0.05\times10^{-8}$ cm^2/s in the interstitial space. The average fluid velocity term in both regions was found to be $2.05\pm0.05\times10^{-8}$ cm/s. The corresponding transport parameters for FITC-Dx 150 were $0.27\pm0.02\times10^{-11}$ cm^2/s, $0.55\pm0.05\times10^{-8}$ cm^2/s, and $1.71\pm0.48\times10^{-8}$ cm/s, respectively.

Using a similar experimental procedures, the extravasation of FITC-Dx 70 and FITC-Dx 150 was experimentally determined after a 5-minute topical application of calcium ionophore A23187 (7×10^{-7} M) which produced a transient increases in the rate of blood-tissue transport of large molecules. In this case, the diffusivity coefficients and average fluid velocity terms were found to be approximately two times and eight times higher, respectively, than the corresponding parameters obtained in the absence of the calcium ionophore A23187.

The diffusivity coefficients and average fluid velocity terms so obtained were then used to quantify the role of the diffusive and convective mechanisms in the total solute flux through the microvascular wall and into the adjoining interstitial space. The macromolecular transport in the microvascular wall was found to be the limiting transport mechanism for the entire process. Within the

microvascular wall, it appeared that the molecular diffusion mechanism dominated over convective transport in all the cases considered. However, in the presence of the calcium ionophore A23187 the convection term increased about three times if compared with the corresponding value in the absence of it. Within the interstitial space, diffusion appeared to be the dominating transport mechanism for all cases.

It is expected that the proposed model and calibration procedure will be used in the future to describe the dynamics of macromolecular transfer across the microvascular wall and into the interstitial space on the basis of both molecular diffusion and convective transport mechanisms, thus contributing to the solution of the controversy regarding the nature of the transfer mechanism controlling the transport of macromolecules in living systems.

ACKNOWLEDGEMENTS

I would like to express my gratitude and a million thanks to the following people who have helped me throughout this work.

Dr. Piero M. Armenante, my advisor, for all his guidance, support and encouragement. His friendship will always be greatly appreciated and remembered.

Dr. Walter N. Durán, for his suggestions, criticism, and guidance throughout this work. I thank him for letting me be part of his research group.

Dr. David Kristol, for the initial suggestion which led to the selection of this research area and for the continued interest.

Dr. Hiroshi Yasuhara, for discussions and valuable suggestions.

Aline Tomeo and Mike FitzPatrick, for technical help and assistance.

Department of Physiology, University of Medicine and Dentistry of New Jersey, for letting me use department equipments and facilities.

My parents and brother, for the scarifies of their lives with the unconditional love.

Finally, my wife, Mira, for believing in me when I was not believing in myself and for being there when I needed her most.

TABLE OF CONTENTS

Chapter		Page
	ABSTRACT	i
	ACKNOWLEDGMENTS	iv
	LIST OF TABLES	vii
	LIST OF FIGURES	viii
1.	INTRODUCTION	1
	1.1. Overview of the Problem	1
	1.2. Objectives of This Work	3
2.	LITERATURE REVIEW	5
3.	MODELING OF MACROMOLECULAR TRANSPORT	9
	3.1. Model Development	9
	3.2. Analytical Solution for the Model	15
	3.3. Numerical Solution for the Model	25
	3.4. Application of the Model to Microvascular Transport	28
4.	EXPERIMENTAL METHODS	35
	4.1. Characteristics of the Macromolecular Tracers and Optical System	35
	4.2. Adjustment of Camera Gain and Threshold Value (KV)	37
	4.3. Animal Preparation	37
	4.4. Experimental Protocol for the Determination of the Calibration Curve	39
	4.5. Experimental Protocol for Macromolecular Transport Studies	43
	i) Macromolecular Transport Studies in the Absence of Calcium Ionophore A23187	43

ii) Macromolecular Transport Studies in the Presence of Calcium Ionophore A23187 44

4.6. Picture Digitization and Development of Mean Gray Scale 44

5. RESULTS 48

5.1. Measurement of Tissue Density 48

5.2. Calibration Curves 48

5.3. Macromolecular Transport Studies 50

6. DISCUSSION 71

6.1. Calibration Procedure 71

6.2. Macromolecular Transport 73

6.3. Interpretation of Transport Parameters 79

i) Pore Theory 79

ii) Fiber-Matrix Theory 82

7. SUMMARY AND CONCLUSIONS 85

REFERENCES 88

APPENDIX 94

A. Proof of the Real Nature of All Roots of Equation (3.25) 95

B. Analysis of the Roots of the Equation (3.25) 98

C. List of Computer Programs 103

D. Data for Digital Image Analysis and Calibration Experiments 123

LIST OF TABLES

Table		Page
4.1.	Physicochemical parameters of the test molecules	36
5.1.	Plasma concentration of FITC-Dextrans	55
5.2.	Results from the digital image analysis of the experimental data. Tracer:FITC-Dx 70	56
5.3.	Results from the digital image analysis of the experimental data. Tracer:FITC-Dx 150	57
5.4.	Results from the digital image analysis of the experimental data. Tracer:FITC-Dx 70 with calcium ionophore A23187	58
5.5.	Results from the digital image analysis of the experimental data. Tracer:FITC-Dx 150 with calcium ionophore A23187	59
5.6.	Parameters used in the determination of transport coefficients from the experimental data	63
5.7.	Sensitivity analysis of the RNLIN program to the initial guesses for D1, D2, and V	65
5.8.	Values of the transport parameters obtained from the regression analysis	69
6.1.	Relative contribution of molecular diffusion and convective transport to the overall transport process	75
6.2.	Effective permeability of macromolecules in microvascular wall	77
6.3.	Comparison of the diffusion coefficients obtained in this study with the results obtained by other workers	78
6.4.	Comparison between the pore theory and the fiber-matrix theory using the diffusivity coefficients in the microvascular wall found in this study	81

LIST OF FIGURES

Figure		Page
3.1.	Schematic diagram of the microvascular wall-interstitial space system used in the development of the model	11
3.2.	Bromwich path for contour integration	20
3.3.	Concentration profiles for selected values of the parameters ($D_2 >> D_1$)	29
3.4.	Concentration profiles for selected values of the parameters ($D_1 >> D_2$)	29
3.5.	Concentration profiles for selected values of the parameters ($\chi_1 >> \chi_2$)	30
3.6.	Concentration profiles for selected values of the parameters ($\chi_2 >> \chi_1$)	30
3.7.	Comparison between analytical and numerical solutions for selected values of the parameters ($D_2 >> D_1$)	32
3.8.	Comparison between analytical and numerical solutions for selected values of the parameters ($D_1 >> D_2$)	32
3.9.	Comparison between analytical and numerical solutions for selected values of the parameters ($\chi_1 >> \chi_2$)	33
3.10.	Comparison between analytical and numerical solutions for selected values of the parameters ($\chi_2 >> \chi_1$)	33
4.1.	Schematic digram of the experimental system	38
4.2.	Preparation of the hamster cheek pouch	40
4.3.	Determination of reference point	47
5.1.	Mean gray level by video-image processing versus tissue concentration of FITC-Dx 150 using a 32x objective and gain=4	49

5.2. Time course of the FITC-Dx extravasation. Pictures were taken at 2, 20, 40, and 60, minutes after tracer injection 51

5.3. Time course of the FITC-Dxs concentration in plasma 54

5.4. Tissue concentration-time profiles for FITC-Dxs and calcium ionophore A23187 60

5.5. Comparison between model prediction and experimental data for extravasation of FITC-Dx 70 66

5.6. Comparison between model prediction and experimental data for extravasation of FITC-Dx 150 66

5.7. Comparison between model prediction and experimental data for extravasation of FITC-Dx 70 with calcium ionophore A23187 67

5.8. Comparison between model prediction and experimental data for extravasation of FITC-Dx 150 with calcium ionophore A23187 67

5.9. Cumulative amount of macromolecule which has extravasated in a given period of time 70

5.10. Mass flux vs. time 70

CHAPTER 1

INTRODUCTION

1.1 Overview of the Problem

The determination of the parameters describing transvascular macromolecular transport is critical for our understanding of the mechanisms which regulate fluid and protein balance in normal and pathological states, as well as for the development of physiologically-based pharmacokinetic models. In principle, two mechanisms can be considered in the process by which macromolecules are transported between blood and interstitial space, namely, bulk fluid movement under the action of hydrostatic pressure gradient (convection), and molecular transport under the action of a concentration gradient (diffusion).

The exact mode of macromolecular transfer across the microvascular wall and into the interstitial space, and the relative importance of convective transport and diffusive transport in specific physiological states is a matter of controversy. Convection was proposed to be the dominant mechanism of macromolecular transfer by several investigators (Arfors *et al.*, 1979; Haddy *et al.*, 1972; McNamee and Staub, 1979). Numerous other investigators, however, contended that macromolecular transfer occurs primarily by diffusion (Renkin *et al.*, 1977; Paaske, 1982; Sejrsen *et al.*, 1985). Most of these studies were carried out by collecting whole-organ lymph and determining the concentration of a tagged protein or a tracer. Whole-organ lymph, however, may not be representative of the ultrafiltrate which is transported through the

microvessel wall (Taylor and Granger, 1983). Moreover, this technique cannot be used to study the localization of the escape of various solutes out of the microvessels and their detailed behavior within the interstitium.

The introduction of digitized fluorescein angiography (Wiederhielm *et al.*, 1973) has helped to further characterize the quantitative transvascular transport. In most of the studies based on this technique (Gerlowski and Jain, 1986; Baxter *et al.*, 1987; Bekker *et al.*, 1989), the convective terms in the convective-diffusive equations have been ignored. In addition, the experimental techniques used to obtain the calibration curve for the determination of the interstitial tracer concentration may have introduced some inaccuracy (Fox and Wayland, 1979; Nugent and Jain, 1984; Ley and Arfors, 1986). Therefore, the effective permeability coefficient (representing a combination of diffusive and convective components) calculated in many of these studies, could have been affected by the use of a simplistic mathematical model and by the inaccuracy associated with the calibration curve.

In a number of recent studies, calcium ionophore A23187 has also been used to increase the permeability of macromolecules across the microvascular wall. In the postcapillary venules of a number of mammalian microvascular beds, the initial increase in transvascular flux of macromolecules and water following the application of the calcium ionophore A23187 has been shown to be associated with the formation of gaps between adjacent endothelial cells (Michel and

Phillips, 1984). However, in recent studies using calcium ionophore A23187 (Clough and Michel, 1988; Michel and Phillips, 1984; Curry and Joyner, 1986; Curry *et al.*, 1989) the individual contribution of each transport mechanism when the gaps were open has not been quantified.

2.2 Objectives of This Work

In order to overcome the problems mentioned above, a mathematical model accounting for both molecular diffusion effects and convective transport effects to explain macromolecular transfer across microvascular wall and into the interstitial space, and a calibration procedure for the determination of the interstitial fluorescein isothiocyanate-labeled dextrans (FITC-Dx) concentration were developed in this investigation. In addition, a large number of experiments were carried out to validate the model and to determine the transport parameters.

The major aim of this study was to determine the transport parameters and the role of transport mechanisms of blood-tissue exchange, and to elucidate the effect of calcium ionophore A23187 in the blood-tissue exchange. The specific objectives of the study were:

1. To develop a mathematical model for the analysis of the macromolecular transport. Both molecular diffusion and convective transport in the microvascular wall as well as in the interstitial space were accounted for.

2. To develop a calibration procedure for the relationship between fluorescent intensity and fluorophore concentration *in vivo*. The measured fluorescent intensity using a video-image processing was

converted to the interstitial FITC-Dx concentration at various time.

3. To determine the transport parameters by fitting the experimental data to the mathematical model.

4. To investigate permeability changes after applying calcium ionophore A23187.

5. To quantify the convective and diffusive contributions in the microvascular wall as well as in the interstitial space in the absence and presence of calcium ionophore A23187.

6. To examine the transport parameters in terms existing theories, such as the pore theory and the fiber-matrix theory.

CHAPTER 2

LITERATURE REVIEW

Intravital microscopy utilizing intravascularly injected dyes (Patent blue V, Evans blue, trypan blue, carbon particle, etc.) has been used to study capillary permeability in various transparent tissues for many years (Landis, 1927; Rous *et al.*, 1930; McMaster and Parson, 1939; Branemark *et al.*, 1968). In these studies, the dye becomes bound to plasma proteins and is assumed to trace the movement of macromolecules across the vascular wall. This technique allows one to correlate the macromolecular transport to vessel structure and solute size. Although the technique offers the unique opportunity of visualizing the extravasation of macromolecules *in vivo,* the low contrast of the images so obtained, the requirement for a high concentration of the absorbing dye, and the uncertainties of the degree of binding of these compounds to plasma proteins seriously limit the application of this method (Levick and Michel, 1973).

With the introduction of optical and recording systems designed specifically for photometric evaluations, and with the availability of stable fluorescein isothiocyanate-labeled dextrans (FITC-Dx), the permeability changes of selected microcirculatory fields could be studied using significantly lower concentrations of macromolecular tracer.

This method was used by Arfors *et al.* (1979), and Svensjö *et al.* (1978), who determined the exact locations of FITC-Dx leakage sites. Hulström and Svensjö (1979), and Joyner *et al.* (1979) have

investigated the effects of various inflammatory chemical mediators (bradykinin, histamine, prostaglandins) on macromolecular permeability. More recently, Gawlowski *et al.* (1982), and Gawlowski and Durán (1986) have used intravital microscopy to establish the reversibility of the induced macromolecular leakage. These studies, while advancing significantly the field of microvascular research, were either qualitative or semiquantitative in nature, and could not be utilized for the determination of the transport parameters.

The introduction of digitized fluorescein angiography (Wiederhielm *et al.*, 1973) has helped to quantify transmural molecular transport.

Nakamura and Wayland (1975), and Fox and Wayland (1979) have measured apparent interstitial diffusion coefficients of macromolecules in the mesenteries of the cat and rat. In these investigations, the transport of fluorescein isothiocyanate (FITC)-tagged molecules was monitored in the capillary bed. The data were analyzed using a one-dimensional model to obtain only the diffusion coefficients for various test molecules.

Rutili *et al.* (1982) have estimated the permeability surface area products for total plasma proteins in dog-paw lymph. They have reported that at low-lymph-flow states convection provides for 70% of the protein transport and diffusion only 30%. At high lymph flows, protein transport was reported to be predominantly convective.

Nugent and Jain (1984) have measured concentration-time profiles of fluorescein isothiocyanate (FITC)-conjugated bovine serum albumin and a graded series of FITC-dextrans within the erythrocyte-free plasma layer in individual vessels and at various positions within the

interstitial tissue space of mature granulation tissue grown in a rabbit ear chamber. Also in this study, the interstitial transport data were analyzed using a one-dimensional diffusion model.

Gerlowski and Jain (1986) have measured microvascular permeability in normal and neoplastic tissues. Interstitial diffusion coefficients and microvascular permeability coefficients in their study were determined by fitting a one-dimensional permeability-diffusion model to the extravasation data. The values of the effective permeability, which included both convective and diffusive terms were calculated by assuming that 1% of the transcapillary exchange was due to diffusion.

Ley and Arfors (1986), using a digital image analysis of fluorescein angiograms developed by Åslund *et al.* (1979), have determined the overall permeability parameters for sodium fluorescein and FITC-Dx 3 using a one-dimensional mathematical model of microvascular blood-tissue transport in the hamster cheek pouch, in which only diffusion was accounted for.

Baxter *et al.* (1987) have developed a one-dimensional mathematical model which relates the number of leaky sites in postcapillary venules to the extravasation of macromolecules in terms of an effective microvascular permeability, and an effective interstitial diffusion coefficient. Their one-dimensional model contained only one diffusion term.

Bekker *et al.* (1989) have determined the effective microvascular permeability coefficients for a graded series of FITC-Dxs using intravital fluorescent microscopy in a one-dimensional, two-compartment diffusion model.

The studies cited above are based on a similar principle: the

image brightness is sampled and quantified at each pixel location and related to the fluorochrome concentration. The experimentally determined concentration profiles are then compared to the theoretically predicted concentration distributions, and the transport parameters are estimated by comparing the two curves and minimizing the error. The concentration as a function of time is used as an independent variable in the computation and optimization of the parameters.

In spite of the significant number of experimental studies appeared in the recent literature, any improvement in the understanding of this phenomenon can only be achieved if an improved comprehensive model which accounts for both molecular diffusion effects and convective transport effects to explain macromolecular transfer across microvascular wall and into the interstitial space is developed. The availability of such a model would enable investigators to interpret their experimental data on the basis of one of the two mechanisms or on a combination of both.

CHAPTER 3

MODELING OF MACROMOLECULAR TRANSPORT

3.1. Model Development

The present model was developed assuming that the macromolecule transport occurs in a thin tissue region (such as the cheek pouch of a hamster) confined between two extended planes, and crossed by microvessels running parallel to the planes containing the tissue region. The region of interest for the analysis is that at and near a single capillary, which is assumed to be a straight cylinder surrounded by a wall of thickness δ. The transport process from one single capillary was modeled neglecting the interference from the other capillaries in the tissue from which extravasation may also be occurring at the same time. This implies that the time interval during which the process can be adequately described by the model must be much smaller than the ratio of the average transport velocity to the average distance between two neighboring capillaries, i.e., that the transport process must be slow with respect to the distance to be traveled by the molecules during the time period in which the process is observed. The validity of this assumption has been experimentally validated by Bekker *et al.* (1989), who were able to observe extravasation from a single postcapillary venule and quantify the transport rate for a rather extensive period of time (up to 35 minutes).

In our model we also assumed that the diameter of the microvessel was large enough, if compared to the thickness of the tissue in which

it is imbedded, so that the macromolecule transport in the direction perpendicular to the planes bounding the tissue could be neglected. This assumption has already been extensively used in the past. For example, Wiederhielm (1966) and Wiederhielm *et al.* (1973) have given considerable attention to the effect of cylindrical geometry on the pattern of movement of materials from capillaries into the surrounding tissue matrix, whereas Fox and Wayland (1979) have carried out a model simulation for diffusion from a cylindrical source (20 μm diameter) into a surrounding semi-infinite 40 μm tissue slab using a two-dimensional tissue preparations. This simulation has shown that since the concentration gradients perpendicular to the tissue plane rapidly die out (because of the no-flux constraints above and below this plane) the total integrated concentration resulting from photometric measurement is essentially equivalent to that arising from a planar source. Therefore, a one-dimensional model appears to provide good approximation to transport in interstitial space of this geometry.

From a mathematical point of view the region considered in our model consists of the space confined between two parallel semi-infinite planes, as shown in Figure 3.1. This space is further subdivided into two regions. The first one, extending in the z-direction between $-\delta$ (the side of the microvascular wall next to the plasma) and 0 (the side of the wall next to the interstitial space), represents the microvascular wall. The second semi-infinite region, extending from 0 to infinity in the z-direction, represents the tissue or interstitial space.

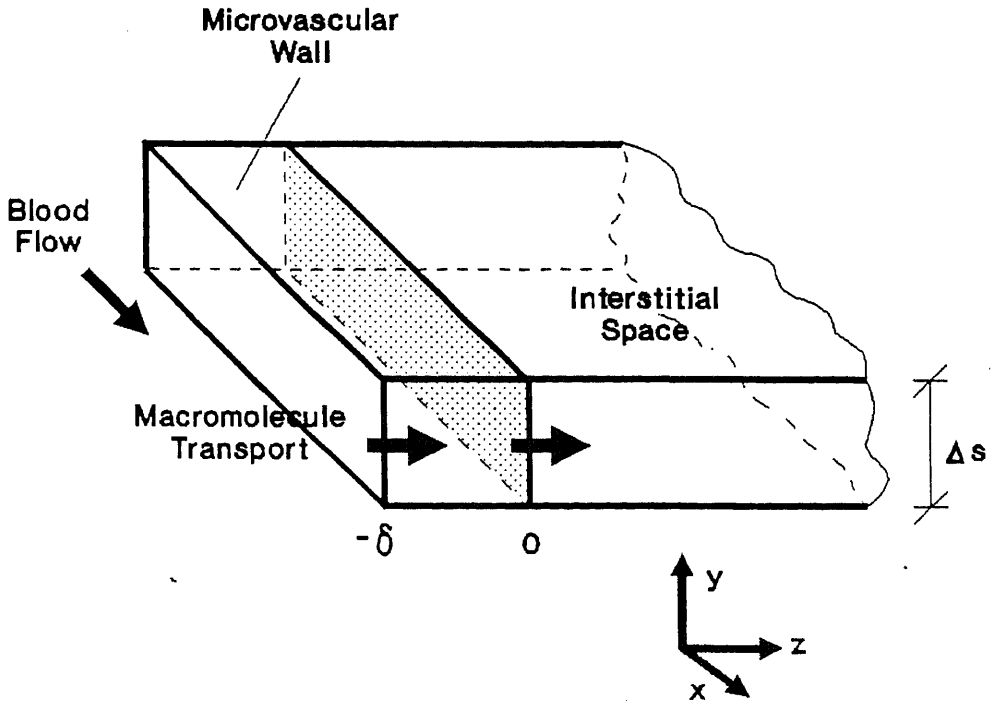

Fig 3.1 Schematic diagram of the system

In addition, the following simplifying assumptions were also made:

(1) the macromolecule concentration in the plasma is maintained at a constant level. Since the blood-side mass transfer resistance between the bulk of the blood and the wall is assumed to be small in comparison to the other resistances in series, this concentration, multiplied by an appropriate partition (or equilibrium) constant, is equal to Co, i.e., the macromolecule concentration in the wall region at the plasma-wall interface. This concentration is assumed to be a constant;

(2) in both regions the macromolecule concentration gradients in the x- and y-directions are always zero. This implies that the end effects are neglected.

Because of these assumptions, the transport equations in the two regions can be written in terms of rectangular rather than cylindrical coordinates in which both molecular diffusion and convective transport are considered. These equations are (Bird *et al.*, 1960):

$$\frac{\partial C_1}{\partial t} = D_1 \frac{\partial^2 C_1}{\partial z^2} - \chi_1 V_1 \frac{\partial C_1}{\partial z} \qquad \text{for} \quad -\delta \le z < 0 \qquad (3.1)$$

$$\frac{\partial C_2}{\partial t} = D_2 \frac{\partial^2 C_2}{\partial z^2} - \chi_2 V_2 \frac{\partial C_2}{\partial z} \qquad \text{for} \quad 0 \le z < +\infty \qquad (3.2)$$

where D_1 and D_2 are the diffusivity coefficients in the microvascular wall and interstitial space, respectively (D_1 being the effective diffusivity in the porous region of the microvascular wall), V_1 and V_2 are the average fluid velocity terms in the z-direction for the

same regions, and χ_1 and χ_2 are the sieving coefficients accounting for the interaction between solute molecule and pore in the microvascular wall region (χ_1), and in the interstitial space (χ_2) (Anderson and Quinn, 1974).

The corresponding initial and boundary conditions are:

$$C_1(t=0,z) = 0 \qquad \text{for } -\delta \le z < 0 \qquad (3.3)$$

$$C_1(t,z=-\delta) = C_o \qquad \text{for } t>0 \qquad (3.4)$$

$$C_1(t,z=0) = a\, C_2(t,z=0) \qquad \text{for } t>0 \qquad (3.5)$$

$$C_2(t=0,z) = 0 \qquad \text{for } 0 \le z < +\infty \qquad (3.6)$$

$$C_2 \to 0, \quad \text{as} \quad z \to \infty \qquad (3.7)$$

$$D_1 \frac{\partial C_1}{\partial z} - \chi_1 V_1 C_1 = b \left(D_2 \frac{\partial C_2}{\partial z} - \chi_2 V_2 C_2 \right) \quad \text{at} \quad z=0 \qquad (3.8)$$

where, a: wall-interstitial space equilibrium constant;

b: ratio of the cross-sectional area of the two regions.

Equation (3.4) expresses the condition that the concentration in the wall at the plasma-wall interface is constant and equal to Co. Equation (3.5) expresses a linear equilibrium condition at the wall-interstitial space interface, where "a" represents the wall-interstitial space equilibrium constant.

If only short-term data are used, we can neglect the effect of nearby vessels and seek a solution applicable to small penetration distances, as discussed above. Equation (3.7) expresses this condition. Equation (3.8), expressing the continuity of mass flux at the interface between the two regions, was obtained using the equation for the mass flux in a pore obtained by Anderson and Quinn (1974),

i.e.

$$\bar{N} = - D \frac{dC}{dz} + \chi CV \qquad (3.9)$$

with

$$\chi = \int_0^{1-\gamma} \{4\beta\ (1-\beta^2)\ G\}\ d\beta \qquad (3.10)$$

where, χ: sieving coefficient

γ: radius of solute molecule/pore radius

β: radial position in the pore/pore radius

G: lag coefficient accounting for the retarding effect of the pore wall on the solute velocity

The upper limit of integration in equation (3.10) is equal to $(1-\gamma)$ and not to 1 because the center of the spherical molecule can not approach the pore wall any closer than the molecule radius. Hence the real transport area for the molecule is smaller than the pore area.

An integral expression for the equilibrium constant "a" for a rigid particle (or molecule) characterized by a non-dimensional length γ (defined as the ratio of the radius of solute molecule to the pore radius) and a shape factor ε (equal to the ratio of the longest to the shortest dimension of the solute molecule) was derived by Giddings *et al.* (1968) as

$$a = \int_{all\ \Psi} \int_0^1 2\beta P_s\ (\gamma, \varepsilon; \beta, \Psi)\ d\beta\ d\Psi \qquad (3.11)$$

where Ψ represents the Eulerian angular orientation of the particle with respect to the pore axis, and P_s is a discrete probability function which equals 1 if the particle can be situated with the pore (without penetrating the pore wall), and zero otherwise.

In addition, from a mass balance for the water across the microvascular wall-interstitial space interface one can write

$$V_1 = b\ V_2 \tag{3.12}$$

which implies that the total number of independent parameters in equations (3.1) to (3.8) is reduced by one. In particular, if b = 1, then the velocities in both regions are equal.

3.2. Analytical Solution for the Model

First, a substitution can be made to eliminate the convective terms from equations (3.1) and (3.2) using the transformation

$$C_i(t,z) = e^{\chi_i V_i (z - \frac{\chi_i V_i}{2})/2D_i}\ W_i(t,z) \tag{3.13}$$

where i = 1,2 and W_i is an auxiliary variable.

Equations (3.1) and (3.2) may be rewritten as

$$\frac{\partial W_1}{\partial t} = D_1 \frac{\partial^2 W_1}{\partial z^2} \qquad \text{for } -\delta \le z < 0 \tag{3.14}$$

$$\frac{\partial W_2}{\partial t} = D_2 \frac{\partial^2 W_2}{\partial z^2} \qquad \text{for} \quad 0 \le z < +\infty \qquad (3.15)$$

Applying the Laplace transform to equations (3.14) and (3.15), we obtain

$$\frac{d^2\overline{W_1}}{dz^2} - q_1^2\,\overline{W_1} = 0 \qquad \text{where,} \quad q_1^2 = \frac{s}{D_1} \qquad (3.16)$$

using the initial condition (3.3), and

$$\frac{d^2\overline{W_2}}{dz^2} - q_2^2\,\overline{W_2} = 0 \qquad \text{where,} \quad q_2^2 = \frac{s}{D_2} \qquad (3.17)$$

using the initial condition (3.6).

In order to apply the boundary conditions to equations (3.16) and (3.17) it is necessary to convert $\overline{W_1}$ and $\overline{W_2}$ to $\overline{C_1}$ and $\overline{C_2}$, respectively.

By applying the Laplace transform to equation (3.13) we obtain

$$\overline{C_i}\,(s,z) = e^{\frac{\chi_i V_i}{2D_i} z}\ \overline{W_i}\{z,\ s+\frac{(\chi_i V_i)^2}{4D_i}\} \qquad \text{where, } i=1,2 \qquad (3.18)$$

Equation (3.18) can be used to obtain the solution to equation (3.16):

$$\overline{C_1}\,(s,z) = e^{\frac{\chi_1 V_1}{2D_1} z}\,(B_1 \cosh q_1^* z + B_2 \sinh q_1^* z) \qquad (3.19)$$

where, $(q_1^*)^2 = \frac{s}{D_1} + (\frac{\chi_1 V_1}{2D_1})^2$, and B_1 and B_2 are constants.

Equation (3.18) can be used again to obtain a solution to equation (3.17) with boundary condition (3.7):

$$\overline{C_2}\,(s,z) = B_3\, e^{\left(\frac{\chi_2 V_2}{2D_2} - q_2^*\right) z} \qquad (3.20)$$

where, $(q_2^*)^2 = \frac{s}{D_2} + \left(\frac{\chi_2 V_2}{2D_2}\right)^2$, and B_3 is a constant.

In order to calculate B_1, B_2, and B_3 the boundary conditions (3.4), (3.5), and (3.8), appropriately expressed in terms of $\overline{C_1}$ and $\overline{C_2}$, are applied to equations (3.19) and (3.20), yielding the following

$$\frac{\overline{C_1}(s,z)}{C_0} = e^{\frac{\chi_1 V_1}{2D_1}(z+\delta)}\left[\frac{1}{s}\,\frac{2D_1 q_1^* \cosh q_1^* z - \left\{\frac{b}{a}\left(\chi_2 V_2 + 2q_2^* D_2\right) - \chi_1 V_1\right\}\sinh q_1^* z}{2D_1 q_1^* \cosh q_1^* \delta + \left\{\frac{b}{a}\left(\chi_2 V_2 + 2q_2^* D_2\right) - \chi_1 V_1\right\}\sinh q_1^* \delta}\right] \qquad (3.21)$$

and

$$\frac{\overline{C_2}(s,z)}{C_0} = \frac{e}{a}^{\frac{\chi_1 V_1 \delta}{2D_1}}\left[\frac{1}{s}\,\frac{2D_1 q_1^*\, e^{\left(\frac{\chi_2 V_2}{2D_2} - q_2^*\right) z}}{2D_1 q_1^* \cosh q_1^* \delta + \left\{\frac{b}{a}\left(\chi_2 V_2 + 2q_2^* D_2\right) - \chi_1 V_1\right\}\sinh q_1^* \delta}\right] \qquad (3.22)$$

The inverse Laplace transform of equations (3.21) and (3.22) then gives the desired solution. We used contour integration in the complex region to perform such inversion (Carslaw and Jaeger, 1959). Prior to this step we found more convenient to express these equations using the following substitution

$$\lambda = s + \frac{(\chi_2 V_2)^2}{4D_2} \tag{3.23}$$

in order to move the origin in correspondence of the branch point $s = -\frac{(\chi_2 V_2)^2}{4D_2}$, which is one of the roots of the denominators in equations (3.21) and (3.22).

The inverse Laplace transform of equation (3.21) could then be expressed as

$$\frac{C_1(t,z)}{C_o} = \frac{1}{2\pi\iota} e^{\frac{V_1\chi_1}{2D_1}(z+\delta)} \int_{r-\iota\infty}^{r+\iota\infty} \frac{1}{\lambda - \frac{(\chi_2 V_2)^2}{4D_2}} \cdot$$

$$\frac{2D_1 q_1^\circ \cosh q_1^\circ z - \{\frac{b}{a}(\chi_2 V_2 + 2q_2^\circ D_2) - \chi_1 V_1\} \sinh q_1^\circ z}{2D_1 q_1^\circ \cosh q_1^\circ \delta + \{\frac{b}{a}(\chi_2 V_2 + 2q_2^\circ D_2) - \chi_1 V_1\} \sinh q_1^\circ \delta} e^{\{\lambda - \frac{(\chi_2 V_2)^2}{4D_2}\}t} d\lambda \tag{3.24}$$

where, $(q_1^\circ)^2 = \frac{\lambda}{D_1} + \frac{(\chi_1 V_1)^2}{4D_1^2} - \frac{(\chi_2 V_2)^2}{4D_1 D_2}$, and $(q_2^\circ)^2 = \frac{\lambda}{D_2}$

and where r is a constant to be so large that all the singularities of equation (3.24) lie to the left of the line $(r-\iota\infty, r+\iota\infty)$.

The integral in this equation can be calculated by analyzing the singularities of the integrand. These singularities can be found by determining the roots of the denominator in equation (3.24). By imposing that $q_2^\circ = 0$ one can find that a branch point exists in correspondence of $\lambda = 0$ (one can also prove that the branch point which would produce from $q_1^\circ = 0$ can be removed if the hyperbolic sine

and cosine terms in equations (3.21) and (3.22) are expanded in Taylor series). In addition, from equation (3.24) one can also find that a single pole exist in correspondence of $\lambda = \frac{(\chi_2 V_2)^2}{4D_2}$, and for all the values of λ for which

$$2D_1 q_1^\circ \cosh q_1^\circ \delta + \{\frac{b}{a}(\chi_2 V_2 + 2q_2^\circ D_2) - \chi_1 V_1\} \sinh q_1^\circ \delta = 0 \qquad (3.25)$$

The roots of equation (3.25) are all real and simple, as proven in the Appendix A. In addition, one can prove that equation (3.25) can only have a *finite* number of roots (if any) associated with residues different from zero, as explained below in greater detail.

The integral in equation (3.24) was calculated to be equal to the sum of the contour integral along the line EHJKL outlined in Figure 3.2 (i.e., over the small circle about the origin, plus the integrals over the lines EH and KL), the residue at $\lambda = \frac{(\chi_2 V_2)^2}{4D_2}$, and the residues at all the roots of equation (3.25) (Carslaw and Jaeger, 1959).

The residue at $\lambda = \frac{(\chi_2 V_2)^2}{4D_2}$ is equal to

$$e^{k_1(z^*+1)} \cdot \frac{\cosh(k_1 z^*) - (2k_2 - 1)\sinh(k_1 z^*)}{\cosh k_1 + (2k_2 - 1)\sinh k_1} \qquad (3.26)$$

where, $k_1 = \frac{\chi_1 V_1 \delta}{2D_1}$, $k_2 = \frac{b}{a}\frac{\chi_2 V_2}{\chi_1 V_1}$, and $z^* = \frac{z}{\delta}$

The contour integral along the small circle HJK can be calculated to be equal to zero. By putting $\lambda = (D_1/\delta^2)\, u'^2\, e^{i\pi}$ along EH and $\lambda =$

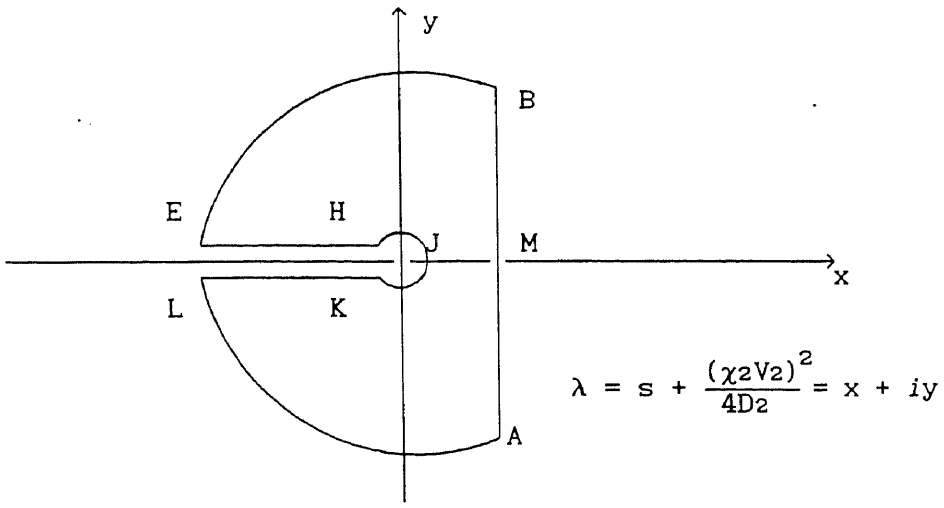

FIGURE 3.2 BROMWICH PATH FOR CONTOUR INTEGRATION

$(D_1/\delta^2)\ u'^2\ e^{-i\pi}$ along KL the contribution of the contour integral along these two paths becomes

$$-\frac{8}{\pi} e^{k_1(z^*+1)} \int_0^{\infty} e^{-k_4\tau} \frac{(u^2/k_4)\ k_5\ k_3 \sin\{k_3(z^*+1)\}}{\{\frac{k_3}{k_1}\cos k_3 - (1-k_2)\sin k_3\}^2 + (k_6 \sin k_3)^2}\, du \qquad (3.27)$$

where, $k_3 = \sqrt{(\frac{u}{\delta})^2 + \frac{(\chi_2 V_2)^2}{4D_1D_2} - (\frac{\chi_1 V_1}{2D_1})^2} \cdot \delta$, $k_4 = u^2 + \frac{(\chi_2 V_2 \delta)^2}{4D_1D_2}$,

$k_5 = \frac{b}{a} \frac{D_1\ D_2}{(\chi_1 V_1)^2} \frac{1}{\delta^2} \sqrt{\frac{D_1}{D_2}}$, $k_6 = 2\frac{b}{a}\frac{D_2}{\chi_1 V_1}\frac{u}{\delta}\sqrt{\frac{D_1}{D_2}}$, and $\tau = t\frac{D_1}{\delta^2}$

In order to avoid a negative value under the square root sign in the expression for k_3 during the calculation of equation (3.27), k_3 may be separated into two parts using the following substitution

$$\text{for } u < \delta\sqrt{(\frac{\chi_1 V_1}{2D_1})^2 - \frac{(\chi_2 V_2)^2}{4D_1D_2}}, \longrightarrow k_3 = \iota\, k_9 \qquad (3.28)$$

$$\text{for } u \geq \delta\sqrt{(\frac{\chi_1 V_1}{2D_1})^2 - \frac{(\chi_2 V_2)^2}{4D_1D_2}}, \longrightarrow k_3 = k_3 \qquad (3.29)$$

where, $k_7 = \frac{\chi_2 V_2 \delta}{2\ D_2}$ $k_8 = \frac{D_1}{\chi_1 V_1}\frac{1}{\delta\ u}$, and $k_9 = \delta\sqrt{(\frac{\chi_1 V_1}{2D_1})^2 - \frac{(\chi_2 V_2)^2}{4D_1D_2} - (\frac{u}{\delta})^2}$

The residues at all the poles which lie within the area delimited by the closed curve BEHJKLAB can be obtain using the theory of residues (once the poles have been identified) as more clearly explained below.

Finally, by summing together all these contribution from the contour integral and the residues, the macromolecule concentration in the microvascular wall region, $C_1(\tau, z^*)$, was found to be

$$\frac{C_1(\tau,z^*)}{C_0} = e^{k_1(z^*+1)} \left[\frac{\cosh(k_1 z^*) - (2k_2 - 1)\sinh(k_1 z^*)}{\cosh k_1 + (2k_2 - 1)\sinh k_1} \right.$$

$$- \frac{8}{\pi} \left\{ \int_0^{k_{10}} e^{-k_4 \tau} \frac{(u^2/k_4)\, k_5\, k_9 \sinh\{k_9(z^*+1)\}}{\{\frac{k_9}{k_1}\cosh k_9 - (1-k_2)\sinh k_9\}^2 + (k_6 \sinh k_9)^2}\, du \right.$$

$$\left. + \int_{k_{10}}^{\infty} e^{-k_4 \tau} \frac{(u^2/k_4)\, k_5\, k_3 \sin\{k_3(z^*+1)\}}{\{\frac{k_3}{k_1}\cos k_3 - (1-k_2)\sin k_3\}^2 + (k_6 \sin k_3)^2}\, du \right\}$$

$$+ \sum_{n=1}^{m} \frac{2k_{12}\sin\{(z^*+1)k_{12}\}\; e^{-(k_{12}^2+k_{13}^2)\tau}}{(k_{12}^2 + k_1^2)\,(\frac{1}{k_{12}}\cos k_{12}\sin k_{12} - 1 - \frac{k_{17}}{k_{19}}\sin^2 k_{12})}$$

$$\left. + \frac{2k_{15}\sinh\{k_{15}(z^*+1)\}\; e^{-(k_{14}-k_{16})\tau}}{(k_{16} - k_{14})\,(\frac{1}{k_{15}}\cosh k_{15}\sinh k_{15} - 1 + \frac{k_{17}}{k_{18}}\sinh^2 k_{15})} \right] \tag{3.30}$$

where, $k_{10} = \delta \sqrt{(\frac{\chi_1 V_1}{2D_1})^2 - \frac{(\chi_2 V_2)^2}{4D_1 D_2}}$, $k_{11} = \sqrt{\frac{D_1}{D_2}}$, $k_{12} = X_n \delta$,

$$k_{13} = \frac{\chi_1 V_1 \delta}{2D_1}, \qquad k_{14} = \frac{(\chi_2 V_2 \delta)^2}{4D_1 D_2}, \qquad k_{15} = q^{\circ}_{1o}\,\delta, \qquad k_{16} = \frac{\lambda_o \delta^2}{D_1},$$

$$k_{17} = \frac{b}{a}, \quad k_{18} = q^{\circ}_{2o}\,\delta, \quad \text{and} \quad k_{19} = \delta \sqrt{-\frac{D_1}{D_2} X_n^2 - \frac{(\chi_1 V_1)^2}{4D_1 D_2} + \left(\frac{\chi_2 V_2}{2D_2}\right)^2}$$

and where q°_{1o} and q°_{2o} are given below.

We will now examine the origin of each term in equation (3.30). In equation (3.30) the first term in brackets corresponds to the residue at $\lambda = \frac{(\chi_2 V_2)^2}{4D_2}$. The two integral terms are obtained as the sum of the contributions of the integrals along the lines EH and KL in Figure 3.2 (these two terms were found by combining together equations (3.27), (3.28), and (3.29)). The summation term and the last term in equation (3.30) are equal to residues in correspondence of the roots (if any) of equation (3.25). More specifically, we were able to prove in Appendix B that the fourth term (containing the summation) in equation (3.30) will be different from zero only if the equation

$$\tan(X_n \delta) = \frac{2 D_1 X_n}{\chi_1 V_1 - \frac{b}{a}(\chi_2 V_2 + 2D_2 \Phi)} \tag{3.31}$$

with $n = 1, 2, 3, \ldots\ldots, m$ and $\Phi = \sqrt{-\frac{D_1}{D_2} X_n^2 - \frac{(\chi_1 V_1)^2}{4D_1 D_2} + \left(\frac{\chi_2 V_2}{2D_2}\right)^2}$

is satisfied for values of X_n in the range

$$0 < X_n^2 < \frac{(\chi_2 V_2)^2}{4D_1 D_2} - \left(\frac{\chi_1 V_1}{2D_1}\right)^2$$

It is obvious that equation (3.31) can be only have a finite number of roots (if any) in this range.

Similarly, the fifth term in equation (3.30) will be different from zero only if the equation

$$\tanh\left(q_{1o}^{\circ}\,\delta\right) = \frac{2D_1\, q_{1o}^{\circ}}{\chi_1 V_1 - \frac{b}{a}\left(\chi_2 V_2 + 2q_{2o}^{\circ} D_2\right)} \qquad (3.32)$$

with $q_{1o}^{\circ} = q_1^{\circ}\Big|_{\lambda=\lambda_o}$ and $q_{2o}^{\circ} = q_2^{\circ}\Big|_{\lambda=\lambda_o}$

is satisfied for values of λ_o which simultaneously satisfy the two conditions

$$\lambda_o > \frac{(\chi_2 V_2)^2}{4D_2} - \frac{(\chi_1 V_1)^2}{4D_1} \quad \text{and} \quad \lambda_o > 0$$

The proof is also reported in Appendix B.

Using a similar approach, the macromolecule concentration in the interstitial space, $C_2(\tau, z^*)$, can be calculated to be given by

$$\frac{C_2(\tau, z^*)}{C_o} = \frac{1}{a}\, e^{(k_1 + z^* k_7)} \left[\frac{e^{-z^* k_7}}{\cosh k_1 + (2k_2 - 1)\sinh k_1} - \right.$$

$$\frac{4}{\pi}\left\{\int_0^{k_{10}} e^{-k_4\tau}\,\frac{u^2}{k_4}\cdot \frac{2k_5k_9\sinh k_9\cos(z^*uk_{11})+k_8k_9\{\frac{k_9}{k_1}\cosh k_9-(1-k_2)\sinh k_9\}\sin(z^*uk_{11})}{\{\frac{k_9}{k_1}\cosh k_9-(1-k_2)\sinh k_9\}^2+(k_6\sinh k_9)^2}\,du\right.$$

$$+\int_{k_{10}}^{\infty} e^{-k_4\tau}\,\frac{u^2}{k_4}\cdot \left.\frac{2k_5k_3\sin k_3\cos(z^*uk_{11})+k_8k_3\{\frac{k_3}{k_1}\cos k_3-(1-k_2)\sin k_3\}\sin(z^*uk_{11})}{\{\frac{k_3}{k_1}\cos k_3-(1-k_2)\sin k_3\}^2+(k_6\sin k_3)^2}\,du\right\}$$

$$+\sum_{n=1}^{m}\left[\frac{2k_{12}(\sin k_{12})\,e^{-z^*k_{19}-(k_{12}^2+k_{13}^2)\tau}}{(k_{12}^2+k_1^2)(\frac{1}{k_{12}}\cos k_{12}\sin k_{12}-1-\frac{k_{17}}{k_{19}}\sin^2 k_{12})}\right.$$

$$\left.+\frac{2k_{15}(\sinh k_{15})\,e^{-z^*k_{18}-(k_{14}-k_{16})\tau}}{(k_{16}-k_{14})(\frac{1}{k_{15}}\cosh k_{15}\sinh k_{15}-1+\frac{k_{17}}{k_{18}}\sinh^2 k_{15})}\right] \tag{3.33}$$

Also in this case, the last two terms in equation (3.33) are different from zero only if equations (3.31) and (3.33) have any real roots.

If $V_1=V_2=0$, equations (3.30) and (3.33) produce a simpler solution which is identical to that obtained by Carslaw and Jaeger (1959).

3.3. Numerical Solution for the Model

The model represented by equations (3.1) through (3.8) was also

solved numerically using a subroutine program called MOLCH (IMSL, 1986). This subroutine is based on the method of lines with cubic Hermite polynomials. The computer program is listed in Appendix C.

Let m=number of differential equations and n=number of mesh points in the program. MOLCH solves the partial differential equation system

$$\frac{\partial u^k}{\partial t} = f^k \left(x, t, u^1, \ldots . u^m, \frac{\partial u^m}{\partial x}, \frac{\partial u^m}{\partial x}, \frac{\partial^2 u^1}{\partial x^2}, \ldots . \frac{\partial^2 u^m}{\partial x^2}\right)$$

with the initial conditions

$$u^k = u_o^k(x) \qquad \text{at} \quad t = t_o$$

and the boundary conditions

$$\alpha_1^k u^k + \beta_1^k \frac{\partial u^k}{\partial x} = \gamma_1^k \qquad \text{at} \quad x = x_1$$

$$\alpha_m^k u^k + \beta_m^k \frac{\partial u^k}{\partial x} = \gamma_m^k \qquad \text{at} \quad x = x_m,$$

for k=1,....., m. Cubic Hermite polynomials are used in the spatial approximation so that the trial solution is expanded in the series

$$\hat{u}^k(x,t) = \sum_{i=1}^{m} \{a_i^k(t)\phi_i(x) + b_i^k(t)\psi_i(x)\},$$

where $\phi_i(x)$ and $\psi_i(x)$ are the standard basis functions for the cubic Hermite polynomials with the knots $x_1<x_2< \cdots\cdots <x_n$. These are piecewise cubic polynomials with continuous first derivatives. At the breakpoints they satisfy the following conditions

$$\phi_1(x_1) = \delta_{11} \qquad \psi_1(x_1) = 0$$

$$\frac{d\phi_1}{dx}(x_1) = 0 \qquad \frac{d\psi_1}{dx}(x_1) = \delta_{11}$$

According to the collocation method, the coefficients of the approximation are obtained so that the approximation satisfies the differential equation at the two Gaussian points in each subinterval,

$$p_{2j-1} = x_j + \frac{3 - \sqrt{3}}{6}(x_{j+1} - x_j)$$

$$p_{2j} = x_j + \frac{3 - \sqrt{3}}{6}(x_{j+1} + x_j)$$

for $j = 1, \cdots\cdots\cdots, n$.

The collocation approximation to the differential equation is

$$\frac{da_i^k}{dt}\phi_i(p_j) + \frac{db_i^k}{dt}\psi_i(p_j) =$$

$$f^k(p_j, t, \hat{u}^1(p_j), \cdots, \hat{u}^M(p_j), \hat{u}_x^1(p_j), \cdots, \hat{u}_x^M(p_j), \hat{u}_{xx}^1(p_j), \cdots, \hat{u}_{xx}^M(p_j))$$

for $k = 1, \cdots, m$ and $j = 1, \cdots, 2(n-1)$. This is a system of $2m(n-1)$ ordinary differential equations in $2mn$ unknown coefficient functions, a_i^k and b_i^k. The last $2m$ equations are obtained by differentiating the boundary conditions

$$\alpha_i^k \frac{da_i^k}{dt} + \beta_i^k \frac{db_i^k}{dt} = \frac{d\gamma_i^k}{dt}$$

$$\alpha_m^k \frac{da_m^k}{dt} + \beta_m^k \frac{db_m^k}{dt} = \frac{d\gamma_m^k}{dt}$$

for $k = 1, \cdots, m$.

The initial conditions $u_o^k(x)$ must satisfy the boundary conditions, also $\gamma_1^n(t)$ must be continuous or the boundary conditions will not be properly imposed for $t>t_o$.

3.4. Application of the Model to Microvascular Transport

Equations (3.30) and (3.33) can be used to determine the non-dimensional concentration profiles in the microvascular wall ($C_1(\tau,z^*)/C_o$) and in the interstitial space ($C_2(\tau,z^*)/C_o$) for any given set of the parameters required in the equations, i.e., for any eight out of the following nine parameters (since equation (3.12) must be satisfied): D_1, D_2, V_1, V_2, a, b, δ, χ_1, and χ_2. Examples of such profiles for selected values of the parameters are given in Figures 3.3, 3.4, 3.5, and 3.6. Figure 3.3 shows the concentration profile for the case in which the diffusion coefficient in the interstitial space is much larger than that in the microvascular wall region. The reverse is true for the case in which the diffusivity coefficient ratio is inverted, as shown in Figure 3.4, for which case the wall region becomes a well mixed region. In both these examples the convective transport contributions were arbitrarily set at very low values in comparison to the diffusivity contributions. Intermediate profiles can be obtained for other combinations of parameters in which the convective contribution is more significant, as shown in Figures

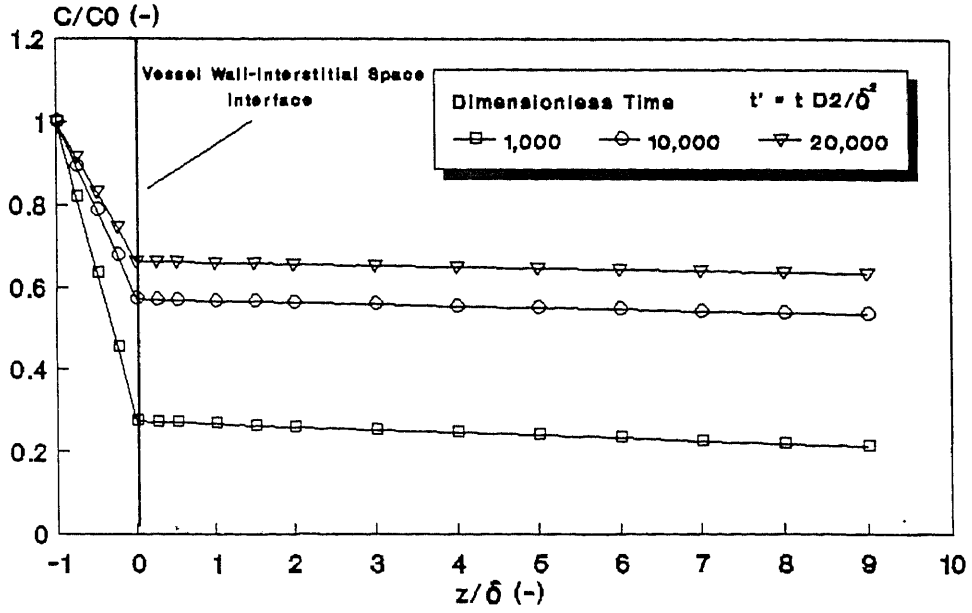

Figure 3.3 Concentration Profiles

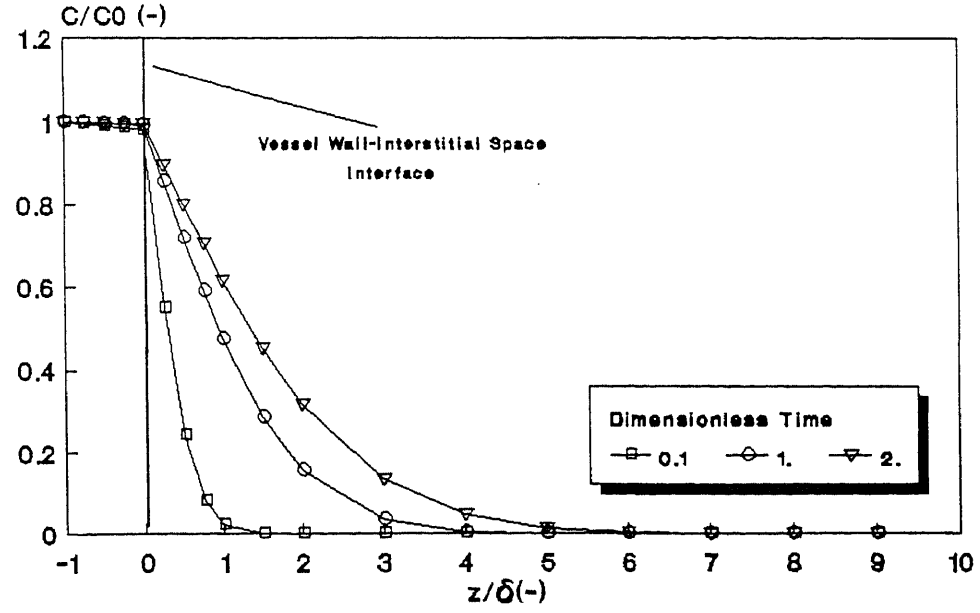

Figure 3.4 Concentration Profiles

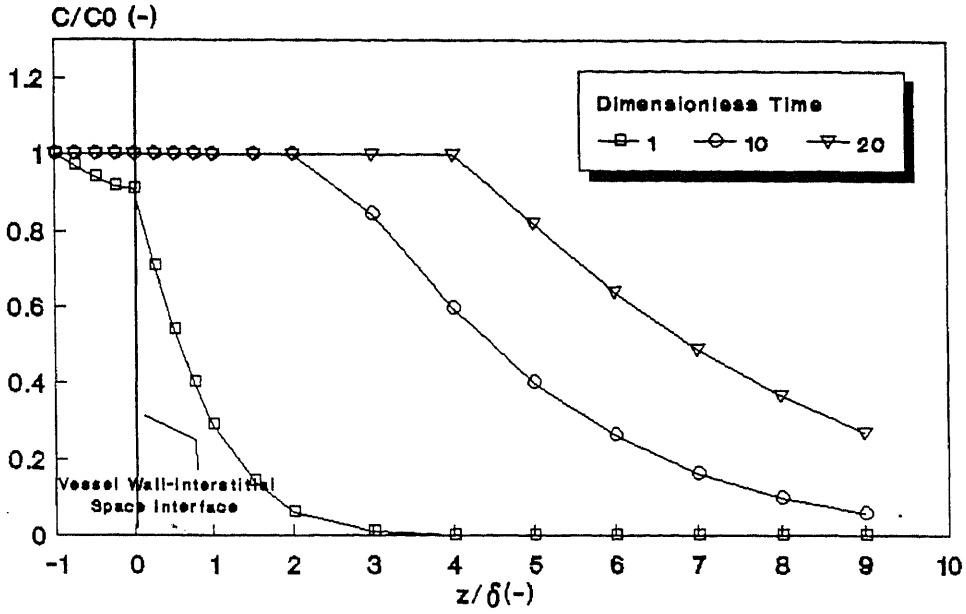

D2/D1=1; a=b=1
D1/(V1χ1δ)=1; D2/(V2χ2δ)=100
χ2/χ1=0.01

Figure 3.5 Concentration Profiles

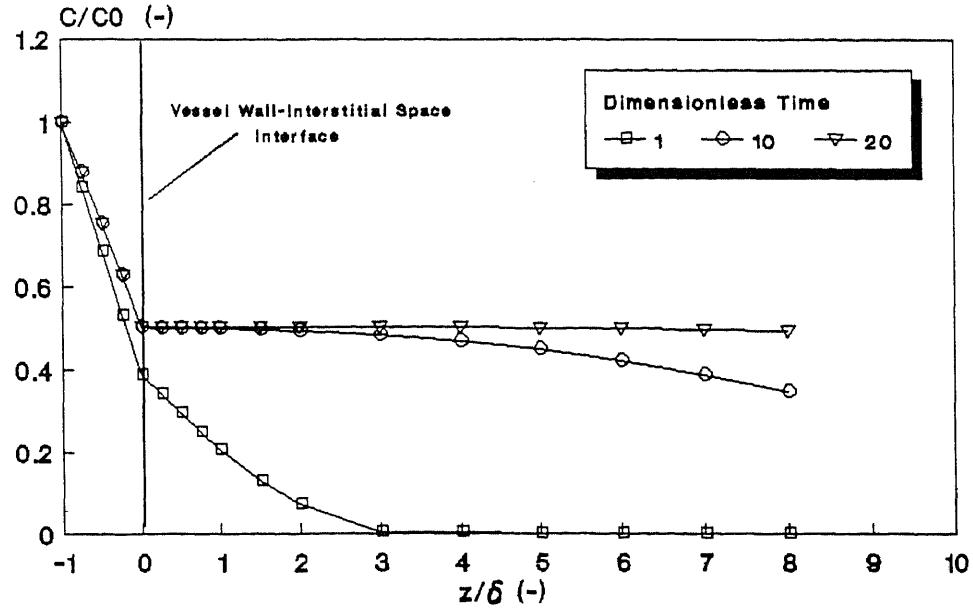

D2/D1=1; a=b=1
D1/(V1χ1δ)=100; D2/(V2χ2δ)=1
χ2/χ1=100

Figure 3.6 Concentration Profiles

3.5 and 3.6.

The comparisons between analytical and numerical solutions for each of the cases considered above are presented in Figures 3.7, 3.8, 3.9, and 3.10. The results are nearly identical at each case.

In this study, equations (3.30) and (3.33) were used to determiene the values of D_1, D_2, V_1 and V_2 from experimental data. These equations can also be used to determine the profiles of other variables which are functions of the concentrations. In particular the concentration equations can be used to obtain an expression for M(t), the cumulative amount of macromolecule which has extravasated into the interstitial space in a given period of time t. This can be expressed mathematically as

$$M(t) = S \int_0^t \left(- D_2 \frac{dC_2}{dz}\bigg|_{z=0} + \chi_2 V_2 C_2 \bigg|_{z=0}\right) dt \qquad (3.34)$$

where S is the surface area of the leaking capillary vessel. Substituting equation (3.33) into equation (3.34) and performing the necessary differentiation yields:

$$M(t) = S \left[\frac{1}{a} C_0 e^{k_1} \int_0^t \left[\frac{\chi_2 V_2}{\cosh k_1 + (2k_2 - 1)\sinh k_1} - \frac{4}{\pi}\left\{\int_0^{k_{10}} e^{-k_4\tau} \frac{u^2}{k_4} \cdot \frac{\chi_2 V_2 k_5 k_9 \sinh k_9 - D_2 k_8 k_9 \{\frac{k_9}{k_1}\cosh k_9 - (1-k_2)\sinh k_9\} \frac{u}{\delta} k_{11}}{\{\frac{k_9}{k_1}\cosh k_9 - (1-k_2)\sinh k_9\}^2 + (k_6 \sinh k_9)^2} du +\right.\right.\right.$$

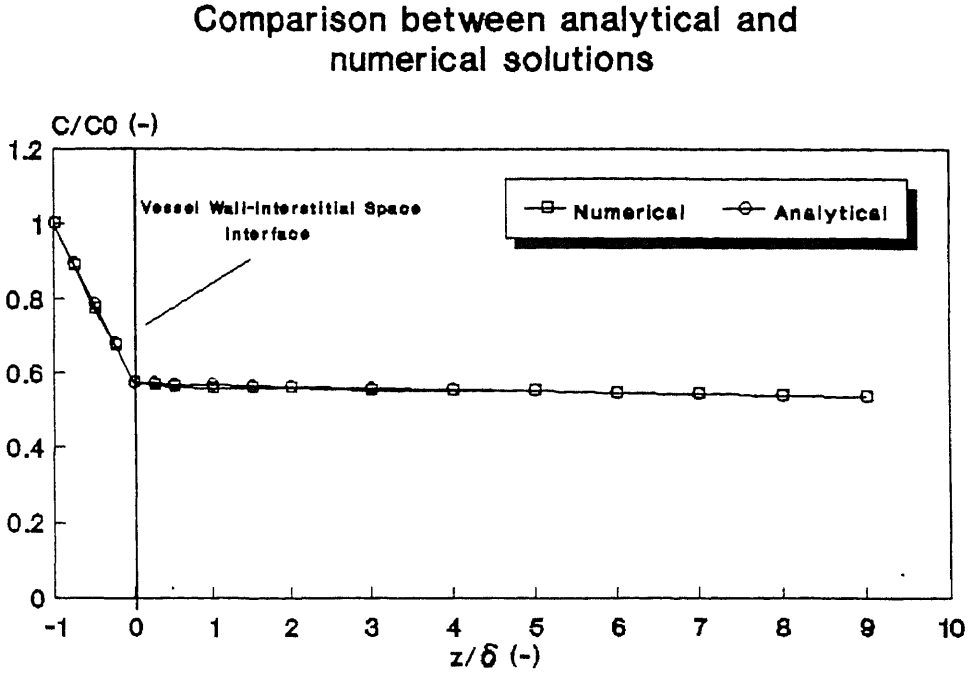

Figure 3.7

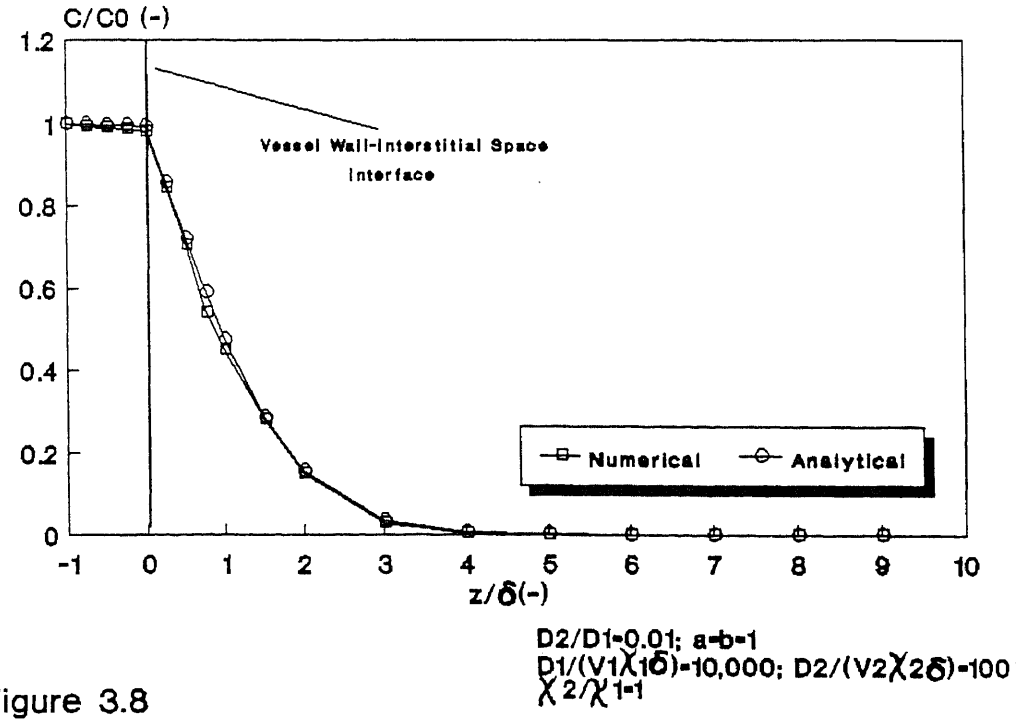

Figure 3.8

Comparison between analytical and numerical solutions

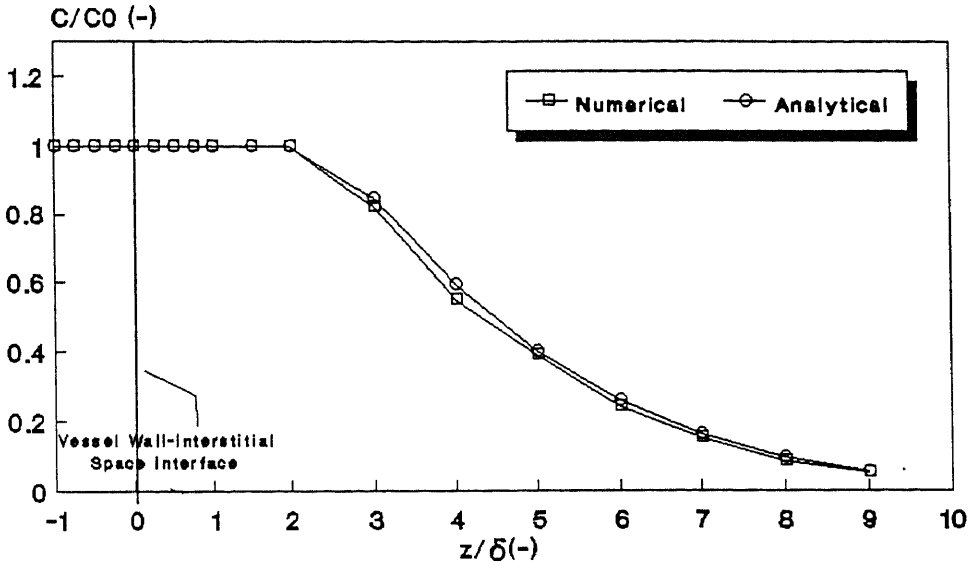

D2/D1=1; a=b=1
D1/(V1χ1δ)=1; D2/(V2χ2δ)=100
χ2/χ1=0.01

Figure 3.9

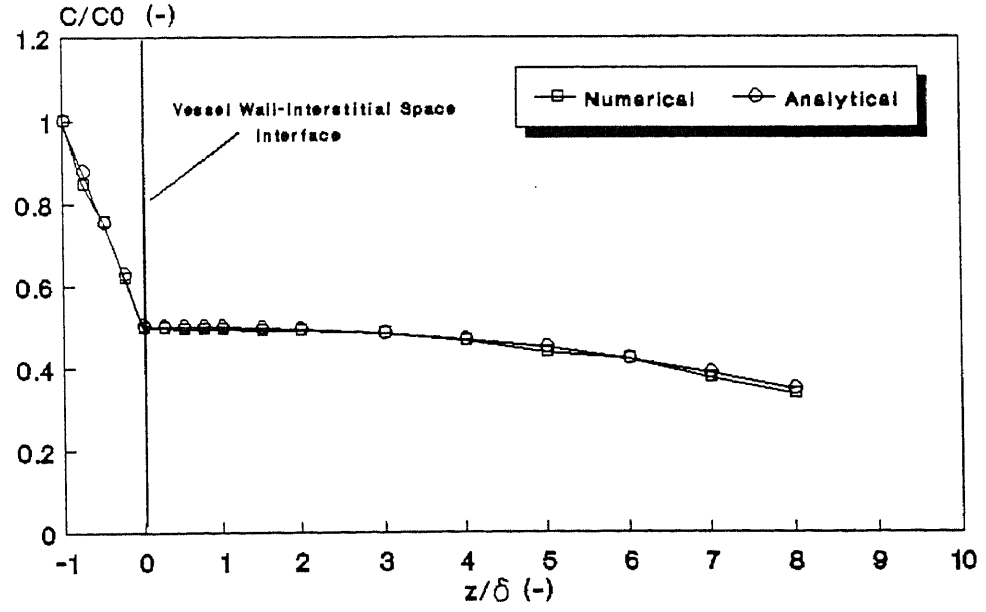

D2/D1=1; a=b=1
D1/(V1χ1δ)=100; D2/(V2χ2δ)=1
χ2/χ1=100

Figure 3.10

$$+\int_{k10}^{\infty} e^{-k4\tau}\,\frac{u^2}{k4}\,\frac{\chi 2V2\ k5k3\ \sin k3 - D2\ k8k3\ \{\frac{k3}{k1}\cos k3-(1-k2)\ \sin k3\}\ \frac{u}{\delta}\ k11}{\{\frac{k3}{k1}\cos k3 - (1-k2)\ \sin k3\}^2+(k6\ \sin k3)^2}\,du\Bigg\}$$

$$+\sum_{n=1}^{m}\frac{(\chi 2V2 + 2D2\Phi)\ k12\ \sin k12\ \ e^{-(k12^2+\ k13^2)\tau}}{(k12^2+\ k1^2)\ (\frac{1}{k12}\cos k12\ \sin k12 - 1 - \frac{k17}{\Phi}\ \sin^2 k12)}$$

$$+\frac{(\chi 2V2 + 2D2q^{\circ}_{2o})\ k15\ \sinh k15\ \ e^{-(k14-k16)\tau}}{(k16 - k14)\ (\frac{1}{k15}\cosh k15\ \sinh k15 - 1 + \frac{k17}{k18}\ \sinh^2 k15)}\Bigg]\,dt \qquad (3.35)$$

The last two terms in this equation are different from zero only if equations (3.31) and (3.32) have any real roots.

Equations (3.30) and (3.33) can be also used to obtain an expression for $\overline{Ns}(t)$, the mass flux into the interstitial space. This can be expressed mathematically as

$$\overline{Ns}(t) = - D2\ \frac{dC2}{dz}\Big|_{z=0} + \chi 2V2C2\Big|_{z=0} \qquad (3.36)$$

The mass flux was calculated as a function of time in the "RESULTS" section.

CHAPTER 4

EXPERIMENTAL METHODS

4.1. Characteristics of the Macromolecular Tracers and Optical System

Fluorescein Isothiocyanate-labeled Dextrans (FITC-Dx) of 70,000 and 150,000 molecular weight (FITC-Dx 70 and FITC-Dx 150) were used as macromolecular tracers. The physicochemical parameters of the FITC-Dxs are shown in Table 4.1. During each experiment, a saline solution containing 5% (by weight) of FITC-Dx was administered intravenously.

Observations were made with an Olympus BH microscope equipped with both bright-field transillumination and epi-illumination using 10X, 32X long working distance objectives and a 10X ocular. Epi-illumination was provided by a 100-W mercury DC lamp source in conjunction with an Olympus FITC exciter filter (488 nm), an Olympus dichroic mirror (DM-500 and O-515), and an Olympus barrier filter (O-515). The recording system comprised a SIT TV camera (MTI, SIT 66) coupled to a real time generator (RCA), a video recorder (Sony, VO2850), and a monochrome video monitor (RCA, TC1217). Video images of microvessels and leakage sites in the interstitial space throughout the course of each experiment were stored on videotape for later frame-by-frame analysis using a video-image digitizer (Quantex, DS20F) operated through a computer (Hewlett Packard, A-900). Photographs were taken with an Olympus PM-10-A photomicrography system using Kodak Tri-X pan film and 50 sec exposures. A schematic diagram of the

Table 4.1. Physicochemical properties of the fluorochromes used in this investigation

Tracer	Mw	Mn	Mw/Mn	E (nm)	$D_{w,37^\circ C}$ ($cm^2/s \times 10^{-7}$)
FITC-Dx 70[a]	71,800	62,100	1.16	5.79	6.10
FITC-Dx 150[b]	152,700	101,100	1.51	8.25	3.97

Mw = weight average molecular weight

Mn = number average molecular weight

E = equivalent Stokes-Einstein radius

$D_{w,37^\circ C}$ = free diffusion coefficient in water at 37°C

[a]Nugent and Jain, 1984.

[b]Nakamura and Wayland, 1975.

optical and recording system is depicted in Figure 4.1 (taken from A. Tomeo, 1991; with permission).

4.2. Adjustment of Camera Gain and Threshold Value (KV)

On the basis of prior experience in the laboratory, a maximum vascular concentration of 3.0 mg/ml of fluorochrome inside a venule (20-50 μm in diameter) was selected for our experiments. This concentration provided sufficient fluorescent intensity to saturate the SIT camera at a gain of 40% of maximum. This is important since the dynamic response of the SIT camera is optimal near the middle of the gain range. FITC-Dx 150 was used for setting the camera gain and threshold value (KV), since its blood-tissue extravasation rate is very low. The camera gain and threshold value (KV) were manually adjusted to give between 0.7 volt peak-to-peak signal and 1 volt peak-to-peak signal from the video camera as measured on an oscilloscope.

4.3. Animal Preparation

Male Golden Syrian hamsters weighing between 80 and 110 g were used. They were initially anesthetized with sodium pentobarbital (60 mg/kg body wt., i.p.). Body temperature was maintained at 37°C with a regulated heating pad. Tracheotomy was performed to facilitate spontaneous respiration. The left carotid artery (PE 50) and jugular vein (PE 10) were cannulated to obtain blood samples, and to inject the tracer and additional doses of sodium pentobarbital.

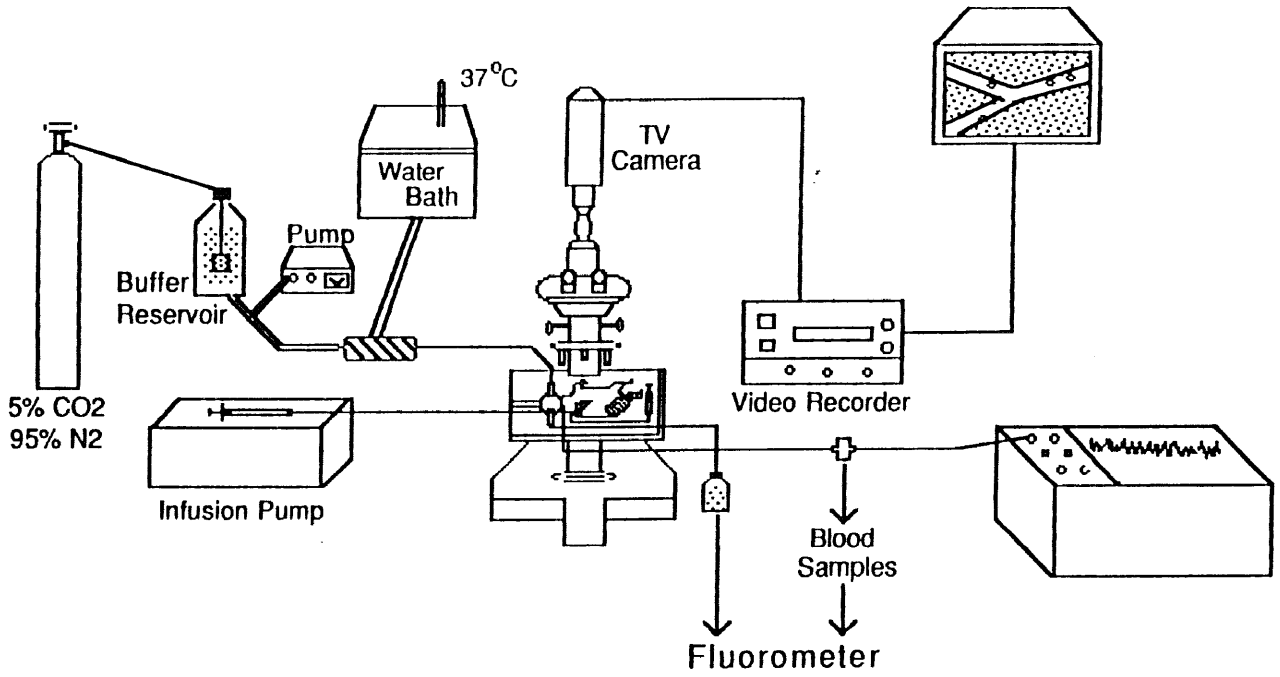

Figure 4.1 Experimental Setup

The right cheek pouch was prepared for fluorescent intravital microscopy as previously described (Mayhan and Joyner, 1984). The skin above the pouch was cut and the epithelium cleared. To prevent damage to the tissue, only a minimal amount of loose connective tissue was dissected away. A Lucite chamber containing a 1-ml reservoir was attached to a single layer of the pouch and secured to the base with the pouch interposed. The seam was sealed externally with a purse string and petroleum jelly to prevent leakage from the reservoir (Gawlowski and Durán, 1986). The hamster was subsequently placed on a Lucite board and mounted on a microscope stage. Figure 4.2 shows the design of the lucite chamber and a scheme of the working preparation (taken from M. Boric, 1985; with permission).

Following surgical dissection and mounting, the preparation was suffused with a 35°C bicarbonate buffered solution (composition in m*M*: 151.8 NaCl, 4.69 KCl, 2.00 $CaCl_2$, 1.17 $MgSO_4$, 20.0 $NaHCO_3$) which was bubbled with 95% N_2 and 5% CO_2 to maintain a low oxygen tension and a pH of 7.35.

4.4. Experimental Protocol for the Determination of the Calibration Curve

After a 20 to 30 minute stabilization period, suffusion was interrupted for a topical application of bradykinin triacetate (Sigma Chemical Co.), which was used to produce transient increases in the rate of blood-tissue transport of large molecules. For this purpose, a bicarbonate buffered solution (pH=7.35) containing 1 μg/ml of bradykinin was applied topically to the microcirculation of the cheek pouch for a period of 5 minutes. After this application period,

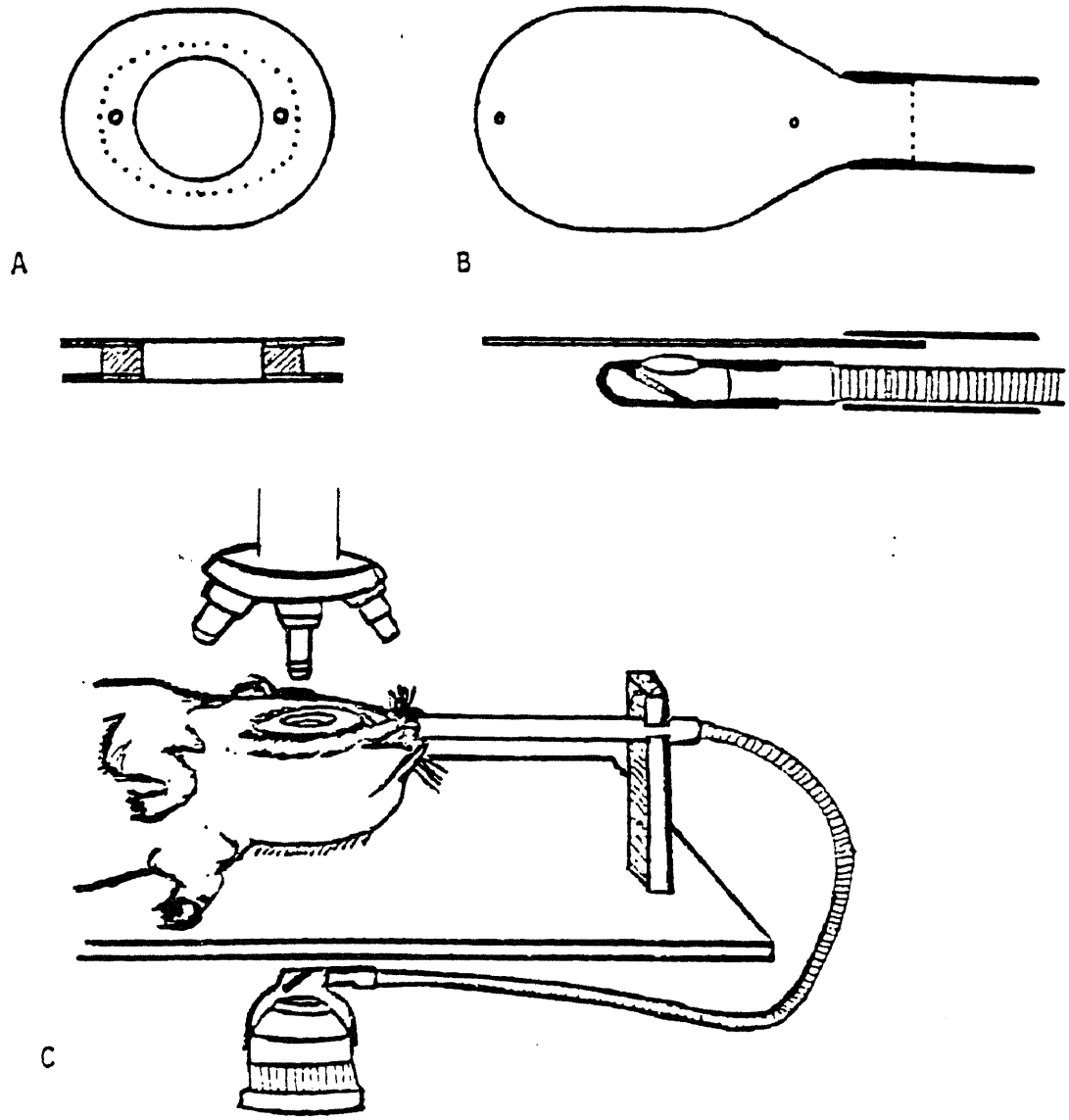

Figure 4.2 Preparation of the Hamster Cheek Pouch.

(A). Top and side views of the observation chamber
(B). Top and side views of the supporting plate and fiber optic cable with its adaptor
(C). A schematic representation of the overall preparation

bradykinin was washed out, and the buffered solution was replaced by mineral oil maintained at 35°C. Mineral oil was selected to prevent swelling of the tissue and the escape of the tracer molecules into the superfusate (Fox and Wayland, 1979). After the substitution of mineral oil, three selected tissue fields and vessels (20-50 μm in diameter) were videotaped to obtain background data. The fields for investigation were the areas around those venules and leakage sites which were relatively free of capillaries and other leaking postcapillary venules.

In each experiment, the FITC-Dx concentration in the vessels was maintained approximately constant by administering a bolus injection (10mg/100g body wt.) immediately followed by a continuous i.v. infusion (10 μl/min).

A different concentration of FITC-Dx 150 or FITC-Dx 70 was used in each experiment to obtain a preselected final concentration in the microvessels. Five minutes after tracer administration, the three selected venules (diameter 20-50 μm) were videotaped in order to obtain the corresponding gray levels (TV camera gain=4.0, KV=3,4,5 for 10x, KV=5,6 for 32x). Up to three sites were studied for each venule. To minimize the deleterious effects of UV light on the preparation, each observation period was limited to a maximum of 45 seconds (Rosenblum, 1978; Hermann, 1983; Bekker *et al.*, 1987). Simultaneously, arterial blood samples were obtained. After centrifugation and hematocrit determination, the samples were diluted with a saline solution (dilution factor 1:1000) and analyzed for FITC-Dx concentration using a Perkin-Elmer LS-3 spectrofluorometer (excitation wavelength: 488 nm; emission wavelength: 515 nm). The

corresponding gray levels and fluorometrically determined concentrations were used to produce a calibration curve for the vascular FITC-Dx concentration.

The following procedure was then used to obtain a calibration curve in the interstitial space. The hamster cheek pouch was allowed to saturate with tracer (approximately 30 minutes for FITC-Dx 70, and 45 minutes for FITC-Dx 150). Three selected saturated fields were videorecorded to obtain the gray levels by digital image processing (TV camera gain=4.0, KV=3,4,5 for 10x, KV=5,6 for 32x). Three saturated sites were studied for each field.

Then, the right carotid artery was cannulated (PE 50) antidromically to flush out the vascular tracer with saline solution. The hamster was sacrificed, and both jugular veins and the left carotid artery were divided to facilitate the intravascular tracer flushing. The cheek pouch microvasculature was flushed for 5 minutes to remove the vascular FITC-Dx. The amount of backflux of tracer macromolecules over this period of time was estimated to be negligible because of their low permeability coefficients (2.4×10^{-7} cm/sec for FITC-Dx 40; Kim *et al.*, 1990). The portion of the hamster cheek pouch contained in the Lucite chamber was cut, weighed, and homogenized using a glass homogenizer. The homogenized tissue was filtered with filter paper (Microporous Filter Co., 0.45 μm), and the amount of tracer measured using a spectrofluorometer. The gray levels and the FITC-Dx concentrations were used to produce a calibration curve for the interstitial space.

During the experiment, each preparation was inspected for the maintenance of tissue integrity. The preparation was discarded if red

blood cells were detected outside the microcirculation, and if spontaneous leakage sites were observed immediately after FITC-Dx administration.

In all of the preparations used for the analysis, the FITC-Dxs appeared in the microcirculation within 40 seconds after injection, and were seen simultaneously in all the vessels in the field of view. Since bradykinin was administered to enhance microvascular permeability, visible leakage sites developed in the interstitial space within 5 minutes after the FITC-Dx injection. The interstitial leakage sites were observed at postcapillary venules with luminal diameters between 14 and 25 μm.

4.5 Experimental Protocol for Macromolecular Transport Studies

i) Macromolecular Transport Studies in the Absence of Calcium Ionophore A23187

After a 20 to 30 minute stabilization period, the buffered solution was replaced by mineral oil maintained at 35°C. After the substitution of mineral oil, three selected tissue fields were videotaped to obtain background data.

In each experiment, the FITC-Dx concentration in the vessels was maintained approximately constant (2mg/ml) by administering a bolus injection (10mg/100g body wt.) immediately followed by a continuous i.v. infusion (10 μl/min) of FITC-Dxs 70 and 150 in concentrations equal to 1.00 and 2.55 mg/ml, respectively. Immediately after the tracer injection, three selected fields were videotaped to obtain gray levels by digital image processing. Recording was repeated at 3-5

minute intervals for approximately 2 hours.

Arterial blood samples were obtained routinely at 5, 15, 30, 60, and 90 minutes to ensure maintenance of a constant FITC-Dx concentration. After centrifugation and hematocrit determination, samples were analyzed for FITC-Dx concentration using a spectrofluorometer.

ii) Macromolecular Transport Studies in the Presence of Calcium Ionophore A23187

After a 20 to 30 minute stabilization period, the suffusion of buffered solution was interrupted for a topical application of calcium ionophore A23187 (Sigma Chemical Co.), which was used to produce transient increases in the rate of blood-tissue transport of large molecules. For this purpose, a bicarbonate buffered solution (pH=7.35) containing 7×10^{-7}M of calcium ionophore A23187 was applied topically to the microcirculation of the cheek pouch for a period of 5 minutes. After this application period, the calcium ionophore solution was washed out, and the buffered solution was replaced by mineral oil maintained at 35°C. Immediately after the substitution of mineral oil, FITC-Dx was administered. After the FITC-Dx administration, all the experimental procedures were same as explained in part *i*).

4.6. Picture Digitization and Development of Mean Gray Scale

Videotapes of each experiment were played back frame-by-frame, and each frame was digitized into x-y arrays of 512 by 512 picture

elements (pixels), using a video-image digitizer. Each pixel was associated with an 8 bit gray level (a number between 0 and 255). The digitized data consisted of the x-y positions of each pixel in the field and their corresponding gray values. The gray values were read from the memory using a computer program (Ritter *et al.*, 1985). Three sites within each frame were selected for further analysis. The size of each site was 10 by 10 pixels.

A measure of the total gray value for a selected site was obtained using the Integrated Optical Intensity (IOI), defined as (Bekker *et al.*, 1989):

$$IOI = \sum_{x}^{nc} \sum_{y}^{nr} D(x,y)$$

where D(x,y) is the intensity (gray level) of a pixel at position x and y, and nc and nr are the total number of columns and rows of pixels chosen from the selected frame. The mean gray level of the site after background subtraction was calculated by dividing ΔIOI values (IOI after background subtraction) by the total number of pixels in it.

The same subregion of the video frame which contained the selected leaking sites was read from different video frames at different time steps. This presented a problem, since small excursions of the leaking site in the video field occurred over time. To compensate for these excursions and to assure reproducibility of the spatial coordinates from frame-to-frame, a "reference point" was chosen in the control frame for each leaking site. This reference point was a well-defined morphological landmark such as a bifurcation which could

be precisely located (± 1 pixel) in each subsequent video frame. For example, in Figures 4.3a and 4.3b, the two subregions of 10x10 pixels had to be positioned so that they coincided exactly. Since the branching points A1 and A2 (Figures 4.3a and 4.3b), in different video frames are common to both fields, points A1 and A2 were selected as a "reference point". The "cursor" subroutine in the IMAGE program was used to define the relative positions of points A1 and A2 (A1(x,y), A2(x,y)) in both frames. Then the position of point X2 in the second frame could be located exactly by adding or subtracting the deviations along the x- and y-axes which were measured in the first frame.

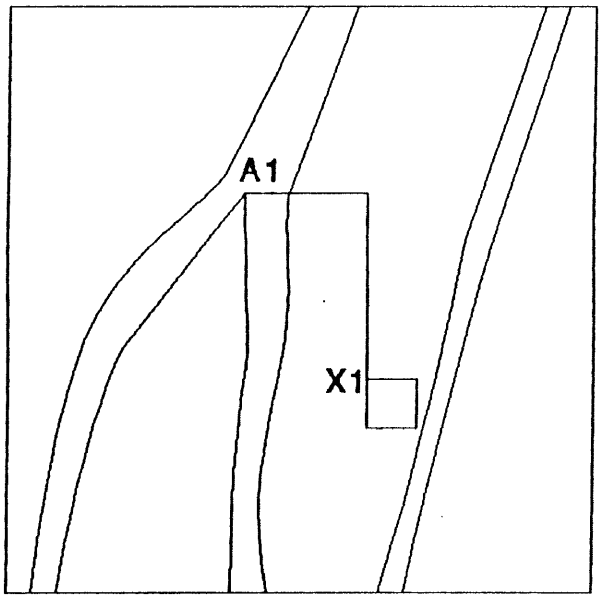

Fig. 4.3a

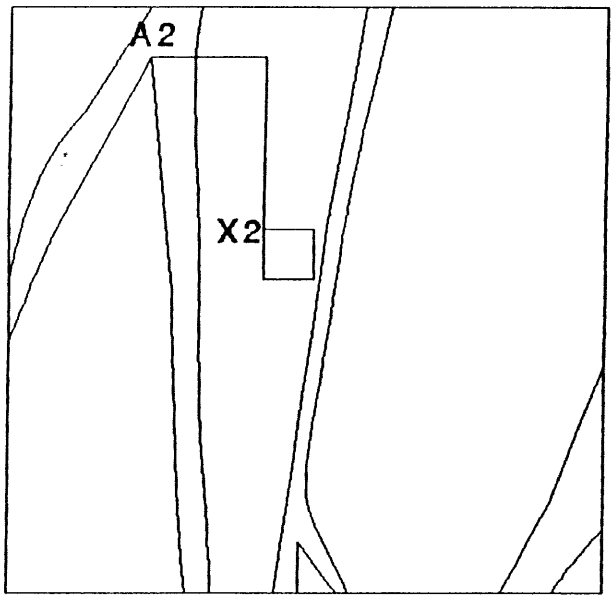

Fig. 4.3b

Position of A1 = (150,150)

Position of X1 = (280,300)

Horizontal Deviation = +130

Vertical Deviation = +150

Position of A2 = (100,50)

Position of X2 = (100+130,50+150)

= (230,200)

CHAPTER 5

RESULTS

5.1. Measurement of Tissue Density

The technique described for the measurement of the FITC-Dx in the tissue enabled us to determine the FITC-Dx concentration expressed in terms of mass of FITC-Dx/mass of tissue. In order to change this unit to mass of FITC-Dx/volume of tissue, we experimentally determined the density of the tissue. A pycnometric technique was used for this purpose. A known mass of tissue was placed in a 10 ml pycnometric bottle of precisely known mass and volume. The bottle was filled with saline solution. By differential weighing (since the density of the saline is known at any given temperature), the volume and density of the tissue were calculated. A tissue density of 1.066 g/cm^3 was obtained using this method. This value agrees well with the density of 1.05 g/cm^3 reported for the rat mesenteric tissue (Barber *et al.*, 1987).

5.2. Calibration Curves

Our determination of tissue density included intravascular, interstitial and cellular volumes. To calculate the concentration of FITC-Dx in the interstitial space, we applied 0.18 as a correction factor for the fraction of extravascular space available to tracer molecules (Bekker *et al.*, 1989). Figure 5.1 shows the relationship between mean gray level and interstitial FITC-Dx concentration obtained with 32x objective. Each point in this figure represents the

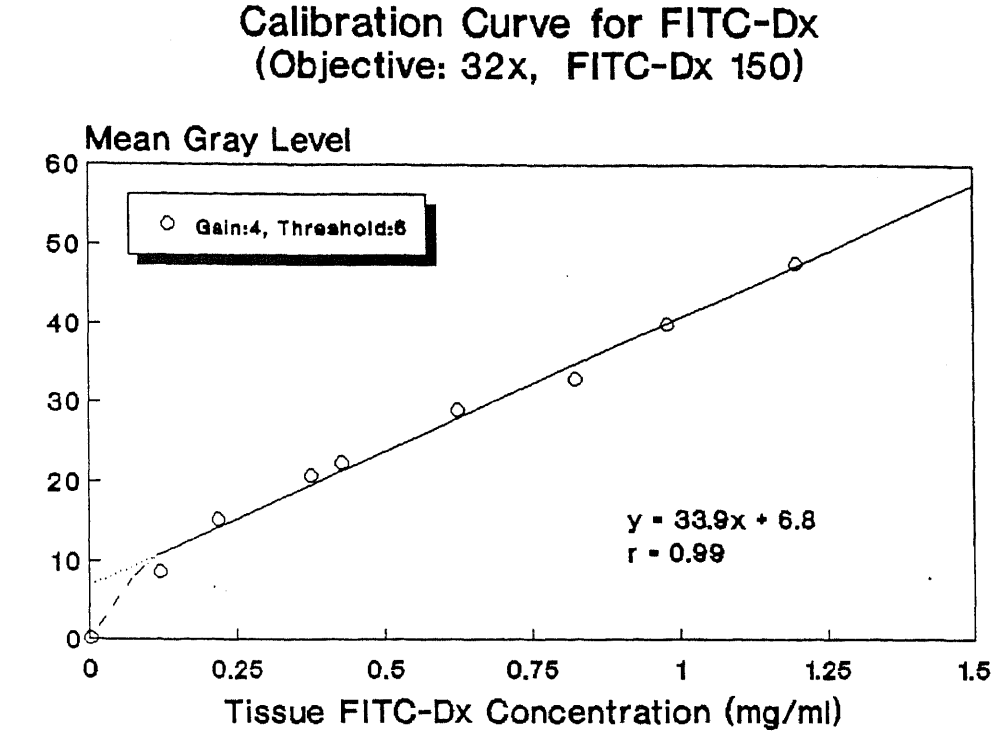
Calibration Curve for FITC-Dx
(Objective: 32x, FITC-Dx 150)
Mean Gray Level
60
50
40
30
20
10
0
Gain:4, Threshold:6
y = 33.9x + 6.8
r = 0.99
0
0.25
0.5
0.75
1
1.25
1.5
Tissue FITC-Dx Concentration (mg/ml)

Figure 5.1

average of nine experimental determinations. For each of the points, the standard deviation was found to be in the range ±1.01 to ±2.31 gray level units. The average standard deviation was found to be ±1.85 gray level units. The measured mean gray levels for investigated interstitial fields at various time were converted to the interstitial FITC-Dx concentrations using this calibration curve. A linear correlation was found over the range from 0.12 to 1.50 mg/ml.

The linear regression equation correlating fluorescence intensity and *interstitial* FITC-Dx 150 concentration (32x objective; gain = 4; KV =6) was found to be

Mean Gray Level = 33.9 [Tissue Concentration (mg/ml)] + 6.8

This equation has a correlation coefficient of 0.993.

In this investigation, the microvascular calibration curves for FITC-Dxs in the interstitial as well as vascular regions were also developed at various threshold values and objectives. Detail of these results are given in Appendix D.

5.3. Experimental Results for Macromolecular Transport Studies

The time course for FITC-Dx extravasation at leakage sites in the absence of calcium ionophore A23187 is shown in Figure 5.2. As time increased more leakage sites developed from the postcapillary venules.

The application of boundary condition (3.4) used in the solution of partial differential equations requires a constant level of tracer

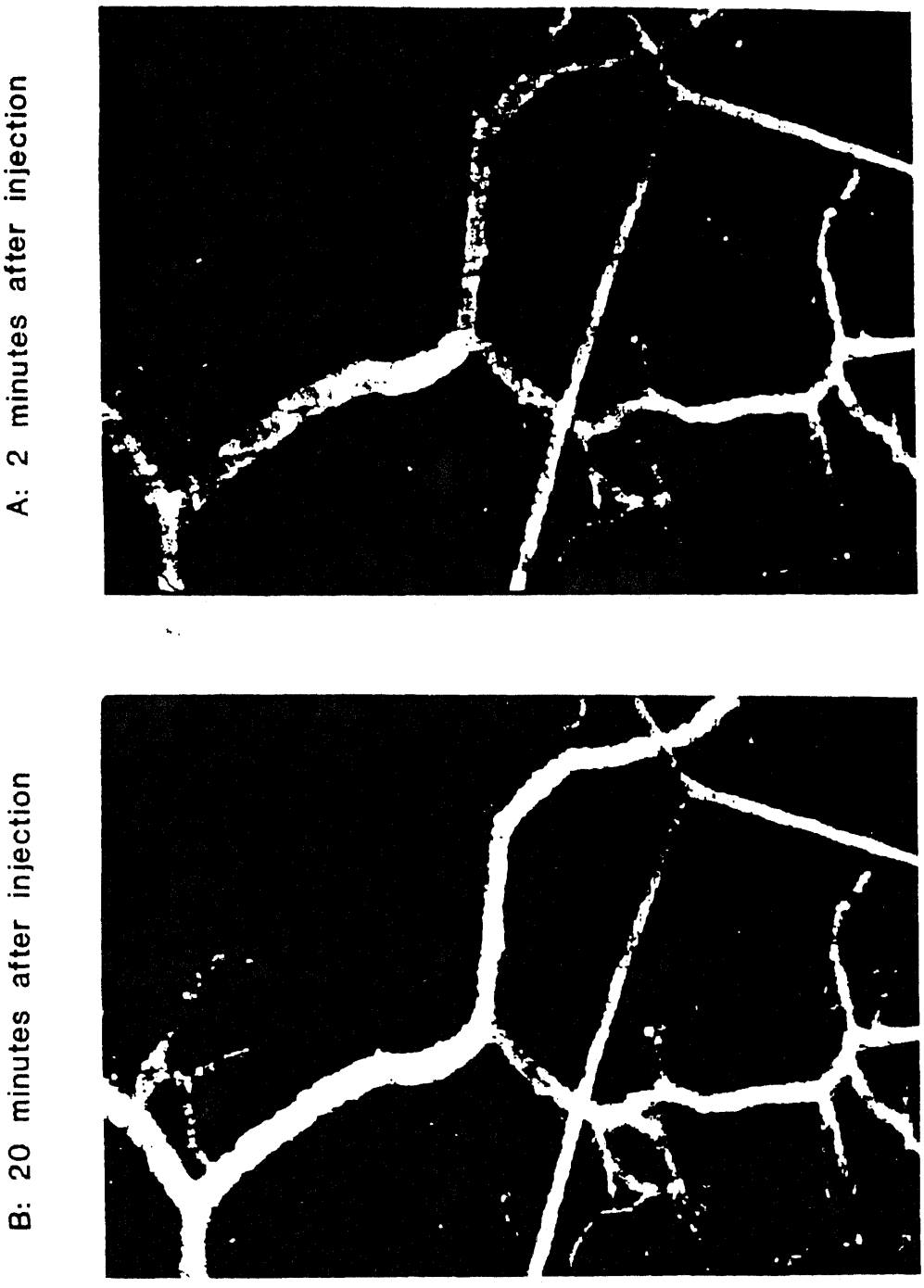

Figure 5.2 Time course of the FITC-Dx extravasation. Pictures are taken at 2, 20, 40 and 60 minutes after tracer injection.

D: 60 minutes after injeotion

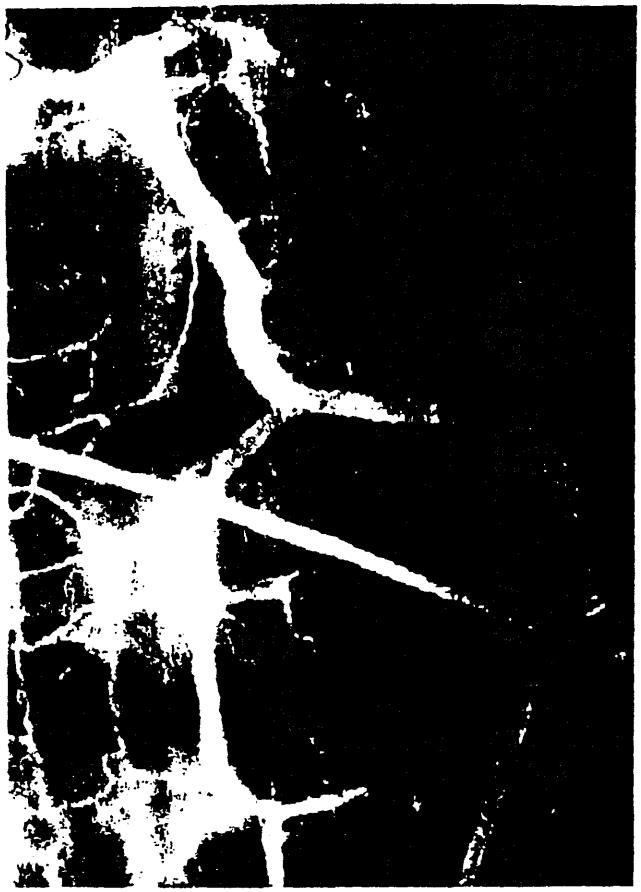

C: 40 minutes after injection

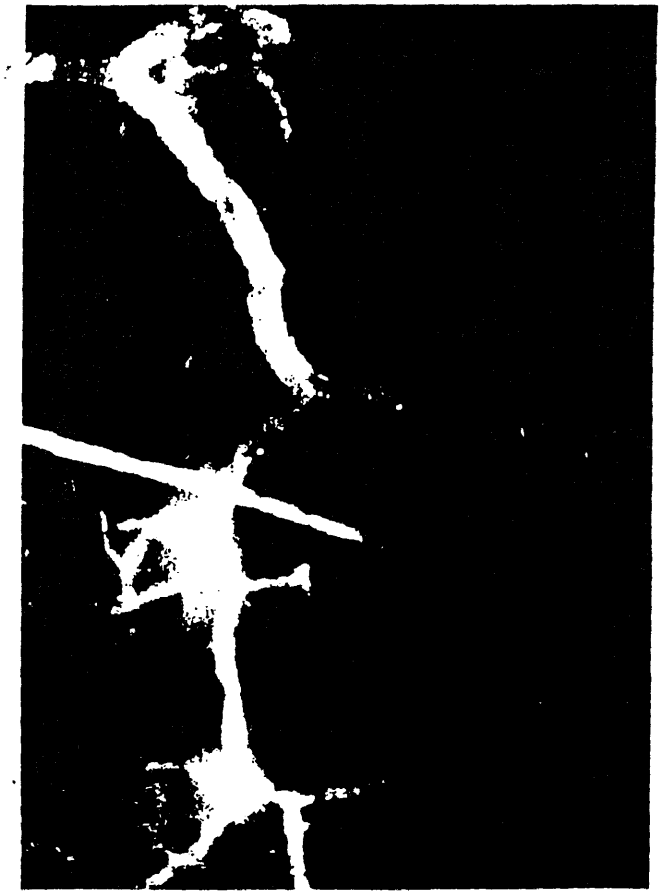

concentration in the plasma. This was accomplished by a bolus injection followed by continuous intravenous administration of the FITC-Dx. The average infusion rate for continuous i.v. infusion of FITC-Dx was about 10 μl/min. The actual infusion rate varied because the available infusion pump was not always able to maintain such a low infusion rate. The level of the tracer concentration in the plasma was monitored by analyzing blood samples obtained from an arterial cannula (Gawlowski and Durán, 1986). Figure 5.3 shows plasma concentration vs. time for two representative experiments. The average concentrations ± standard deviations for the series of experiments conducted are reported in Table 5.1. In all experiments, the maximum deviation of plasma concentration from the average value was less than 15%. This value was taken as an acceptable level for the experimental error.

Tables 5.2-5.5 show a typical raw data log sheet, in which IOI was measured in the interstitial space near the microvascular wall ($z=2.5x10^{-4}$cm). The experimentally obtained discrete values of IOI can directly be utilized for the calculation of concentrations at various times using a calibration curve. These representative set of experimental data showing the time course of the interstitial concentration is also presented in Figure 5.4 for each case. The tracer equilibration in the interstitial space was usually achieved within 1.5 hr. The interstitial FITC-Dx concentrations obtained at various time were then used as the input data for the calculation of transport parameters using the mathematical model. Only the initial portion of the experimental data was used to in our calculations to minimize the effect of extravasation from nearby vessels.

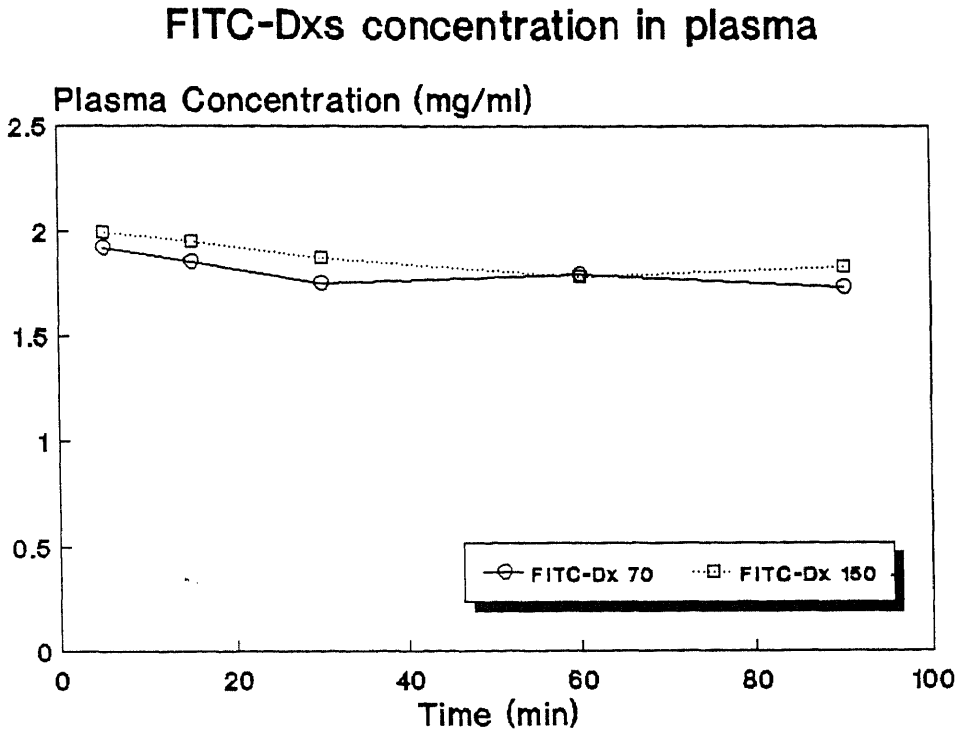
FITC-Dxs concentration in plasma
Plasma Concentration (mg/ml)
2.5
2
1.5
1
0.5
0
0
20
40
60
80
100
Time (min)
FITC-Dx 70
FITC-Dx 150

Figure 5.3

Table 5.1. Plasma concentration of FITC-Dextrans

Experiment	Plasma concentration (mg/ml)
FITC-Dx 70	
1.	1.72±0.21
2.	1.69±0.19
3.	1.74±0.20
4.	1.67±0.23
5.	1.85±0.19
FITC-Dx 150	
1.	1.87±0.14
2.	1.92±0.09
3.	1.89±0.13
4.	1.94±0.07
5.	1.79±0.18

Table 5.2. Results from digital image analysis of the experimental data at various time for Tracer: FITC-Dx 70

Time (sec)	IOI	IOI after background subtraction	Gray level after background subtraction	Concentration (mg/ml)
300	6828	850	8.50	0.050
425	7694	1716	17.16	0.306
732	8127	2149	21.49	0.433
905	8504	2526	25.26	0.544
1215	8899	2921	29.21	0.661
1543	9125	3147	31.47	0.728
1817	9201	3223	32.23	0.750
2111	9389	3411	34.11	0.806
2403	9558	3580	35.80	0.856
2698	9935	3957	39.57	0.967
3015	10067	4089	40.89	1.006
3319	10151	4173	41.73	1.031
3643	10291	4313	43.13	1.072
3905	10445	4467	44.67	1.117
4214	10575	4597	45.97	1.156

Table 5.3. Results from digital image analysis of the experimental data at various time for Tracer: FITC-Dx 150

Time (sec)	IOI	IOI after background subtraction	Gray level after background subtraction	Concentration (mg/ml)
301	6790	812	8.12	0.039
595	7411	1433	14.33	0.222
914	7543	1565	15.65	0.261
1201	7695	1717	17.17	0.306
1497	7807	1829	18.29	0.339
1784	8074	2096	20.94	0.417
2103	8126	2148	21.48	0.433
2395	8146	2168	21.68	0.439
2701	8221	2243	22.43	0.461
3002	8258	2280	22.80	0.472
3295	8373	2395	23.95	0.506
3591	8543	2565	25.65	0.556
3909	8634	2656	26.56	0.583
4255	8672	2694	26.94	0.594
4419	8712	2734	27.34	0.606

Table 5.4. Results from digital image analysis of the experimental data at various time for Tracer: FITC-Dx 70 with calcium ionophore A23187

Time (sec)	IOI	IOI after background subtraction	Gray level after background subtraction	Concentration (mg/ml)
175	7600	1622	16.22	0.278
355	8543	2565	25.65	0.556
541	9011	3033	30.33	0.694
722	9482	3504	35.04	0.833
895	10048	4070	40.70	1.000
1077	10424	4446	44.46	1.111
1254	10614	4636	46.36	1.167
1443	10858	4880	48.80	1.239
1622	11085	5107	51.07	1.306
1798	11197	5219	52.19	1.339
1983	11214	5236	52.36	1.344
2158	11272	5294	52.94	1.361

Table 5.5. Results from digital image analysis of the experimental data at various time for Tracer: FITC-Dx 150 with calcium ionophore

Time (sec)	IOI	IOI after background subtraction	Gray level after background subtraction	Concentration (mg/ml)
184	7224	1246	12.46	0.167
367	7994	2016	20.16	0.394
546	8523	2545	25.45	0.550
718	8712	2734	27.34	0.606
904	8994	3016	30.16	0.689
1084	9333	3355	33.55	0.789
1265	9577	3599	35.99	0.861
1436	9767	3789	37.89	0.917
1621	9858	3880	38.80	0.944
1800	10218	4240	42.40	1.050
1982	10387	4409	44.09	1.100
2162	10519	4541	45.41	1.139
2341	10550	4572	45.72	1.148
2529	10706	4728	47.28	1.194
2703	10821	4843	48.43	1.228

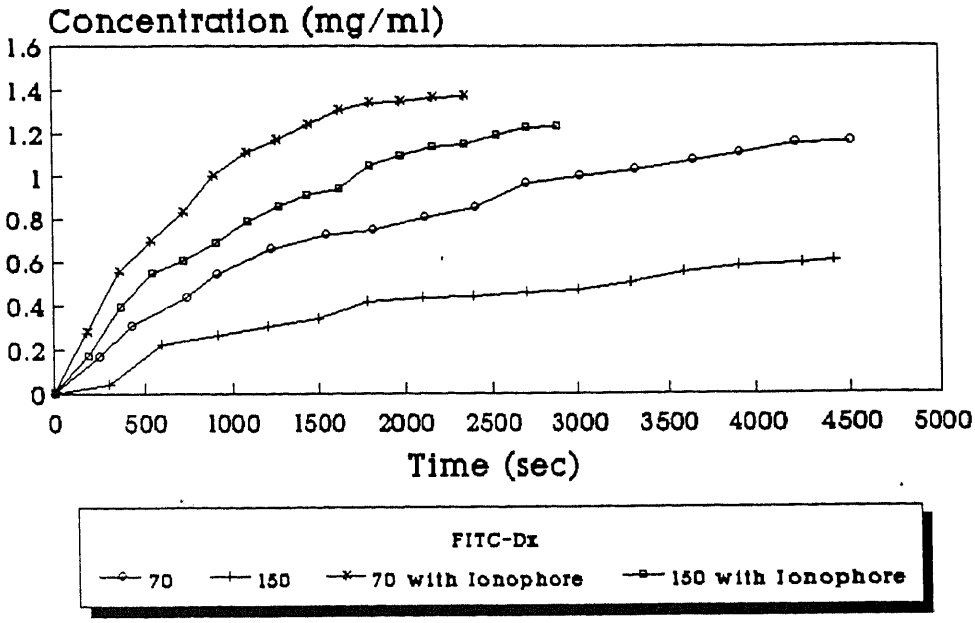

Figure 5.4 Concentration-time profiles

The use of our model in combination with the experimental data required the additional knowledge of several parameters such as the values of the thickness of the wall (δ), the macromolecule concentration in the wall at the plasma-wall interface (Co), the ratio of the cross-sectional areas of the two regions (b), the sieving coefficients (χ_1, χ_2), and the wall-interstitial space equilibrium constant (a). Following Ley and Arfors (1986) we assumed a value for the wall thickness of 0.5 μm in all our computations. We assumed that the macromolecule concentration in the wall at the plasma-wall interface was 2 mg/ml. Ley and Arfors (1986), and Bekker *et al.* (1989) also assumed in their mathematical model that the ratio of the cross sectional areas at the wall-interstitial space interface was equal to 1. Using the same assumption, we imposed that b = 1 in our model. Assuming that the sieving coefficients have the same numerical value in both regions (as better explained below) this also implies that $V_1 = V_2 = V$.

The value of G necessary for the evaluation of equation (3.10) can be derived, in principle, from the a momentum balance for a sphere moving in a long cylindrical tube under Stokes flow conditions. A review of the method used to carry out the corresponding calculations is summarized by Happel and Brenner (1965). According to this reference, for the case in which the ratio γ (radius of molecule/radius of pore) is less than 0.4 the following equation can be used to calculate G

$$G = 1 - 2/3\ \gamma^2 - 0.163\ \gamma^3 \qquad (5.1)$$

Estimates of the size of the large pores for calculation of γ, as reported by different investigators, vary substantially. Taylor *et al.* (1982) calculated the effective pore radii in dog hind paw microvessels to be 195 Å. The results of Joyner *et al.* (1974), however, were consistent with an effective pore radius of about 280 Å. Garlick and Renkin (1970) reported a value of 800 Å in the dog. A value of 300 Å was used in our calculations for both the microvascular wall and interstitial space. This choice is rather arbitrary, but considering the difficulties involved in measuring the size of a large pore, it seemed pointless to attempt to further improve this estimate. Since the radii of the FITC-Dx 70 and FITC-Dx 150 can be estimated to be equal to 57.9 Å and 82.5 Å respectively, the ratio γ was calculated to be 0.193 and 0.275, respectively. Hence, using equation (3.10), the values of the sieving coefficients χ_1 and χ_2 were taken to be both equal to 0.86 and 0.73 for FITC-Dx 70 and FITC-Dx 150, respectively.

The value of the parameter "a" was obtained from equation (3.11) assuming that spherical molecule orientation and shape effects are absent. Then, following the procedure of Giddings *et al.* (1968), equation (3.11) becomes

$$a = (1-\gamma)^2 \tag{5.2}$$

Therefore, the values for a in our case were calculated to be 0.65 and 0.53 for FITC-Dx 70 and FITC-Dx 150, respectively.

Table 5.6 summarizes the values which we used to calculate transport parameters from the experimental data.

In order to search for the values of the transport parameters D_1,

Table 5.6. Parameters used in the determination of transport coefficients from the experimental data

Thickness of the microvascular wall (δ)	0.5 μm
Macromolecule concentration in the wall at the plasma-wall interface (Co)	2.0 mg/ml
Ratio of the cross-sectional areas of the two region (b)	1.0
Sieving coefficients (χ)	0.86 for FITC-Dx 70 0.73 for FITC-Dx 150
Wall-interstitial space equilibrium constant (a)	0.65 for FITC-Dx 70 0.53 for FITC-Dx 150

D_2, and V which best fit the experimental data when interpreted using our mathematical model, we used a RNLIN subroutine program (IMSL, 1986) utilizing the Levenberg-Marquardt optimization algorithm (Levenberg, 1944; Marquardt, 1963). This non-linear regression algorithm is based on the minimization of the sum of squares of the deviations between the experimental data and the theoretical equation, when the transport parameters are used as variables in the optimization process. The computer program which performs these calculations is given in Appendix C.

The values of the transport parameters obtained from the regression were $D_1 = 0.9 \times 10^{-11} cm^2/sec$, $D_2 = 1.29 \times 10^{-8} cm^2/sec$, and $V = V_1 = V_2 = 2.00 \times 10^{-8} cm/sec$ for the case of FITC-Dx 70 in the absence of ionophore.

To test the sensitivity of the RNLIN program to the initial guess for D_1, D_2, and V, the program was run repeatly with several different choices for the initial guess. It was found that the computer program was not much effected by the initial choice, as shown in Table 5.7.

A comparison between the proposed equation best fitted with these transport parameters and the experimental data for each case are shown in Figures 5.5, 5.6, 5.7, and 5.8. The computer program written to do the computations is shown in Appendix C.

This procedure was repeated for each experiment and was used to estimate the diffusivity coefficients and average fluid velocity term for both the microvascular wall and the interstitial space. All the results obtained were shown in Appendix D.

The average and the standard deviations for the transport parameters obtained from the regression for FITC-Dx 70 and FITC-Dx 150

Table 5.7. Sentitivity analysis of the RNLIN program to the initial guesses for D_1, D_2, and V

Initial guess	Result from RNLIN program
$D_1 = 7\times10^{-8}$ (cm^2/s)	$D_1 = 0.90119\times10^{-11}$ (cm^2/s)
$D_2 = 7\times10^{-7}$ (cm^2/s)	$D_2 = 1.29331\times10^{-8}$ (cm^2/s)
$V = 5\times10^{-8}$ (cm/s)	$V = 2.00123\times10^{-8}$ (cm/s)
$D_1 = 1\times10^{-9}$ (cm^2/s)	$D_1 = 0.90125\times10^{-11}$ (cm^2/s)
$D_2 = 1\times10^{-9}$ (cm^2/s)	$D_2 = 1.29351\times10^{-8}$ (cm^2/s)
$V = 1\times10^{-9}$ (cm/s)	$V = 2.00141\times10^{-8}$ (cm/s)
$D_1 = 5\times10^{-9}$ (cm^2/s)	$D_1 = 0.90153\times10^{-11}$ (cm^2/s)
$D_2 = 5\times10^{-9}$ (cm^2/s)	$D_2 = 1.29329\times10^{-8}$ (cm^2/s)
$V = 5\times10^{-9}$ (cm/s)	$V = 2.00117\times10^{-8}$ (cm/s)
$D_1 = 1\times10^{-10}$ (cm^2/s)	$D_1 = 0.90114\times10^{-11}$ (cm^2/s)
$D_2 = 1\times10^{-10}$ (cm^2/s)	$D_2 = 1.29322\times10^{-8}$ (cm^2/s)
$V = 1\times10^{-10}$ (cm/s)	$V = 2.00150\times10^{-8}$ (cm/s)

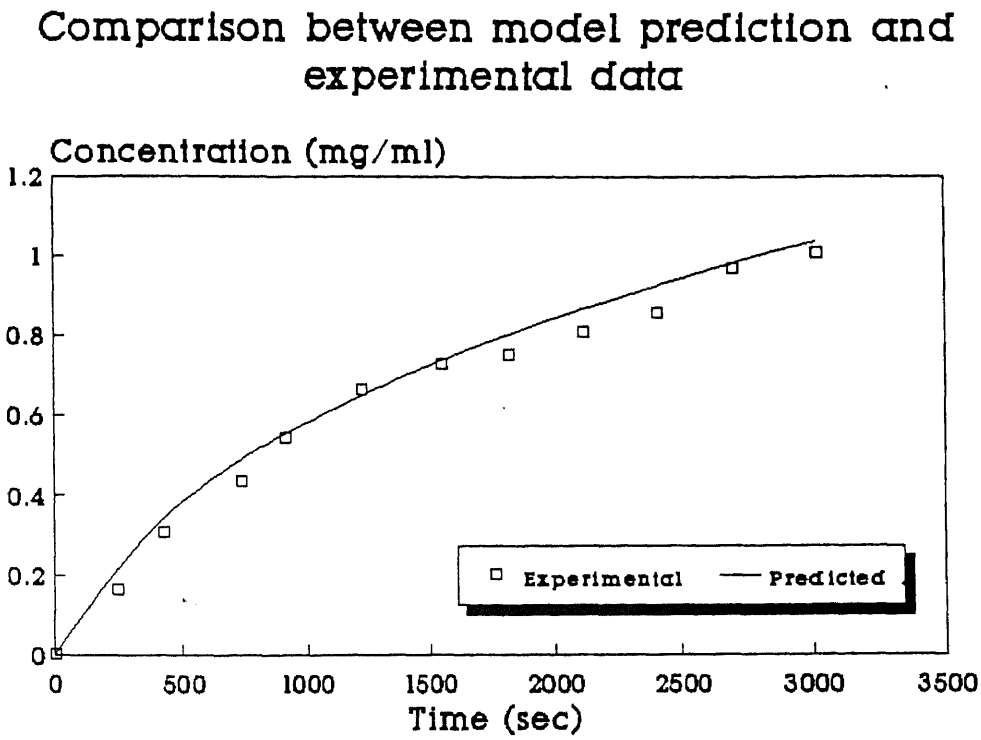

Figure 5.5 FITC-Dx 70

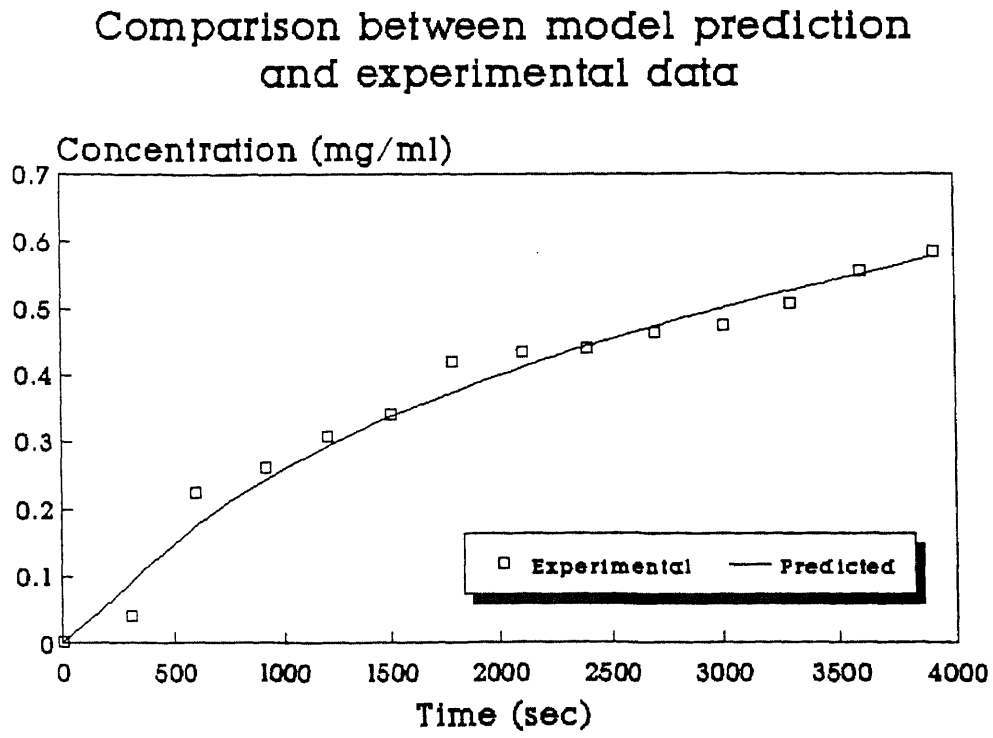

Figure 5.6 FITC-Dx 150

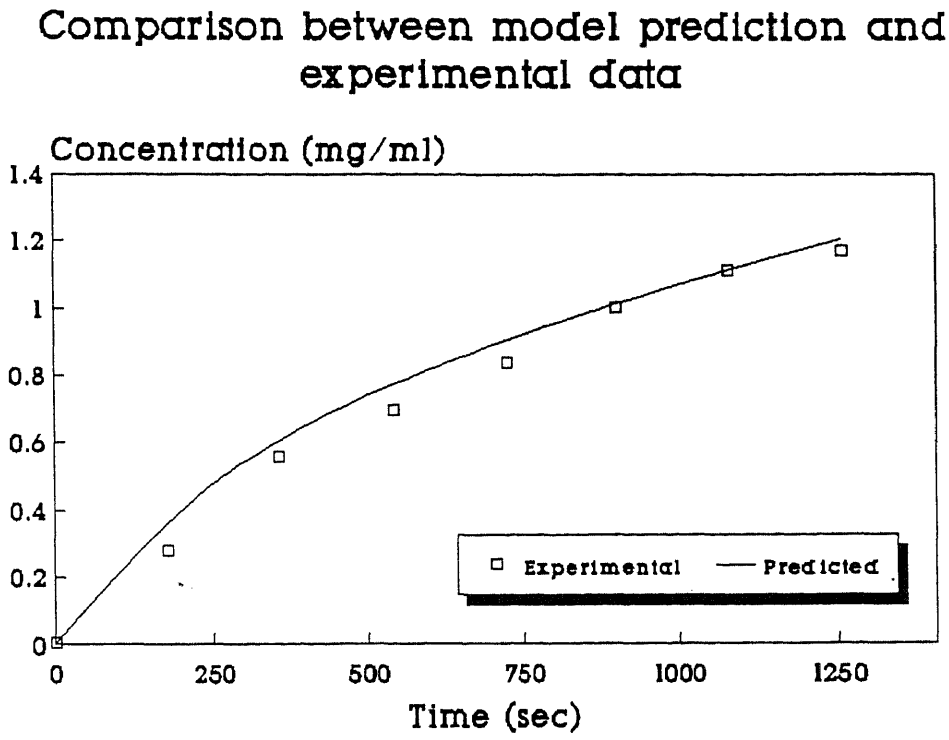

Figure 5.7 FITC-Dx 70 with ionophore

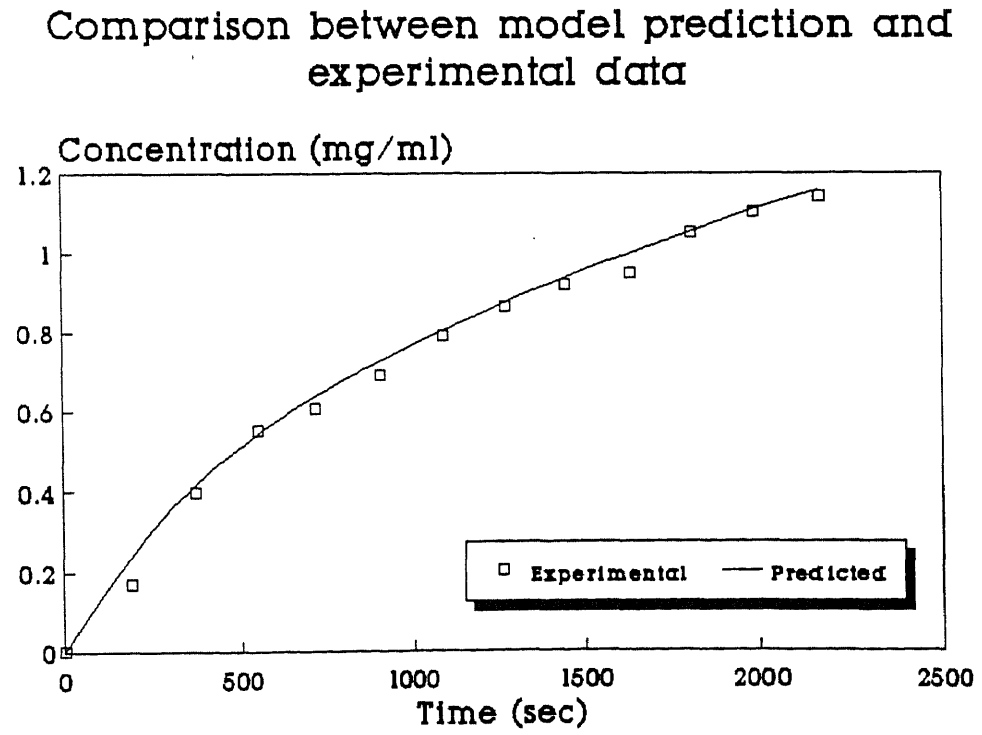

Figure 5.8 FITC-Dx 150 with ionophore

data are given in Table 5.8.

The cumulative amount of macromolecule which has extravasated into interstitial space in a given period of time was calculated using a equation (3.35) for each case as shown in Figure 5.9. The use of equation (3.35) for M(t) requires the value of the mass transfer area. The thickness of the connective tissue was assumed to be 42 μm (Ley and Arfors, 1986; Wiedeman *et al.*, 1981). The value for the length of the capillary vessel used was estimated to be 5 μm. Then, we were able to calculate the mass transfer area which was 210 μm^2. The computer program which performed these calculations is also given in Appendix C.

The mass flux into the interstitial space at various time was calculated using a equation (3.36) as shown in Figure 5.10. The computer program for this calculation is also given in Appendix C.

Table 5.8. Values of the transport parameters obtained from the regression analysis

- **Transport Parameters in Hamster Cheek Pouch without Calcium Ionophore**

Macromolecule	D_1 ($cm^2/s \times 10^{11}$)	D_2 ($cm^2/s \times 10^{8}$)	$V=V_1=V_2$ ($cm/s \times 10^{8}$)
FITC-Dx 70	0.90±0.04	1.29±0.05	2.05±0.05
FITC-Dx 150	0.27±0.02	0.55±0.05	1.71±0.48

- **Transport Parameters in Hamster Cheek Pouch with Calcium Ionophore**

Macromolecule	D_1 ($cm^2/s \times 10^{11}$)	D_2 ($cm^2/s \times 10^{8}$)	$V=V_1=V_2$ ($cm/s \times 10^{8}$)
FITC-Dx 70	1.83±0.05	2.11±0.07	15.7±0.53
FITC-Dx 150	0.83±0.06	1.08±0.14	14.9±1.02

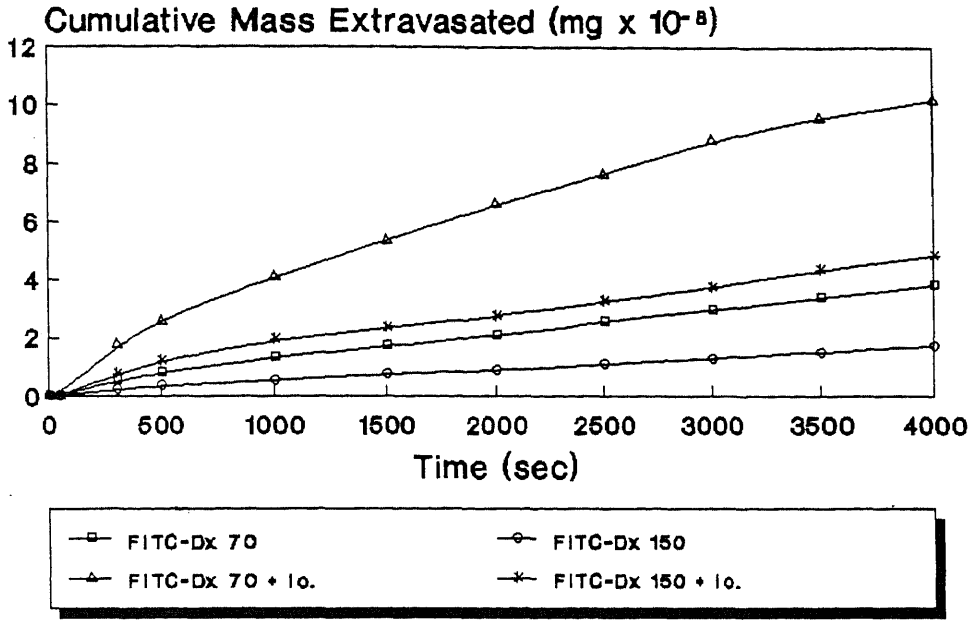

Figure 5.9 Cumulative Mass vs. Time

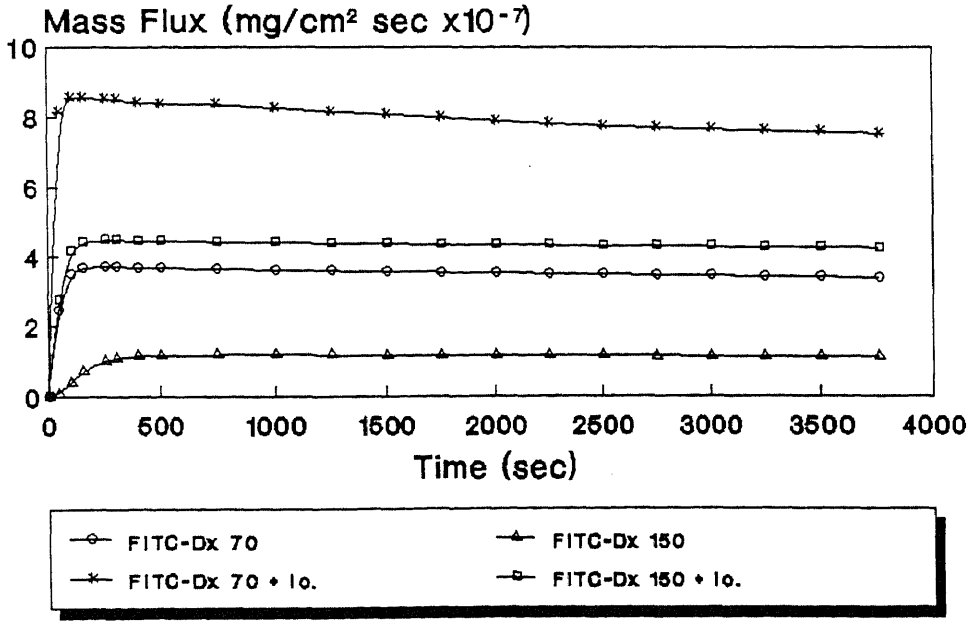

Figure 5.10 Mass Flux vs. Time

CHAPTER 6

DISCUSSION

6.1. Calibration Procedure

Our data demonstrate that a linear relation exists between the fluorescence intensity detected by the SIT TV-microscope combination and both the plasma and the tissue FITC-Dx concentration, when the SIT TV camera is operated in the manual gain mode and at a fixed KV. This linear relationship is reproducible, predictable and qualitatively independent of the magnification used in the observations. The existence of such a relationship validates the use of fluorescent TV intravital microscopy for quantitative measurements, and in particular, for the assessment of microvascular transport of macromolecules.

In order to obtain a linear correlation between intensity and a range of fluorophore concentration, it is important to set the SIT TV camera gain manually at 40% of its maximum. This setting takes advantage of the fact that the dynamic response of the TV camera is optimal near the mid-range of its gain. The system should also be manually adjusted, using an oscilloscope, to yield a 1 volt peak-to-peak signal. The manual setting of the threshold displaces the calibration curve, but does not change the linearity of the system (see Figures D.1-D.8).

We chose to analyze fluorescence intensity as IOI by computer-aided digital image analysis. The use of an integrated intensity should contribute to minimize possible errors associated

with single pixel analysis.

The high correlation coefficients obtained for the vascular and interstitial concentrations of FITC-Dx further prove the linear relationship between TV fluorescent intensity and fluorophore concentration. These observations lend support to the concept that TV microscopy can be used as a fairly good fluorometer (Inoué, 1986).

The linear regression equations were computed over a wide range of FITC-Dx vascular and interstitial concentrations. The data in Figs. D.1-D.8 indicate that a break in linearity may occur at lower concentrations, since the intensity should approach zero as the FITC-Dx concentration approaches zero. In preliminary experiments, Dumrongsiri *et al.* (1990) have been able to extend the linear range of this correlation by instituting changes in gain and KV.

In order to obtain a reliable measurement of the interstitial concentration, one should allow saturation (near equilibration) of the tissue with the test FITC-Dx to occur. In our experiments this saturation was enhanced by the topical application of bradykinin to promote an increased rate of macromolecular extravasation.

The slight discrepancy in correlation coefficient between the equations for FITC-Dx 150 and FITC-Dx 70, emphasizes the need to carry out the calibration procedure with the experimental test macromolecule. Since the intensity is a function of the mass of excited and emitting FITC molecules, the difference in correlation coefficients may be due to different substitution rates or different total number of FITC molecules in the two test dextrans.

6.2. Macromolecular Transport

The values of the transport parameters obtained from the regression of the experimental data in the hamster cheek pouch (Table 5.8) when fitted to our model appear to decrease as the size of the transported solute increases. The magnitudes of the calculated unsteady-state transported parameters and their inverse correlation with molecular size are consistent with the idea the transport pathways of these macromolecules are not just water-filled channels. The current thinking is that blood-tissue transport pathways contain a network of fibrous material that restricts free diffusion and reduces the magnitudes of both the diffusive and convective mechanisms in proportion to the size, shape, and charge of the solute (Curry, 1986).

An increased vascular permeability to fluid and macromolecules is often associated the appearance of large gaps between the endothelial cells of the venules in electron micrographs. It has been suggested (Majno *et al.*, 1969) that the gaps are the pathways responsible for the increased permeability, and that they are formed by the contraction of adjacent endothelial cells. To investigate whether intercellular gaps can be generated by a rise in Ca^{2+} within the endothelium, Michel and Phillips (1984) measured the permeability of single frog capillaries in the absence and presence of the ionophore A23187 which they believed might raise Ca^{2+} within the endothelium. They found that A23187 increased the vascular permeability independently of mast cells and possibly by a direct action on the endothelium. Therefore, the transport parameters in the presence of

calcium ionophore A23187 are always higher than the corresponding parameters in the absence it. This conclusion appears to be validated by our results.

In addition, the results obtained here in the absence and in the presence of ionophore indicate that the values of the diffusion coefficients in the microvascular wall are three orders of magnitude smaller than the corresponding values in the interstitial space.

Table 6.1 shows the relative contribution of molecular diffusion and convective transport in the overall transport process. These results show that the transport in the microvascular wall was the limiting transport mechanism, at least for the data set considered in this work. Within the microvascular wall, it appeared that the molecular diffusion mechanism dominated over convective transport. However, the convection mechanism transport in the presence of calcium ionophore increased about three times compared to the corresponding value in the absence of calcium ionophore.

The relative importance of these two mechanisms varies depending on the time elapsed and, more significantly, on the position within the wall. It was found that convection accounts for approximately 9.37% of the total mass flux for positions in the wall closer to the plasma-wall interface when FITC-Dx 70 was used. However, for positions in the interstitial space closer to the wall-interstitial space interface, convection accounted for 0.42% only. These changes in the relative importance of the transport mechanisms can be attributed primarily to the sharply decreasing concentration profile within the microvascular wall, since the concentration directly affects the convective flux, $\kappa_1 V_1 C_1$, and indirectly (through the

Table 6.1. Relative contribution of molecular diffusion and convective transport

• **In the wall, next to the plasma-wall interface** ($z = -5x10^{-4}cm$)

Macromolecule	Diffusion $(-D_1(\partial C_1/\partial z))$ mg/sec cm^2	Convection $(\chi_1 V_1 C_1)$ mg/sec cm^2	Diffusion (%)	Convection (%)
FITC-Dx 70	$3.33x10^{-7}$	$3.44x10^{-8}$	90.63	9.37
FITC-Dx 150	$1.05x10^{-7}$	$2.14x10^{-8}$	83.11	16.89
FITC-Dx 70*	$6.87x10^{-7}$	$2.70x10^{-7}$	71.79	28.21
FITC-Dx 150*	$4.16x10^{-7}$	$2.14x10^{-7}$	66.05	33.95

• **In the wall, next to the wall-interstitial space interface** ($z \rightarrow 0^{-}cm$)

Macromolecule	Diffusion $(-D_1(\partial C_1/\partial z))$ mg/sec cm^2	Convection $(\chi_1 V_1 C_1)$ mg/sec cm^2	Diffusion (%)	Convection (%)
FITC-Dx 70	$3.65x10^{-7}$	$1.54x10^{-9}$	99.58	0.42
FITC-Dx 150	$1.27x10^{-7}$	$3.74x10^{-10}$	99.71	0.29
FITC-Dx 70*	$9.45x10^{-7}$	$2.16x10^{-8}$	97.76	2.24
FITC-Dx 150*	$6.54x10^{-7}$	$1.03x10^{-8}$	98.44	1.56

• **In the interstitial space, next to the wall-interstitial space interface**($z \rightarrow 0^{+}cm$)

Macromolecule	Diffusion $(-D_1(\partial C_1/\partial z))$ mg/sec cm^2	Convection $(\chi_1 V_1 C_1)$ mg/sec cm^2	Diffusion (%)	Convection (%)
FITC-Dx 70	$3.59x10^{-7}$	$2.37x10^{-9}$	99.34	0.66
FITC-Dx 150	$1.16x10^{-7}$	$7.05x10^{-10}$	99.40	0.60
FITC-Dx 70*	$7.99x10^{-7}$	$3.36x10^{-8}$	95.51	4.49
FITC-Dx 150*	$4.15x10^{-7}$	$1.95x10^{-8}$	95.60	4.40

* Calcium ionophore applied to the hamster cheek pouch

derivative) the molecular diffusion flux, $D_1(\partial C_1/\partial z)$.

The effective permeability coefficient in the microvascular wall was calculated as:

$$P = \bar{N}/\Delta C$$

where $\bar{N}$ is the mass flux and ΔC is the concentration difference between one side of the microvascular wall and the other. The computer program which performed these calculations is given in Appendix C.

Table 6.2 shows the permeability values we obtained, and a comparison with the corresponding values determined by other workers. The effective permeability values of FITC-Dx 70 and FITC-Dx 150 as reported by Baxter *et al.* (1987) and Garlick and Renkin (1970) are about twenty times higher for FITC-Dx 150 and about four times higher for FITC-Dx 70 than the corresponding values determined by this investigation. This might be due to the different of method to measure the effective permeability. The value of FITC-Dx 150 as reported by Gerlowski and Jain (1986) is slightly higher than the value we measured. They used a one-dimensional diffusion model to estimate P value. This value was included the convective contribution of FITC-Dx 150 transport.

The values for the diffusivity coefficients in the interstitial space obtained in the absence of ionophore on hamster cheek pouch compare favorably with the results previously obtained by other workers in similar systems, as shown in Table 6.3. A comparison of the average fluid velocity terms obtained in this work with

Table 6.2. Effective permeability of macromolecule in microvascular wall

Solute	Method	Tissue	E (Å)	P x 10^{-8} (cm)	Reference
Dextran	Steady state lymph data	Dog paw			Garlick and Renkin (1970)
Dx 40			49.0	2.23	
Dx 80			61.5	1.71	
Dx 110			71.5	1.03±0.03	
Dx 150			82.5	0.26	
Albumin	Steady state lymph data	Dog paw	35.5	4.64±0.50	Carter *et al.* (1974)
Haptoglobulin			46.0	3.13±0.50	
γ-Globulin			56.0	3.25±0.44	
Dextran 110			71.5	1.13±0.16	
Dextran 150	Intravital microscopy	Rabbit ear	82.5	7.26±3.29	Gerlowski and Jain (1986)
Dextran 70	Transient analysis of superfusate	Hamster cheek pouch	60.0	4.1	Baxter *et al.* (1987)
α-Lactalbumin	Photo-densitometry	Frog mesentery	20.2	210.0-400.0	Huxley *et al.* (1987)
Dextran 70	Intravital microscopy	Hamster cheek pouch	56.8	18.0±0.8	This Work
Dextran 150			82.5	5.5±0.4	

Table 6.3. Comparison of the diffusion coefficients obtained in this study with the results obtained by other workers

Solute	Interstitial space ($cm^2/sec \times 10^8$)	Reference
FITC-Dx 40	1.70	Kim *et al.* (1990)
	2.00	Nugent and Jain (1984)
	1.80	Fox and Wayland (1979)
FITC-Dx 70	1.31	This work
	1.35	Baxter and Jain (1988)
	0.61	Nugent and Jain (1984)
FITC-Dx 150	0.53	This work
	24.0	Nakamura and Wayland (1975)

experimental data could not be carried out, however, since no data were available.

6.3. Interpretation of Transport Coefficients

i) Pore Theory

The pore hypothesis (Pappenheimer, 1951) was first used to describe the selectivity property of blood-tissue transport barriers to various small solutes and water. In the pore model, the ratio of solute radius to pore radius are used to describe the permeability and selectivity properties of the microvascular blood-tissue barrier.

In order to further analyze the diffusivity coefficients obtained in this investigation, the pore theory defines a parameter which is equivalent to the diffusivity coefficient determined in our experiment as:

$$D_P = (1-\alpha)^2 \quad F(\alpha) \quad D_W \qquad (6.1)$$

where, α: aspect ratio (= E/R_P)

E: the equivalent radius of a spherical solute

R_P: the pore radius

$F(\alpha)$ is a hydrodynamic function, defined as (Curry, 1984)

$$F(\alpha) = 1 - 2.104\ \alpha + 2.088\ \alpha^3 - 0.95\ \alpha^5$$

D_P: the restricted diffusion coefficient of the solute in the pore

D_W: the free diffusion coefficient of the solute

The functional relationship between D_P/D_W and α is based on a

hydrodynamic model developed by Faxen(1959) and is accurate for values of α up to 0.6 (Curry, 1984). Other empirical relationships have been developed for $F(\alpha)$, which are claimed to be accurate for higher values of α (Paine and Scherr, 1975).

For large solutes (between 30Å and 60Å) passing through a system of large pores ($R > 200Å$) α is less than 0.3. The corresponding values of the hydrodynamic function $F(\alpha)$ are greater than 0.4. The diffusivity coefficients calculated from our experimental data are at least three orders of magnitude lower than those predicted by equation (6.1) as shown in Table 6.4. The disagreement between our results and the prediction of the pore theory can be explained by the following considerations. The parameters commonly used in the pore theory to describe solute transport, the hydraulic conductivity, L_p and the permeability coefficient, P, are given by the following expressions:

$$L_p = \frac{N_p \pi R_p^4}{S \delta 8\eta} \tag{6.2}$$

where, N_p: number of pores

S: surface area

η: viscosity

and

$$P = \frac{N_p \pi R_p^2}{S \delta} \phi D_p \tag{6.3}$$

where, ϕ: partition coefficient

Equations (6.2) and (6.3) include pore density (N_p/S) as a parameter. The numerical values of L_p and P are usually determined from steady

Table 6.4 Comparison between the pore theory and the fiber-matrix theory using the determined diffusivity coefficients in the microvascular wall found in this study

Macromolecule	D_1 (this work) cm^2/sec	D_1 (pore theory) cm^2/sec	D_1 (fiber-matrix) cm^2/sec
FITC-Dx 70	0.90×10^{-11}	2.41×10^{-7}	0.21×10^{-11}
FITC-Dx 150	0.27×10^{-11}	9.68×10^{-8}	0.29×10^{-12}

state whole organ experiments where the measured variable is the total solute flux. In such a treatment, any erroneous assumption about the flow regime within the pore will be corrected by selecting the right value of pore density.

ii) Fiber-Matrix Theory

One of the most compelling reasons to investigate new mechanisms to account for the permeability properties of the capillary wall is the major inconsistency found when the pore theory is used to analyze experimental data describing the permeability and selectivity of the capillary wall. The equivalent pore radius that describes the selectivity of the capillary wall is smaller than the equivalent pore radius that describes the hydraulic conductivity and small solute permeability of the capillary wall (Crone and Levitt; 1984, Curry; 1984). The problem arises in all capillaries with continuous endothelium, including those in skeletal muscle, lung, heart, and frog mesentery. For example, in frog mesentery, the reflection coefficients to albumin and myoglobin are accounted for by an equivalent pore radius of 5.5 nm, but the hydraulic conductivity of the wall is accounted for by an equivalent pore radius 8 nm. Because of the inconsistency of the pore model, Michel (1978,1980) reintroduced the hypothesis of a three-dimensional network of fibrous molecules within the transcellular pathways. The hypothesis was that this fibrous network acted as the principal determinant of the selectivity of capillary transport barrier. Curry and Michel (1980) then derived the equations that described the transport parameters

within a transport pathway containing a random array of cylindrical fibers in terms of the fiber radius (R_f) and the void volume, ε (=the volume occupied by aqueous solution). The description of transport coefficients using the fiber matrix model resolved the inconsistency brought about by the equivalent pore hypothesis.

The interpretation of restricted diffusion in the fiber-matrix model is based on the equations describing diffusion of a molecule through a random array of fibers of molecular dimensions as described by Ogston *et al.*(1973). The diffusivity coefficient can be expressed as a product of the effective diffusion coefficient in the matrix and a steric exclusion factor:

$$D_m = \exp\left[-(1-\varepsilon)\left\{\frac{2E}{R_f} + \left(\frac{E}{R_f}\right)^2\right\}\right] \cdot D_w \cdot \exp\left[-\left\{(1-\varepsilon)^{0.5}(1+E/R_f)\right\}\right] \quad (6.4)$$

where D_m: the diffusion coefficient of the solute in the matrix

D_w: the free diffusion coefficient of the solute

ε : the void volume that equals one minus the fiber volume;

$= 1 - \pi R_f^2 L$ (L is fiber length per unit volume)

E: the equivalent radius of a spherical solute

R_f: the fiber radius

The selectivity of a microvascular wall is a function of the size and concentration of fibrous molecules in the membranous space available for solute transport. The numerical values of these parameters, however, are not known a priory, and are determined by matching permeability data obtained experimentally. Curry and Huxley

(1982) used the fiber matrix model to analyze the transport coefficients measured in single capillaries and whole organs. The calculations showed that in the frog mesenteric capillaries, fibers 0.6nm in radius (the radius of a sulphated proteoglycan) which occupy 5% of the transport pathway volume are able to explain the restricted diffusion of solutes. Using these values, the diffusivity coefficients calculated for each of FITC-Dxs are reported in Table 6.4. Our result can be explained reasonably well by the fiber-matrix theory. However, no single set of R_f and ε can satisfactory predict the diffusivity coefficients for all cases.

CHAPTER 7

SUMMARY AND CONCLUSIONS

1. Fluorescent intravital microscopy in combination with digital image processing offers a convenient method to study the dynamics of macromolecular transport *in vivo.*
2. A one-dimensional, unsteady-state mathematical model was developed to describe the transfer of macromolecules across a microvascular wall and into the interstitial space. The model so developed accounts for both molecular diffusion and convective transfer through the microvascular wall as well as in the interstitial space.
3. A new calibration procedure to convert from digital image processing data to interstitial concentrations at various times was developed in this work. This procedure offers the advantage of determining the time course of tracer extravasation in a form amenable to quantitative analysis.
4. Experimental data obtained from digital image processing were analyzed using the developed model. Diffusivity coefficients and average fluid velocity terms for FITC-Dx 70 and FITC-Dx 150 in the absence and presence of the calcium ionophore A23187 were calculated by matching the experimentally obtained and the theoretically predicted values. Transport parameters were estimated using a non-linear regression method. The diffusivity coefficients for FITC-Dx 70 were found to be $0.90\pm0.04\times10^{-11}$ cm^2/s in the microvascular wall, and $1.29\pm0.05\times10^{-8}$ cm^2/s in the

interstitial space. The average fluid velocity term in both regions was found to be $2.05\pm0.05\times10^{-8}$ cm/s. The corresponding transport parameters for FITC-Dx 150 were $0.27\pm0.02\times10^{-11}$ cm^2/s, $0.55\pm0.05\times10^{-8}$ cm^2/s, and $1.71\pm0.48\times10^{-8}$ cm/s, respectively. Using a similar experimental procedures, the extravasation of FITC-Dx 70 and FITC-Dx 150 was experimentally determined after a 5-minute topical application of calcium ionophore A23187 (7×10^{-7} M). In this case, the diffusivity coefficients for FITC-Dx 70 were found to be $1.83\pm0.05\times10^{-11}cm^2/s$ in microvascular wall, and $2.11\pm0.07\times10^{-8}$ cm^2/s in the interstitial space. The average fluid velocity term was $15.7\pm0.53\times10^{-8}$ cm/s in both regions. The corresponding transport parameters for FITC-Dx 150 were $0.83\pm0.06\times10^{-11}cm^2/s$, $1.08\pm0.14\times10^{-8}$ cm^2/s, and $14.9\pm1.02\times10^{-8}$ cm/s, respectively.

5. The diffusivity coefficients and average fluid velocity terms in the presence of the calcium ionophore A23187 were found to be approximately two times and eight times higher, respectively, than the corresponding parameters obtained in the absence of it.
6. The diffusivity coefficients and average fluid velocity terms were used to quantify the role of the convective and diffusive components on the total solute flux through the microvascular wall and into the adjoining interstitial space. It was shown that the relative contributions of the two major transport mechanisms, diffusion and convection, on macromolecular blood-tissue transport depend on the molecule, the time elapsed and, more significantly,

on the position.

7. The macromolecular transport in the microvascular wall was the limiting transport mechanism for the entire process. Within the microvascular wall, it appeared that the molecular diffusion mechanism dominated over convective transport for all cases considered. However the convection mechanisms in the presence of calcium ionophore A23187 increased about three times compared the corresponding values in the absence of calcium ionophore A23187. Within the interstitial space, diffusion appeared to be the dominating transport mechanism for all cases.
8. The experimentally determined transport parameters were examined in view of two previously proposed hypotheses of macromolecular permeability. Our calculations show that the fiber-matrix theory, which postulates that solute transport rate and selectivity are regulated by the size and concentration of fibrous molecules in a channel, can be used to describe macromolecular transport. The pore theory, which was originally developed to describe capillary permeability of small solutes, fails to predict parameters of macromolecular transvascular exchange.
9. The mathematical model and the calibration procedure developed in this investigation are useful tools to provide better understanding of the dynamics of macromolecular transport across the microvascular wall and into the adjoining interstitial space.

REFERENCES

Anderson J.L., and Quinn, J.A., Restricted transport in small pores. *Biophys. J.* **14**, 130-150 (1974).

Arfors, K.E., Rutili, G., and Svensjo, E., Microvascular transport of macromolecule in normal and inflammatory conditions. *Acta. Physiol. Scand. Suppl.* **463**, 93-103 (1979).

Branemark, R.I., Ekholm, R., and Lindhe, J., Colloidal carbon used for identification of vascular permeability. *Med. Exp.* **18**, 139-150 (1968).

Barber, B.J., Oppenheimer, D.C., and Zimmermann, H.A., Variations in rat mesenteric tissue thickness due to microvasculature. *Am. J. Physiol.* **253**, G549-G556 (1987).

Baxter, L.T., Jain, R.K., Vascular permeability and interstitial diffusion in superfused tissues: A two-dimensional model. *Microvasc. Res.*, **36**, 108-155 (1988).

Baxter, L.T., Jain, R.K., and Svensjo, E., Vascular permeability and interstitial diffusion of macromolecules in the hamster cheek pouch: effects of vasoactive drugs. *Microvasc. Res.* **34**, 336-348 (1987).

Bekker, A.Y., Ritter, A.B., and Durán, W.N., Reduction of pressure in postcapillary venules induced by EPI-Fluorescent illumination of FITC-Dxtrans. *Microcirc. Endoth. Lymphatics.* **3**, 411-423 (1987).

Bekker, A.Y., Ritter, A.B., and Durán, W.N., Analysis of microvascular permeability to macromolecules by video-image digital processing. *Microvasc. Res.* **34**, 200-216 (1989).

Bird, R.B., Stewart, W.E., Lightfoot, E.N., "Transport Phenomena", John Wiley & Sons, New York (1960).

Carslaw, H.S., and Jaeger, J.C., "Conduction of Heat in Solids", 2nd Ed., Oxford University Press (Clarendon), London/New York (1959).

Carter, R.D., Joyner, W.L., and Renkin, E.M., Effects of histamine and some other substances on molecular selectivity of the capillary wall to plasma proteins and dextran. *Microvasc. Res.* **7**, 31-48 (1974).

Clough, G. and Michel, C.C., The ultrastructure of frog microvessels following perfusion with ionophore A23187. *Q. J. Exp. Physiol.* **73**, 123-125 (1988).

Crone, C., Levitt, D.G., The exchange of small solutes through the

capillary wall, in Renkin E.M., Michel C.C. (eds): Handbook of physiology, Sect 2, The cardiovascular system, Vol IV, The microcirculation. Bethesda, M.D., *Am. Physiol. Soc.*, 411-466 (1984).

Curry, F.E., Permeability coefficients of the capillary wall to low molecular weight hydrophilic solutes measured in single perfused capillaries of frog mesentery. *Microvasc. Res.* **240**. H597-605 (1979).

Curry, F.E., Antipyrine and aminopyrine permeability of individually perfused frog capillaries. *Am. J. Physiol.* **240**. H597-605 (1981).

Curry, F.E., Mechanics and thermodynamics of transcapillary exchange, in Renkin E.M., and Michel C.C.: Handbook of physiology, Sect. 2, The cardiovascular system, Vol IV, The microcirculation, Bethesda, M.D., *Am. Physiol. Soc.*, 309-374 (1984).

Curry, F.E. and Joyner, W.L., The effect of histamine, 48/80 and A23187 on albumin permeability in frog venular capillaries. *Federation Proce.* **45**, 1159 (1986).

Curry, F.E., Joyner, W.L., and Rutledge, J.C., Graded modulation of frog microvessel permeability to albumin using ionophore A23187. *Am. J. Physiol.* H (1989).

Curry, F.E., and Huxley, V.H., Comparison of the capillary membrane properties determining fluid exchange in single capillaries and whole organ. *Int. J. Microcir. Clin. Exp.* **1**. 381-391 (1982).

Curry, F.E., Mason, J.C., and Michel, C.C., Osmotic reflection coefficients of capillary walls to low molecular weight hydrophilic solutes measured in single perfused capillaries of frog mesentery. *J. Physiol. London.* **261**. 319-339 (1976).

Curry, F.E., and Michel, C.C., A fiber matrix theory of capillary permeability. *Microvasc. Res.* **20**. 96-99 (1980).

Dumrongsiri, S., Durán, W.N., and Ritter, A.B., Changes in macromolecular permselectivity of the epimyocardial microvascular barrier in STZ-treated rats. *FASEB J.* **4**, A1250 (1990).

Faxen, H., About T. Bohlin's paper: on the drag on rigid shpheres moving in a viscous liquid inside cylindrical tubes. *Kolloid Z.* **167**, 146 (1959).

Fox, J.R., and Wayland, H., Interstitial diffusion of macromolecules in the rat mesentery. *Microvasc. Res.* **18**, 255-276 (1979).

Garlick, D.G., and Renkin, E.M., Transport of large molecules from

plasma to interstitial fluid and lymph in dogs. *Am. J. Physiol.* **219**, H1596-H1605 (1970).

Gawlowski, D.M., and Durán, W.N., Dose-related effects of adenosine and bradykinin on microvascular permselectivity to macromolecules in the hamster cheek pouch. *Circ. Res.* **58**, 348-355 (1986).

Gerlowski, L.E., and Jain, R.K., Microvascular permeability of normal and neoplastic tissues. *Microvasc. Res.* **31**, 288-305 (1986).

Giddings, J.C., Kucera, E., Russell, C.P., and Myers, M.N., Statistical theory for the equilibrium distribution of rigid molecules in inert porous networks. *J. Phys. Chem.* **72**, 4397 (1968).

Haddy, F.J., Scott, J.B., and Grega, G.J., Effects of histamine on lymph protein concentration and flow in the dog forelimb. *Am. J. Physiol.* **223**, H1172-H1177 (1972).

Happel, J., and Brenner, H., "Low Reynolds Number Hydrodynamics", Prentice-Hall, New Jersey (1965).

Hermann, K., Platelet aggregation induced in the hamster cheek pouch by a photochemical process with excited fluorescein isothiocyanate dextran. *Microvasc. Res.* **26**, 238-249 (1983).

Hulström, D., and Svensjö, E., Intravital and electron-microscopy study of bradykinin induced vascular permeability changes using FITC-Dextrans as a tracer. *J. Pathol.* **129**, 125-132 (1979).

Huxley, V.H., Curry, F.E., and Adamson, R.H., Quantitative fluorescence microscopy on single capillaries. α-Lactalbimin transport. *Amer. J. Physiol.* **252**, H188-H197 (1987).

IMSL, "STAT/LIBRARY User's manual", IMSL Inc., Houston (1986).

Inoué, "Video microscopy", Plenum Press, New York and London (1986).

Joyner, W.L., Carter, R.D., Raizes, G.S., and Renkin, E.M., Influence of histamine and some other substances on blood-lymph transport of plasma protein and dextran in the dog paw. *Microvasc. Res.* **7**, 19-30 (1974).

Joyner, W.L., Svensjö, E., and Arfors, K.E., Simultaneous measurement of microvascular leakage and arteriolar blood flow as altered by PGE_1 and β_2-receptor stimulant in the hamster cheek pouch. *Microvasc. Res.* **18**, 301-310 (1979).

Kim, D., Armenante, P.M., and Durán, W.N., Mathematical modeling of mass transfer in microvascular wall and interstitial space. *Microvasc. Res.* **40**, 358-378 (1990).

Landis, E.M., Micro-injection studies of capillary permeability. *Am. J. Physiol.* **82**, 217-238 (1927).

Levenberg, K., A method for the solution of certain problems in least squares, *Quart. of Appl. Math.* **2**, 164-168 (1944).

Levick, J.R., and Michel, C.C., Permeability of individually perfused frog mesenteric capillaries to T-1924 and T-1824-albumin as evidence for a large pore system. *Q. J. Exp. Physiol.* **58**, 67-85 (1973).

Ley, K., and Arfors, K.E., Segmental differences of microvascular permeability for FITC-Dextrans in the hamster cheek pouch. *Microvasc. Res.* **31**, 84-99 (1986).

Majno, G., Shea, S.M., and Leventhal, M., Endothelial contraction induced by histamine-type mediators: An electron microscope study. *J. cell Biol.* **42**, 647-672 (1969).

Marquardt, D., An algorithm for least-squares estimation of nonlinear parameters, *SIAM J. of Appl. Math.* **11**, 431-441 (1963).

Mayhan, W.G., and Joyner, W.L., The effect of altering the external calcium concentration and calcium channel blocker, Verapamil, on microvascular leaky sites and Dextrans clearances in the hamster cheek pouch. *Microvasc. Res.* **28**, 143-158 (1984).

McMaster, P.D., and Parson, R.J., Physiological conditions existing in connective tissue. *J. Exp. Med.* **69**, 247-264 (1939).

McNamee, J.E., and Staub, N.C., Pore model of sheep lung microvascular barrier using new data on protein tracers. *Microvasc. Res.* **18**, 229-244 (1979).

Michel, C.C., The measurement of permeability in single capillaries. *Arch. Int. Physiol, Biochem.*, **86**, 657-667 (1978).

Michel, C.C., Filtration coefficients and osmotic reflection coefficients of the walls of single frog mesenteric capillaries. *J. Physiol. London.* **309**. 341-355 (1980).

Michel, C.C., Fluid movement through capillary walls, in Renkin E.M., and Michel C.C. (eds): Handbook of Physiology, Sect 2, The cardiovascular system, Vol IV, The microcirculation. Bethesda, M.D., *Am. Physiol. Soc.*, 375-409 (1984).

Michel, C.C., and Phillips, M.E., Effects of the divalent cation ionophore A23187 on the permeability of single frog mesenteric capillaries. *J. Physiol.* **353**, 111P (1984).

Nakamura, Y., and Wayland, H., Macromolecular transport in the cat mesentery. *Microvasc. Res.* **9**, 1-21 (1975).

Nugent L.J., Jain, R.K., Plasma pharmacokinetics and interstitial diffusion of macromolecules in a capillary bed. *Am. J. Physiol.*

246, H129-H137 (1974).

Ogston, A.G., Preston, B.M., Wells, J.D., On the transport of compact particles through solutions of chain polymers. *Proc. Roy. Soc. Lond. Ser. A.* **333**. 297-316 (1973).

Paaske, W.P., Microvascular exchange of albumin. *Microvasc. Res.* **25**, 101-107 (1982).

Paine, P.L., and Scherr, P., Drag coefficients for the movement of rigid spheres through liquid-filled cylindrical pores. *Biophys. J.* **15**, 1087-1089 (1975).

Pappenheimer, J.R., Passage of molecules through capillary walls. *Physiol. Rev.* **33**, 387-423 (1953)

Renkin, E.M., Watson, P.D., Sloop, C.H., Joyner, W.L., and Curry, F.E., Transport pathways for fluid and large molecules in microvascular endothelium of the dog's paw. *Microvasc. Res.* **14**, 205-214 (1977).

Ritter, A.B., Braun, W., Stein, A., and Durán, W.N., Visualization of the coronary microcirculation using digital image processing. *Comput. Biol. Med.* **15**, 361-374 (1985).

Rosenblum, W., Fluorescence induced in platelet aggregates as a guide to luminal contour in the pressure of platelet aggregation. *Microvasc. Res.* **15**, 103-106 (1978).

Sejrsen, P., Paaske, W.P., and Henriksen, O., Capillary permeability of I-albumin in skeletal muscle. *Microvasc. Res.* **29**, 265-381 (1985).

Svensjö, E., Arfors, K.E., Arturson, G., and Rutili, G., The hamster cheek pouch preparation as a model for studies of macromolecular permeability of the microvasculature. *Upsala. J. Med. Sci.* **83**, 71-79 (1978).

Taylor, A.E., and Granger, D.N., Exchange of macromolecules across the circulation, in Renkin E.M., Michel C.C. (eds):Handbook of Physiology, Sect 2, The cardiovascular system, Vol IV, The Microcirculation. Bethesda, M.D., *Am. Physiol. Soc.*, (1983).

Taylor, A.E., Granger, D.N., and Brace, R.A., Analysis of lymphatic protein flux data. I. Estimation of the reflection coefficient and permeability surface area product for total protein. *Microvasc. Res.*, **13**, 297-31 (1977).

Taylor, A.E., Perry, M.A., Shin, D.W., Granger, D.N., and Parker, J.C., Calculation of the effective pore radii in the dog hind paw capillaries using lymph endogenous proteins. *Microvasc. Res.* **23**, 276-290 (1982).

Wiederhielm, C.A., Transcapillary and interstitial transport phenomena

in the mesentery. *Federation Proc.* **25**, 1789-1798 (1966).

Wiederhielm, C.A., Shaw, M.L., Kehl, T.H., and Fox, J.R., A digital system for studying interstitial transport of dye molecules. *Microvasc. Res.* **5**, 243-250 (1973).

APPENDIX

APPENDIX A: Proof of the Real Nature of All Roots of Equation (3.25)

APPENDIX B: Analysis of the Roots of the Equation (3.25)

APPENDIX C: Computer Programs

APPENDIX D: Data for Digital Image Analysis and Calibration Experiments

APPENDIX A

Proof of the Real Nature of All Roots of Equation (3.25)

We will now show that equation (3.25) can only have real solutions for λ. This will be proven by showing that equation (3.25) cannot have any complex (or pure imaginary) and conjugate roots. Consider the functions $U_1(\lambda,z)$ and $U_2(\lambda,z)$ defined as

$$U_1(\lambda,z) = 2a \sinh q_1^{\circ}(\delta+z) \qquad \text{for } -\delta \le z < 0 \qquad (A.1)$$

$$U_2(\lambda,z) = 2 \sinh q_1^{\circ}\delta \; e^{-q_2^{\circ}z} \qquad \text{for } 0 \le z < +\infty \qquad (A.2)$$

where q_1° and q_2° are functions of λ (according to the definition given in Chapter 3), and where

$$U_1 = 0, \qquad \text{at} \quad z=-\delta$$

$$U_2 = 0, \qquad \text{at} \quad z=\infty$$

$$U_1 = aU_2, \qquad \text{at} \quad z=0$$

$$D_1\frac{dU_1}{dz} - \frac{1}{2}\chi_1 V_1 U_1 - b\{D_2\frac{dU_2}{dz} - \frac{1}{2}\chi_2 V_2 U_2\}$$

$$= a[2D_1 q_1^{\circ}\cosh q_1^{\circ}\delta + \{\frac{b}{a}(\chi_2 V_2 + 2q_2^{\circ}D_2) - \chi_1 V_1\} \sin(q_1^{\circ}\delta)] = 0, \qquad \text{at } z=0 \qquad (A.3)$$

In equation (A3) the term in square brackets is equal to zero only because λ is a root of equation (3.25). Then we have

$$\frac{d^2U_1}{dz^2} - (q_1^o)^2\, U_1 = 0 \qquad \text{for} \quad -\delta \le z < 0 \qquad (A.4)$$

$$\frac{d^2U_2}{dz^2} - (q_2^o)^2\, U_2 = 0 \qquad \text{for} \quad 0 \le z < +\infty \qquad (A.5)$$

Now let λ_1 and λ_2 be two different roots of equation (3.25), and let $U_1(\lambda_1)$, $U_2(\lambda_1)$, and $U_1(\lambda_2)$, $U_2(\lambda_2)$ be the functions U_1 and U_2 calculated at λ_1 and λ_2, respectively.

Following Carslaw and Jaeger's approach (1959) one can rearrange equations (A.4) and (A.5) to give

$$\frac{1}{D_1}(\lambda_2-\lambda_1)\int_{-\delta}^{0} U_1(\lambda_1)U_1(\lambda_2)\,dz + \int_{-\delta}^{0}[U_1''(\lambda_1)U_1(\lambda_2)-U_1''(\lambda_2)U_1(\lambda_1)]dz = 0$$

$$\frac{1}{D_2}(\lambda_2-\lambda_1)\int_{0}^{\infty} U_2(\lambda_1)U_2(\lambda_2)\,dz + \int_{0}^{\infty}[U_2''(\lambda_1)U_2(\lambda_2)-U_2''(\lambda_2)U_2(\lambda_1)]dz = 0$$

Therefore

$$(\lambda_2 - \lambda_1)\left[\int_{-\delta}^{0} U_1(\lambda_1)U_1(\lambda_2)\,dz + a\,b\int_{0}^{\infty} U_2(\lambda_1)U_2(\lambda_2)\,dz\right] =$$

$$= D_1\int_{-\delta}^{0}[U_1''(\lambda_2)U_1(\lambda_1)-U_1''(\lambda_1)U_1(\lambda_2)]dz +$$

$$a\,b\,D_2\int_{0}^{\infty}[U_2''(\lambda_2)U_2(\lambda_1)-U_2''(\lambda_1)U_2(\lambda_2)]\,dz =$$

$$= D_1\,[U_1(\lambda_1)U_1'(\lambda_2)-U_1(\lambda_2)U_1'(\lambda_1)]\Big|_{-\delta}^{0} +$$

$$a\ b\ D_2\ [U_2'(\lambda_2)U_2(\lambda_1)-U_2'(\lambda_1)U_2(\lambda_2)]\Big|_0^{\infty} = 0 \qquad (A.6)$$

using equation (A.3). It follows from equation (A.6) that the roots λ_1 and λ_2 cannot be complex or pure imaginary since $[U_1(\lambda_1),\ U_1(\lambda_2)]$ and $[U_2(\lambda_1),\ U_2(\lambda_2)]$ would be conjugate complex quantities and the term

$$\int_{-\delta}^{0} U_1(\lambda_1)U_1(\lambda_2)\ dz + ab \int_{0}^{\infty} U_2(\lambda_1)U_2(\lambda_2)\ dz$$

would be positive, thus making the term $[\lambda_2 - \lambda_1] = 0$. It is self evident that this condition cannot be verified if λ_1 and λ_2 are complex (or imaginary) and conjugate. Thus, all roots of equation (3.25) must be real and simple.

APPENDIX B

Determination of the Roots of the Equation (3.25)

In this Appendix, we will determine all the possible roots of equation (3.25). This equation can only have real and simple roots, as proven in Appendix A. Equation (3.25) can be rewritten as:

$$\tanh\,(q_1^{\circ}\delta) = \frac{2D_1\, q_1^{\circ}}{\chi_1 V_1 - \frac{b}{a}\,(\chi_2 V_2 + 2q_2^{\circ} D_2)}$$

where $(q_1^{\circ})^2 = \frac{\lambda}{D_1} + \frac{(\chi_1 V_1)^2}{4D_1{}^2} - \frac{(\chi_2 V_2)^2}{4D_1 D_2}$, and $(q_2^{\circ})^2 = \frac{\lambda}{D_2}$

Two cases will be considered, depending on the value of the difference $\{\frac{(\chi_1 V_1)^2}{4D_1} - \frac{(\chi_2 V_2)^2}{4D_2}\}$. Each case will be considered separately in one part. For each of these two parts four cases will be analyzed, depending on the sign of $(q_1^{\circ})^2$ and $(q_2^{\circ})^2$.

Part 1 Assumption: $\frac{(\chi_1 V_1)^2}{4D_1} > \frac{(\chi_2 V_2)^2}{4D_2}$

Case 1.1

Assumptions: $(q_1^{\circ})^2 > 0 \longrightarrow \lambda > \frac{(\chi_2 V_2)^2}{4D_2} - \frac{(\chi_1 V_1)^2}{4D_1}$

$(q_2^{\circ})^2 > 0 \longrightarrow \lambda > 0$

Since $\frac{(\chi_2 V_2)^2}{4D_2} - \frac{(\chi_1 V_1)^2}{4D_1}$ is a negative number, these two conditions can

be simultaneously satisfied only if $\lambda > 0$.

Then in equation (3.25) all the terms are real. Therefore equation (3.25) can only have one root (if any) in the range $\lambda > 0$ since the hyperbolic tangent is non-periodic.

Case 1.2

$$\text{Assumptions:} \quad (q_1^\circ)^2 < 0 \longrightarrow \lambda < \frac{(\chi_2 V_2)^2}{4D_2} - \frac{(\chi_1 V_1)^2}{4D_1}$$

$$(q_2^\circ)^2 > 0 \longrightarrow \lambda > 0$$

Since $\frac{(\chi_2 V_2)^2}{4D_2} - \frac{(\chi_1 V_1)^2}{4D_1}$ is a negative number, these two conditions can not be simultaneously satisfied. Hence, Case 1.2 is dismissed.

Case 1.3

$$\text{Assumptions:} \quad (q_1^\circ)^2 > 0 \longrightarrow \lambda > \frac{(\chi_2 V_2)^2}{4D_2} - \frac{(\chi_1 V_1)^2}{4D_1}$$

$$(q_2^\circ)^2 < 0 \longrightarrow \lambda < 0$$

Since $\frac{(\chi_2 V_2)^2}{4D_2} - \frac{(\chi_1 V_1)^2}{4D_1}$ is a negative number, these two conditions can be simultaneously satisfied only if $\frac{(\chi_2 V_2)^2}{4D_2} - \frac{(\chi_1 V_1)^2}{4D_1} < \lambda < 0$.

In equation (3.25), all the terms are real except q_2° in the denominator because of one of the assumptions for this case. Therefore, equation (3.25) can not have any real solutions. Hence, Case 1.3 is dismissed.

Case 1.4

Assumptions: $(q_1^\circ)^2 < 0 \longrightarrow \lambda < \frac{(\chi_2 V_2)^2}{4D_2} - \frac{(\chi_1 V_1)^2}{4D_1}$

$(q_2^\circ)^2 < 0 \longrightarrow \lambda < 0$

Since $\frac{(\chi_2 V_2)^2}{4D_2} - \frac{(\chi_1 V_1)^2}{4D_1}$ is a negative number, these two conditions can be simultaneously satisfied only if $\lambda < \frac{(\chi_2 V_2)^2}{4D_2} - \frac{(\chi_1 V_1)^2}{4D_1}$.

Since q_1° and q_2° are both imaginary we can define $q_1^\circ = \iota X$ and $q_2^\circ = \iota Y$. Then. equation (3.25) becomes

$$\tan(X\delta) = \frac{2D_1 X}{\chi_1 V_1 - \frac{b}{a}(\chi_2 V_2 + 2\,\iota Y D_2)}$$

Since the denominator in this equation is complex, equation (3.25) has no real solution. Hence, Case 1.4 is dismissed.

Part 2 Assumption: $\frac{(\chi_1 V_1)^2}{4D_1} < \frac{(\chi_2 V_2)^2}{4D_2}$

Case 2.1

Assumptions: $(q_1^\circ)^2 > 0 \longrightarrow \lambda > \frac{(\chi_2 V_2)^2}{4D_2} - \frac{(\chi_1 V_1)^2}{4D_1}$

$(q_2^\circ)^2 > 0 \longrightarrow \lambda > 0$

Since $\frac{(\chi_2 V_2)^2}{4D_2} - \frac{(\chi_1 V_1)^2}{4D_1}$ is a positive number, these two conditions can be simultaneously satisfied only if $\lambda > \frac{(\chi_2 V_2)^2}{4D_2} - \frac{(\chi_1 V_1)^2}{4D_1}$. Then in equation (3.25) all the terms are real numbers. Therefore, equation (3.25) can have one real solution (if any) in this range

since hyperbolic tangent is non-periodic.

Case 2.2

Assumptions: $(q_1^\circ)^2 < 0 \longrightarrow \lambda < \frac{(\chi_2 V_2)^2}{4D_2} - \frac{(\chi_1 V_1)^2}{4D_1}$

$(q_2^\circ)^2 > 0 \longrightarrow \lambda > 0$

Since $\frac{(\chi_2 V_2)^2}{4D_2} - \frac{(\chi_1 V_1)^2}{4D_1}$ is a positive number, these two conditions can be simultaneously satisfied only if $0 < \lambda < \frac{(\chi_2 V_2)^2}{4D_2} - \frac{(\chi_1 V_1)^2}{4D_1}$.

Since q_1° is imaginary we can define $q_1^\circ = \iota X$ where

$$X = \sqrt{-\frac{\lambda}{D_1} - \frac{(\chi_1 V_1)^2}{4D_1^2} + \frac{(\chi_2 V_2)^2}{4D_1 D_2}}$$

From $0 < \lambda < \frac{(\chi_2 V_2)^2}{4D_2} - \frac{(\chi_1 V_1)^2}{4D_1}$, it must be that

$$0 < X^2 < \frac{(\chi_2 V_2)^2}{4D_1 D_2} - \left(\frac{\chi_1 V_1}{2D_1}\right)^2$$

Since $\iota \tan a = \tanh(\iota a)$, then equation (3.25) can be rewritten as

$$\tan(X\delta) = \frac{2 D_1 X}{\chi_1 V_1 - \frac{b}{a}(\chi_2 V_2 + 2D_2 \Phi)}$$

where $\Phi = \sqrt{-\frac{D_1}{D_2} X^2 - \frac{(\chi_1 V_1)^2}{4D_1 D_2} + \left(\frac{\chi_2 V_2}{2D_2}\right)^2}$

This equation can only have a finite number of roots (if any) to be

found forvalues of X_n in the range $0 < X_n^2 < \frac{(\chi_2 V_2)^2}{4D_1D_2} - (\frac{\chi_1 V_1}{2D_1})^2$ with n=1,2,3,$\cdots$, m.

Case 2.3

Assumptions: $(q_1^\circ)^2 > 0 \longrightarrow \lambda > \frac{(\chi_2 V_2)^2}{4D_2} - \frac{(\chi_1 V_1)^2}{4D_1}$

$(q_2^\circ)^2 < 0 \longrightarrow \lambda < 0$

Since $\frac{(\chi_2 V_2)^2}{4D_2} - \frac{(\chi_1 V_1)^2}{4D_1}$ is a positive number, then these two conditions can not be simultaneously satisfied. Therefore Case 2.3 is dismissed.

Case 2.4

Assumptions: $(q_1^\circ)^2 < 0 \longrightarrow \lambda < \frac{(\chi_2 V_2)^2}{4D_2} - \frac{(\chi_1 V_1)^2}{4D_1}$

$(q_2^\circ)^2 < 0 \longrightarrow \lambda < 0$

Since $\frac{(\chi_2 V_2)^2}{4D_2} - \frac{(\chi_1 V_1)^2}{4D_1}$ is a positive number, then these two conditions can be simultaneously satisfied only if $\lambda < 0$.

Since q_1° and q_2° are both imaginary we can define $q_1^\circ = \iota X$ and $q_2^\circ = \iota Y$. From equation (3.25)

$$\tan(X\delta) = \frac{2D_1 X}{\chi_1 V_1 - \frac{b}{a}(\chi_2 V_2 + 2\,\iota Y D_2)}$$

Since the denominator is complex, equation (3.25) has no real solution. Hence, Case 2.4 is dismissed.

APPENDIX C

C.1. Computer program for numerically solving the partial differential equations

C.2. Non-linear regression computer program to search for the transport parameters using the proposed model

C.3. Computer program for the calculation of interstitial concentrations at various times

C.4. Computer program for the calculation of the cumulative mass extravasated in a given period of time

C.5. Computer program for the calculation of the mass flux at various time

C.6. Computer program for the calculation of the permeability coefficient in the microvascular wall

```
C
C ************************************************************************
C *  This is the program to solve a system of partial differential     *
C *  equations of the form UT = F(X, T, U, UX, UXX) using the          *
C *  method of lines with cubic Hermite polynomials.                   *
C *  In the program we used a subprogram called MOLCH in IMSL.         *
C ************************************************************************
C
C  Usage:  Call MOLCH (IOD, FCNUT, FCNBC, NPDES, T, TEND, NX,
C                      XBREAK, TOL, HINIT, Y, LDY)
C
C  ------------------------------------------------------------------
C  Arguments
C  ------------------------------------------------------------------
C
C   IOD:    Flag indicating the state of the computation
C   FCNUT:  User-supplied subroutine to evaluate the function
C           The usage is
C           Call FCNUT (NPDES, X, T, U, UX, UXX, UT), where
C           NPDES - Number of equations
C           X     - Space variable
C           U     - Array of length NPDES containing the dependent
C                   variable values
C           UX    - Array of length NPDES containing the derivative
C                   of U with respect to X
C           UXX   - Array of length NPDES containing the second
C                   derivative of U with respect to X
C           UT    - Array of length NPDES containing the derivative
C                   of U with respect to T
C           FCNUT must be declared EXTERNAL in the calling program.
C   FCNBC:  User-supplied subroutine to evaluate the boundary
C           conditions. The boundary conditions are
C           ALPHA(i)*U(i) + BETA(i)*UX(i) = GAMMA(i)
C           The usage is
C           Call FCNBC (NPDES, X, T, ALPHA, BETA, GAMMAP), where
C           NPDES - Number of equations
C           X     - Space variable
C           T     - Time variable
C           ALPHA - Array of length NPDES containing the ALPHA values
C           BETA  - Array of length NPDES containing the BETA values
C           GAMP  - Array of length NPDES containing the values of
C                   the derivative of GAMMA(i) with respect to T
C           FCNBC must be declared EXTERNAL in the calling program.
C   NPDES:  Number of differential equations
C   T:      Independent variable
C           On input, T supplies the initial time. On output,
C           T is set to the value to which the integration has
C           been completed.
C   TEND:   Value of T at which the solution is desired.
C   NX:     Number of mesh points
C   XBREAK: Array of length NX containing the break points for the
C           cubic Hermite splines used in the spatial discretization
C   TOL:    Differential equation error tolerance
C   Y:      Array of size NPDES by NX containing the solution
C   LDY:    Leading dimension of Y exactly as specified in the
C           dimension statement of the calling program
C
C  ************************************************************************
C
C
      PARAMETER  (NPDES=2, NX=12, LDY=NPDES)
      REAL       FCNBC, FCNUT, XBREAK(NX),Y(LDY,NX), FLOAT
      INTRINSIC  FLOAT
      EXTERNAL   FCNBC, FCNUT, MOLCH, UMACH, WRRRN
      COMMON     D1,D2,V1,V2,A,DELTA
      COMMON     DUMMY1, DUMMY2, DUMMY3
```

```
C
C   To increase a workspace
C
      COMMON/WORKSP/ RWKSP
      REAL RWKSP(40820)
      CALL IWKIN(40820)
C
C   Set parameters for the partial differential equation
C
      DATA  D1,D2,V1,V2/1.E-9,1.E-7,1.E-9,1.E-9/
      DATA  A,DELTA/1.,1.E-4/
C
C   Set breakpoints and initial conditions
C
      DO 10 I=1, NX
         XBREAK(I) = FLOAT(I)-2.
         Y(1,I)    = 1.E-20
         Y(2,I)    = 1.E-20
10    CONTINUE
C
C   Set parameters for subprogram of MOLCH
C
      TOL   =  1.E-4
      HINIT =  0.01
      T     =  0.0
      IDO   =  1
      CALL UMACH (2, NOUT)
C
      TEND=1000.
C
C   Solve the problem
C
      CALL MOLCH (IDO, FCNUT, FCNBC, NPDES, T, TEND, NX, XBREAK,
     &            TOL, HINIT, Y, LDY)
C
      WRITE(*,*) ' Solution at T =', T,'sec'
      CALL WRRRN (TITLE, NPDES, NX, Y, LDY, 0)
      END
C
C   Subroutine to evaluate the function
C
      SUBROUTINE FCNUT (NPDES, X, T, U, UX, UXX, UT)
      REAL      U(2), UX(2), UXX(2), UT(2)
      COMMON    D1,D2,V1,V2,A,DELTA
      COMMON    DUMMY1, DUMMY2, DUMMY3
C
C   Define the PDE
C
      UT(1) = D1/DELTA**2*UXX(1) - 1./DELTA*V1*UX(1)
      UT(2) = D2/DELTA**2*UXX(2) - 1./DELTA*V2*UX(2)
      DUMMY1 = UT(1)
      DUMMY2 = UT(2)
      DUMMY3 = UX(1)
      RETURN
      END
C
C   Subroutine to evaluate the boundary conditions
C
      SUBROUTINE FCNBC (NPDES, X, T, ALPHA, BETA, GAMP)
      REAL      ALPHA(2), BETA(2), GAMP(2)
      COMMON    D1,D2,V1,V2,A,DELTA
      COMMON    DUMMY1, DUMMY2, DUMMY3
C
C   Define the boundary condition
C
      IF ((X/DELTA).LT.0.) THEN
```

```
      ALPHA(1) = 1.0
      BETA(1)  = 0.0
      GAMP(1)  = 0.0
ELSE IF ((X/DELTA).GE.0.AND.(X/DELTA).LT.1.) THEN
      ALPHA(1) = 1.0
      BETA(1) =  0.0
      GAMP(1)  = A*DUMMY2
      ALPHA(2) = -V2
      BETA(2)  = D2/DELTA
      GAMP(2)  = D1/DELTA*DUMMY3 - V1*DUMMY1
ELSE
      ALPHA(2) = 1.0
      BETA(2)  = 0.0
      GAMP(2)  = 0.0
ENDIF
RETURN
END
```

```
C
C ***************************************************************
C *  This program is for non-linear regression. We used RNLIN      *
C *  subroutine in IMSL which is based on the Levenberg-Marquardt  *
C *  optimization algorithm to search the transport paremeters.    *
C *  Also we used QDAG and QDAGI subroutine programs in IMSL to    *
C *  integrate functions.                                          *
C ***************************************************************
C
C  Usage:  Call RLIN (FUNC, NPARM, IDERIV, THETA, R, LDR, IRANK,
C                     DFE, SSE)
C          Call QDAG (F, A, B, ERRABS, ERRREL, IRULE, RESULT,
C                     ERREST)
C          Call QDAGI (F, BOUND, INTERV, ERRABS, ERRREL, RESULT,
C                      ERREST)
C  ------------------------------------------------------------
C  Arguments
C  ------------------------------------------------------------
C    FUNC: User-supplied SUBROUTINE to return the weight, frequency,
C          residual, and optionally the derivative of the residual
C          at the given parameter vector THETA for a given
C          observation.  The usage is
C          Call FUNC (NPARM, THETA, IOPT, IOBS, FRQ, WT, E, DE,
C                     IEND)
C          where,
C          NPARM:  Number of unknown parameters in the regression
C                  function
C          THETA:  Vector of length NPARM containing parameter
C                  values
C          IOPT:   Function/derivative evaluation option
C          IOBS:   Observation number
C                  The function is evaluated at the IOBS-th
C                  observation
C          FRQ:    Frequency for the observation
C          WT:     Weight for the observation
C          E:      Error(residual) for the IOBS-th observation
C          DE:     Vector of length NPARM containing the partial
C                  derivatives of the residual for the IOBS-th
C                  observation
C          IEND:   Completion indicator
C    FUNC must be declared EXTERNAL in the calling program
C      NPARM: Number of unknown parameters in the regression
C             function
C      IDERIV:Derivative option
C      THETA: Vector of length NPARM containing parameter values
C      R:     NPARM by NPARM UPPER triangular matrix containing the
C             R matrix from a QR decomposition of the Jacobian
C      LDR:   Leading dimension of R exactly as specified in the
C             dimension statement in the calling program
C      IRANK: Rank of R
C      DFE:   Degree of freedom for error
C      SSE:   Sums of squares for error
C  ------------------------------------------------------------
C
C      F:      User-supplied FUNCTION to be integrated.
C              The form is F(X), where
C              X:  Independent variable
C              F:  The function value
C              F must be declared EXTERNAL in the calling program
C      A:      Lower limit of integration
C      B:      Upper limit of integration
C      ERRABS: Absolute accuracy desired
C      ERRREL: Relative accuracy desired
C      IRULE:  Choice of quadrature rule
C      RESULT: Estimate of the integral from A to B of F
C      ERREST: Estimate of the absolute value of the error
```

```
C
C       BOUND:  Finite bound of the integration range
C       INTERV: Flag indicating integration interval
C
C  *********************************************************************
C
C
      PARAMETER  (NOBS=8, NPARM=3, LDR=NPARM)
C
      INTEGER    IPARAM(6), SCALE(2), RPARAM(7)
      REAL       THETA(NPARM), R(LDR,NPARM), XDATA(NOBS),
     &           YDATA(NOBS), RESULT1(NOBS), RESULT2(NOBS),
     &           ERREST1(NOBS), ERREST2(NOBS)
      COMMON     /XYDATA/ XDATA, YDATA
      COMMON     D1, D2, V1, MOBS
      EXTERNAL   EXAMPL, R2LIN, UMACH, WRRRN, F1, F2, QDAG, QDAGI
C
      DATA   THETA/1.E-7,1.E-8,7.E-9/
C
      CALL UMACH (2, NOUT)
C
      IDERIV = 0
C
C   To use nondefault convergence parameters
C
      CALL R8LIN (IPARAM, RPARAM)
      IPARAM(3)=1000
C
      CALL R2LIN (EXAMPL, NPARM, IDERIV, THETA, R, LDR, IRANK,
     &            DFE, SSE, IPARAM, RPARAM, SCALE, IWK, WK)
C
      WRITE(*,*) D1, D2, V1
      WRITE(*,*) SSE
      END
C
C
      SUBROUTINE EXAMPL (NPARM, THETA, IOPT, IOBS, FRQ, WT, E, DE,
     &                   IEND)
      REAL       THETA(NPARM), DE(1)
      EXTERNAL   F1, F2, QDAG, QDAGI, CONST
C
      PARAMETER  (NOBS=8)
C
      REAL       XDATA(NOBS), YDATA(NOBS), RESULT1(NOBS),
     &           RESULT2(NOBS), ERREST1(NOBS), ERREST2(NOBS)
      COMMON     /XYDATA/ XDATA, YDATA
      COMMON     D1, D2, V1, MOBS
C
      DATA Z0,Z/5.E-5,2.5e-4/
C
      MOBS=IOBS
C
      IF (MOBS .LE. NOBS) THEN
      WT  = 1.0E0
      FRQ = 1.0E0
      IEND = 0
      D1 = THETA(1)
      D2 = THETA(2)
      V1 = THETA(3)
C
      IF (D1.LT.1.e-14.or.D1.GT.1.e-10) go to 10
      IF (D2.LT.1.e-10.or.D2.GT.1.e-6) go to 20
      IF (V1.LT.1.e-12.or.V1.GT.1.e-7) go to 30
C
      B1=V1*Z0/(2*D1)
      B2=Z/Z0
```

```
      B9=V1*Z/(2*D2)
      B3=1./0.65
      B12=SQRT(-(V1**2/(4*D1*D2))+(V1/(2*D1))**2)*Z0
C
      A1=EXP(B1+B9)
      A2=EXP(-B9)/(COSH(B1)-(1-2*B3)*SINH(B1))
C
      A=0.0
      B=B12
C
      ERRABS=0.0
      ERRREL=0.5
C
      IRULE=2
      CALL QDAG (F1, A, B, ERRABS,E RRREL, IRULE, RESULT1(MOBS),
     &           ERREST1(MOBS))
C
      BOUND=B
      INTERV=1
      CALL QDAGI (F2, BOUND, INTERV, ERRABS, ERRREL, RESULT2(MOBS),
     &            ERREST2(MOBS))
C
C
      PI=CONST('PI')
      E = YDATA(MOBS)-2./0.65*A1*(A2-4/PI*(RESULT1(MOBS)+
     &    RESULT2(MOBS)))
      ELSE
      IEND=1
      END IF
   10 DUM1=D1
   20 DUM2=D2
   30 DUM3=V1
      RETURN
      END
C
C
      REAL FUNCTION F1(U)
      REAL       U
      PARAMETER  (NOBS=8)
      REAL       XDATA(NOBS), YDATA(NOBS)
      COMMON     /XYDATA/ XDATA, YDATA
      COMMON     D1, D2, V1, MOBS
      DATA  Z0,Z/5.E-5,2.5E-4/
C
      T2=XDATA(MOBS)*D2/(Z0**2)
      B1=V1*Z0/(2*D1)
      B2=Z/Z0
      B3=1./0.65
      B5=(D1/D2)*(U**2)+(V1*Z0/(2*D2))**2
      B6=U**2/(U**2+((V1*Z0)**2/(4*D1*D2)))
      B7=1./0.65*SQRT(D1/D2)*D1*D2/((V1*Z0)**2)
      B8=2./0.65*SQRT(D1/D2)*D2/V1*U/Z0
      B10=D1/(V1*U*Z0)
      B11=SQRT(-(U/Z0)**2+(V1/(2*D1))**2-V1**2/(4*D1*D2))*Z0
      B13=SQRT(D1/D2)
      F1=B6*EXP(-B5*T2)*(2*B7*B11*SINH(B11)*COS(B13*U*B2)+B10*B11*
     &   (B11/B1*COSH(B11)-(1-B3)*SINH(B11))*SIN(B13*U*B2))
     &   /((B11/B1*COSH(B11)-(1-B3)*SINH(B11))**2+(B8*SINH(B11))**2)
      RETURN
      END
C
C
      REAL FUNCTION F2(U)
      REAL       U
      INTEGER    NOBS
      PARAMETER  (NOBS=8)
```

```
      REAL        XDATA(NOBS), YDATA(NOBS)
      COMMON      /XYDATA/ XDATA, YDATA
      COMMON      D1, D2, V1, MOBS
      DATA   Z0,Z/5.E-5,2.5E-4/
C
      T2=XDATA(MOBS)*D2/(Z0**2)
      B1=V1*Z0/(2*D1)
      B2=Z/Z0
      B3=1./0.65
      B5=(D1/D2)*(U**2)+(V1*Z0/(2*D2))**2
      B6=U**2/(U**2+((V1*Z0)**2/(4*D1*D2)))
      B7=1./0.65*SQRT(D1/D2)*D1*D2/((V1*Z0)**2)
      B8=2./0.65*SQRT(D1/D2)*D2/V1*U/Z0
      B10=D1/(V1*U*Z0)
      B4=SQRT((U/Z0)**2-(V1/(2*D1))**2+V1**2/(4*D1*D2))*Z0
      B13=SQRT(D1/D2)
      F2=B6*EXP(-B5*T2)*(2*B7*B4*SIN(B4)*COS(B13*U*B2)+B10*B4*
     &     (B4/B1*COS(B4)-(1-B3)*SIN(B4))*SIN(B13*U*B2))
     &     /((B4/B1*COS(B4)-(1-B3)*SIN(B4))**2+(B8*SIN(B4))**2)
      RETURN
      END
C
C
      BLOCK DATA XY
      PARAMETER (NOBS=8)
      REAL       XDATA(NOBS), YDATA(NOBS)
      COMMON     /XYDATA/ XDATA, YDATA
      DATA YDATA/.009,.055,.078,.098,.119,.131,.135,.145/
      DATA XDATA/300.,425.,732.,905.,1215.,1543.,1817.,2111./
      END
```

```
C
C ************************************************************
C *  This program is for the calculation of the interstitial *
C *  concentrations at various times.                        *
C ************************************************************
C
C
      REAL       F1, F2, SQRT, PI, CONST, EXP
      EXTERNAL   F1, F2, QDAGI, QDAG, CONST
      COMMON     T, D1, D2, V1, V2
      COMMON     Z, Z0, C0, P
C
      DATA   D1,D2,V1,V2/0.9E-11,1.29E-8,1.72E-8,1.72E-8/
      DATA   Z,Z0,C0,P/2.5e-4, 5.E-5, 2.,0.65/
      open(5,file='[dkk0941.dat]1.dat',status='old')
C
      WRITE(*,*) '  TIME', '          RESULT'
      DO 20 I=1,16
      READ (5,10) T
 10   FORMAT (1X,F10.1)
      T1=T*D2/(Z0**2)
      B1=V1*Z0/(2*D1)
      B2=Z/Z0
      B9=V2*Z/(2*D2)
      B3=V2/(P*V1)
      B12=SQRT(-V2**2/(4*D1*D2)+(V1/(2*D1))**2)*Z0
C
      A1=EXP(B1+B9)
      A2=EXP(-B9)/(COSH(B1)+(2*B3-1)*SINH(B1))
C
C
      A=0.0
      B = B12
C
      ERRABS = 0.0
      ERRREL = 0.001
C
      IRULE=2
      CALL QDAG (F1, A, B, ERRABS, ERRREL, IRULE, RESULT1, ERREST1)
C
      BOUND=B
      INTERV=1
C
      CALL QDAGI (F2, BOUND, INTERV, ERRABS, ERRREL, RESULT2, ERREST2)
C
      PI=CONST('PI')
      RESULT=C0/P*A1*(A2-4/PI*(RESULT1+RESULT2))
      WRITE(*,*) T, RESULT
 20   CONTINUE
      END
C
      REAL FUNCTION F1(U)
      REAL       U
      COMMON     T, D1, D2, V1, V2
      COMMON     Z, Z0, C0, P
      T1=T*D2/(Z0**2)
      B1=V1*Z0/(2*D1)
      B2=Z/Z0
      B3=V2/(P*V1)
      B5=(D1/D2)*(U**2)+(V2*Z0/(2*D2))**2
      B6=U**2/(U**2+((V2*Z0)**2/(4*D1*D2)))
      B7=1./P*SQRT(D1/D2)*D1*D2/((V1*Z0)**2)
      B8=2./P*SQRT(D1/D2)*D2/V1*U/Z0
      B10=D1/(V1*U*Z0)
      B11=SQRT(-(U/Z0)**2+(V1/(2*D1))**2-V2**2/(4*D1*D2))*Z0
      B13=SQRT(D1/D2)
```

```
      F1=B6*EXP(-B5*T1)*(2*B7*B11*SINH(B11)*COS(B13*U*B2)+B10*B11*
     &    (B11/B1*COSH(B11)-(1-B3)*SINH(B11))*SIN(B13*U*B2))
     &    /((B11/B1*COSH(B11)-(1-B3)*SINH(B11))**2+(B8*SINH(B11))**2)
      RETURN
      END
C
      REAL FUNCTION F2(U)
      REAL       U
      COMMON  T, D1, D2, V1, V2
      COMMON  Z, Z0, C0, P
      T1=T*D2/(Z0**2)
      B1=V1*Z0/(2*D1)
      B2=Z/Z0
      B3=V2/(P*V1)
      B5=(D1/D2)*(U**2)+(V2*Z0/(2*D2))**2
      B6=U**2/(U**2+((V2*Z0)**2/(4*D1*D2)))
      B7=1./P*SQRT(D1/D2)*D1*D2/((V1*Z0)**2)
      B8=2./P*SQRT(D1/D2)*D2/V1*U/Z0
      B10=D1/(V1*U*Z0)
      B4=SQRT((U/Z0)**2-(V1/(2*D1))**2+V2**2/(4*D1*D2))*Z0
      B13=SQRT(D1/D2)
      F2=B6*EXP(-B5*T1)*(2*B7*B4*SIN(B4)*COS(B13*U*B2)+B10*B4*
     &    (B4/B1*COS(B4)-(1-B3)*SIN(B4))*SIN(B13*U*B2))
     &    /((B4/B1*COS(B4)-(1-B3)*SIN(B4))**2+(B8*SIN(B4))**2)
      RETURN
      END
```

```
C
C  ****************************************************************
C  *  This program is for the calculation of the cumulative amount *
C  *  of macromolecule which has extravasated into the interstitial*
C  *  space in a given period of time.  We used QDAG and TWODQ     *
C  *  programs in IMSL to integrate the functions.                 *
C  ****************************************************************
C
C   Usage:  CALL QDAG (F, A, B, ERRABS, ERRREL, IRULE, RESULT,
C                      ERREST)
C
C    Purpose:  Integrate a function using a globally adaptive
C              scheme based on Gauss-Kronrod rules
C
C    Arguments
C
C     F:  User-supplied FUNCTION to be integrated.  The form is
C         F(X), where
C         X:  Independent variable
C         F:  The function value
C         F must be declared EXTERNAL in the calling program
C     A:  Lower limit of integration
C     B:  Upper limit of integration
C     ERRABS:  Absolute accuracy desired
C     ERRREL:  Relative accuracy desired
C     IRULE:  Choice of quadrature rule
C     RESULT:  Estimate of the integral from A to B of F
C     ERREST:  Estimate of the absolute value of the error
C
C
C   Usage:  CALL TWODQ (F, A, B, G, H, ERRABS, ERRREL, IRULE, RESULT,
C                       ERREST)
C
C   Purpose:  compute a two-diemnsional integrated integral
C
C   Arguments
C
C    G: User-supplied FUNCTION to evaluate the lower limits of
C       the inner integral. The form is
C       G(X), where
C       X:  Only argument of G
C       G:  The function value
C       G must be declared EXTERNAL in the calling program.
C    H: User-supplied FUNCTION to evaluate the upper limits of
C       the inner integral. The form is
C       H(X), where
C       X:  Only argument of G
C       H:  The function value
C       H must be declared EXTERNAL in the calling program.
C  ---------------------------------------------------------------
C
      REAL       F1, F2, F3, MASS, PI, CONST, G1, G2, H1, H2
      EXTERNAL   F1,F2,F3,G1,G2,H1,H2,TWODQ, QDAG, CONST
      COMMON     D1,D2,V1,V2,C0,Z0,P
      COMMON     B
C
      DATA   D1,D2,V1,V2/1.83E-11,2.11E-8,13.5E-8,13.5E-8/
      DATA   S/3.78E-5/
      DATA   C0,Z0,P/2.,5.E-5,0.65/
      OPEN (5,FILE='[dkk0941.dat]1.DAT',STATUS='OLD')
C
      B100=V1*Z0/(2*D1)
      B12=SQRT(-V2**2/(4*D1*D2)+(V1/(2*D1))**2)*Z0
C
      WRITE(*,*) '  TIME','          MASS RATE'
C
```

```
      DO 20 I=1,10
      READ(5,10) T
10    FORMAT(1X,F10.1)
C
C   Set limits of integration
      A=0.0
      B =T
C
C   Set error tolerances
      ERRABS = 0.0
      ERRREL = 0.01
C
      IRULE1=2
      IRULE2=2
C
      CALL QDAG (F1, A, B, ERRABS, ERRREL, IRULE1, RESULT1, ERREST1)
      A1=0.0
      B1=B12
      CALL TWODQ (F2,A1,B1,G1,H1,ERRABS,ERRREL,IRULE1,RESULT2,ERREST2)
C
      A2=B1
      B2=1000000.
      CALL TWODQ (F3,A2,B2,G2,H2,ERRABS,ERRREL,IRULE2,RESULT3,ERREST3)
C
      PI=CONST('PI')
      MASS=S*C0/P*EXP(B100)*(RESULT1-4/PI*(RESULT2+RESULT3))
C
      WRITE(*,*) B, MASS
20    CONTINUE
      END
C
C
      REAL FUNCTION F1(T)
      REAL        T
      COMMON      D1,D2,V1,V2,C0,Z0,P
      COMMON      B
      B100=V1*Z0/(2*D1)
      B3=V2/(P*V1)
      F1=V2/(COSH(B100)-(1-2*B3)*SINH(B100))
      RETURN
      END
C
C
      REAL FUNCTION F2(U,T)
      REAL        U,T
      COMMON      D1,D2,V1,V2,C0,Z0,P
      COMMON      B
      T1=T*D2/(Z0**2)
      B100=V1*Z0/(2*D1)
      B3=V2/(P*V1)
      B5=(D1/D2)*(U**2)+(V2*Z0/(2*D2))**2
      B6=U**2/(U**2+((V2*Z0)**2/(4*D1*D2)))
      B7=SQRT(D1/D2)*D1/P*D2/((V1*Z0)**2)
      B8=SQRT(D1/D2)*2/P*D2/V1*U/Z0
      B10=D1/(V1*U*Z0)
      B11=SQRT(-(U/Z0)**2+(V1/(2*D1))**2-V2**2/(4*D1*D2))*Z0
      B13=SQRT(D1/D2)
      F2=B6*EXP(-B5*T1)*(V2*B7*B11*SINH(B11)-D2*B10*B11*U/Z0*B13*
     &     (B11/B100*COSH(B11)-(1-B3)*SINH(B11)))
     &     /((B11/B100*COSH(B11)-(1-B3)*SINH(B11))**2+(B8*SINH(B11))**2)
      RETURN
      END
C
C
      REAL FUNCTION F3(U,T)
      REAL        U,T
```

```
      COMMON     D1,D2,V1,V2,C0,Z0,P,Z
      COMMON     B
      T1=T*D2/(Z0**2)
      B100=V1*Z0/(2*D1)
      B3=V2/(V1*P)
      B5=(D1/D2)*(U**2)+(V2*Z0/(2*D2))**2
      B6=U**2/(U**2+((V2*Z0)**2/(4*D1*D2)))
      B7=SQRT(D1/D2)*D1/P*D2/((V1*Z0)**2)
      B8=SQRT(D1/D2)*2/P*D2/V1*U/Z0
      B10=D1/(V1*U*Z0)
      B4=SQRT((U/Z0)**2-(V1/(2*D1))**2+V2**2/(4*D1*D2))*Z0
      B13=SQRT(D1/D2)
      F3=B6*EXP(-B5*T1)*(V2*B7*B4*SIN(B4)-D2*B10*B4*U/Z0*B13*
     &     (B4/B100*COS(B4)-(1-B3)*SIN(B4)))
     &     /((B4/B100*COS(B4)-(1-B3)*SIN(B4))**2+(B8*SIN(B4))**2)
      RETURN
      END
C
C
      REAL  FUNCTION  G1(T)
      REAL  T
      G1=0.0
      RETURN
      END
C
      REAL  FUNCTION G2(T)
      REAL  T
      G2=0.0
      RETURN
      END
C
      REAL  FUNCTION H1(T)
      REAL  T
      COMMON     D1,D2,V1,V2,C0,Z0,P
      COMMON     B
      H1=B
      RETURN
      END
C
      REAL FUNCTION H2(T)
      REAL T
      COMMON     D1,D2,V1,V2,C0,Z0,P
      COMMON     B
      H2=B
      RETURN
      END
```

```
C
C  ***************************************************************
C  *  This program is for the calculation of the mass flux into  *
C  *  the interstitial space.  We used QDAG and QDAGI programs   *
C  *  in IMSL to integrate the functions.                        *
C  ***************************************************************
C
C
      REAL       F1, F2, PI, CONST
      EXTERNAL   F1, F2, QDAGI, QDAG, CONST
      COMMON     D1,D2,V1,V2,C0,Z0,P,T
C
      DATA   D1,D2,V1,V2/0.83E-11,1.08E-8,10.9E-8,10.9E-8/
      DATA   C0,Z0,P/2.,5.E-5,0.53/
      OPEN (5,FILE='[DKK0941.DAT]1.DAT',STATUS='OLD')
C
      WRITE(*,*) '  TIME', '           MASS RATE'

      DO 20 I=1,22
      READ (5,10) T
 10   FORMAT(1X,F10.1)
      B100=V1*Z0/(2*D1)
      B3=V2/(P*V1)
      B12=SQRT(-V2**2/(4*D1*D2)+(V1/(2*D1))**2)*Z0
C
C
      RESULT1=V2/(COSH(B100)+(2*B3-1)*SINH(B100))
C
C   Set limits of integration
      A=0.0
      B =B12
C
C   Set error tolerances
      ERRABS = 0.0
      ERRREL = 0.001
C
      IRULE=2
C
      CALL QDAG (F1, A, B, ERRABS, ERRREL, IRULE, RESULT2, ERREST1)
C
      BOUND=B
      INTERV=1
C
      CALL QDAGI(F2, BOUND, INTERV, ERRABS, ERRREL, RESULT3, ERREST2)
C
      PI=CONST('PI')
      RESULT=C0/P*EXP(B100)*(RESULT1-4/PI*(RESULT2+RESULT3))
C
      WRITE(*,*) T, RESULT
 20   CONTINUE
      END
C
C
C
      REAL FUNCTION F1(U)
      REAL       U
      COMMON     D1,D2,V1,V2,C0,Z0,P,T
      T1=T*D2/(Z0**2)
      B100=V1*Z0/(2*D1)
      B3=V2/(P*V1)
      B5=(D1/D2)*(U**2)+(V2*Z0/(2*D2))**2
      B6=U**2/(U**2+((V2*Z0)**2/(4*D1*D2)))
      B7=SQRT(D1/D2)*D1/P*D2/((V1*Z0)**2)
      B8=SQRT(D1/D2)*2/P*D2/V1*U/Z0
      B10=D1/(V1*U*Z0)
      B11=SQRT(-(U/Z0)**2+(V1/(2*D1))**2-V2**2/(4*D1*D2))*Z0
```

```
      B13=SQRT(D1/D2)
      F1=B6*EXP(-B5*T1)*(V2*B7*B11*SINH(B11)-D2*B10*B11*U/Z0*B13*
     &    (B11/B100*COSH(B11)-(1-B3)*SINH(B11)))
     &    /((B11/B100*COSH(B11)-(1-B3)*SINH(B11))**2+(B8*SINH(B11))**2)
      RETURN
      END
C
C
      REAL FUNCTION F2(U)
      REAL       U
      COMMON     D1,D2,V1,V2,C0,Z0,P,T
      T1=T*D2/(Z0**2)
      B100=V1*Z0/(2*D1)
      B3=V2/(V1*P)
      B5=(D1/D2)*(U**2)+(V2*Z0/(2*D2))**2
      B6=U**2/(U**2+((V2*Z0)**2/(4*D1*D2)))
      B7=SQRT(D1/D2)*D1/P*D2/((V1*Z0)**2)
      B8=SQRT(D1/D2)*2/P*D2/V1*U/Z0
      B10=D1/(V1*U*Z0)
      B4=SQRT((U/Z0)**2-(V1/(2*D1))**2+V2**2/(4*D1*D2))*Z0
      B13=SQRT(D1/D2)
      F2=B6*EXP(-B5*T1)*(V2*B7*B4*SIN(B4)-D2*B10*B4*U/Z0*B13*
     &    (B4/B100*COS(B4)-(1-B3)*SIN(B4)))
     &    /((B4/B100*COS(B4)-(1-B3)*SIN(B4))**2+(B8*SIN(B4))**2)
      RETURN
      END
```

```
C
C ************************************************************
C *  This program for the calculation of the permeability    *
C *  coefficient in the microvascular wall.                  *
C ************************************************************
C
C
      REAL       F1, F2, F3, F4, F5, F6, F7,F8,F9,F10,PI,CONST
      EXTERNAL   F1, F2, F3, F4, F5, F6, F7,F8,F9,F10,
     &           QDAGI,QDAG,CONST
      COMMON     Z,Z1,Z2,T,D1,D2,V1,V2,Z0,C0,P
C
      DATA   D1,D2,V1,V2/0.27E-11,0.55E-8,1.25E-8,1.25E-8/
      DATA   z,Z1,Z2,z0,c0,p/-5.E-5,0.,-2.5E-5,5.E-5,2.,0.53/
      open(5,file='[dkk0941.dat]1.dat', status='old')
C
      WRITE(*,*) '  TIME', '             RESULT'
      DO 20 i=1,10
      READ(5,10) t
10    FORMAT(1X,F10.1)
      T1=T*D2/(Z0**2)
      B1=V1*Z0/(2*D1)
      B2=Z/Z0
      B3=V2/(V1*P)
      B12=SQRT(-V2**2/(4*D1*D2)+(V1/(2*D1))**2)*Z0
C
C     FOR CALCULATION OF C1
C
      A1=EXP(B1*(B2+1))
      A2=(COSH(B1*B2)+(1-2*B3)*SINH(B1*B2))/(COSH(B1)-(1-2*B3)*SINH(B1))
      A3=(B1/Z0*SINH(B1*B2)-B1/Z0*(2*B3-1)*COSH(B1*B2))/
     &    (COSH(B1)+(2*B1-1)*SINH(B1))
C
C     FOR CALCULATION OF C2
C
      B9=V2*Z1/(2.*D2)
      A4=EXP(B1)
      A5=EXP(-B9)/(COSH(B1)+(2*B3-1)*SINH(B1))
C
      A=0.0
      B = B12
C
      ERRABS = 0.0
      ERRREL = 0.001
C
      IRULE=2
C
C     FOR THE CALCULATION OF DIFFUSION TERM
C
      CALL QDAG (F1, A, B, ERRABS, ERRREL, IRULE, RESULT1, ERREST1)
      CALL QDAG (F3, A, B, ERRABS, ERRREL, IRULE, RESULT3, REEEST3)
C
      BOUND=B
      INTERV=1
C
      CALL QDAGI (F2,BOUND,INTERV,ERRABS,ERRREL,RESULT2,ERREST2)
      CALL QDAGI (F4,BOUND,INTERV,ERRABS,ERRREL,RESULT4,ERREST4)
C
      PI=CONST('PI')
      RESULT7=-(B1/Z0*D1*C0*A1*(A2-8/PI*(RESULT1+RESULT2))+
     &        D1*C0*A1*(A3-8/PI*(RESULT3+RESULT4)))
C
C     FOR CALCULATION OF CONVECTION TERM
C
      CALL QDAG (F5, A, B, ERRABS, ERRREL, IRULE, RESULT5, ERREST5)
      CALL QDAGI (F6, BOUND, INTERV, ERRABS, ERRREL, RESULT6, ERREST6)
```

```
C
      RESULT8=V1*C0*A1*(A2-8/PI*(RESULT5+RESULT6))
C
C
C     FOR CALCULATION OF C1
C
C
      CALL QDAG (F7, A, B, ERRABS, ERRREL, IRULE, RESULT9, ERREST7)
      CALL QDAGI (F8, BOUND, INTERV, ERRABS, ERRREL, RESULT10, ERREST8)
C
      RESULT11=C0*A1*(A2-8/PI*(RESULT9+RESULT10))
C
C
C     FOR CALCULATION OF C2
C
C
      CALL QDAG (F9, A, B, ERRABS, ERRREL, IRULE, RESULT12, ERREST9)
      CALL QDAGI (F10, BOUND, INTERV, ERRABS, ERRREL, RESULT13, ERREST10)
C
      RESULT14=C0/P*A4*(A5-4./PI*(RESULT12+RESULT13))
C
C
      RESULT = (RESULT7+RESULT8)/(RESULT11-RESULT14)
      WRITE(*,*) T, RESULT
20    CONTINUE
      END
C
C
C     FOR THE CALCULATION OF DIFFUSION TERM
C
      REAL FUNCTION F1(U)
      REAL       U
      COMMON     Z,Z1,Z2,T,D1,D2,V1,V2,Z0,C0,P
      T1=T*D2/(Z0**2)
      B1=V1*Z0/(2*D1)
      B2=Z2/Z0
      B3=V2/(V1*P)
      B5=(D1/D2)*(U**2)+(V2*Z0/(2*D2))**2
      B6=U**2/(U**2+((V2*Z0)**2/(4*D1*D2)))
      B7=SQRT(D1/D2)*D1/P*D2/((V1*Z0)**2)
      B8=SQRT(D1/D2)*2./P*D2/V1*U/Z0
      B11=SQRT(-(U/Z0)**2+(V1/(2*D1))**2-V2**2/(4*D1*D2))*Z0
      F1=B11*B7*B6*SINH(B11*(B2+1))*EXP(-B5*T1)/((B11/B1*COSH(B11)
     &    -(1-B3)*SINH(B11))**2+(B8*SINH(B11))**2)
      RETURN
      END
C
      REAL FUNCTION F2(U)
      REAL       U
      COMMON     Z,Z1,Z2,T,D1,D2,V1,V2,Z0,C0,P
      T1=T*D2/(Z0**2)
      B1=V1*Z0/(2*D1)
      B2=Z2/Z0
      B3=V2/(V1*P)
      B5=(D1/D2)*(U**2)+(V2*Z0/(2*D2))**2
      B6=U**2/(U**2+((V2*Z0)**2/(4*D1*D2)))
      B7=SQRT(D1/D2)*D1/P*D2/((V1*Z0)**2)
      B8=SQRT(D1/D2)*2./P*D2/V1*U/Z0
      B4=SQRT((U/Z0)**2-(V1/(2*D1))**2+V2**2/(4*D1*D2))*Z0
      F2=B4*B7*B6*SIN(B4*(B2+1))*EXP(-B5*T1)/((B4/B1*COS(B4)
     &    -(1-B3)*SIN(B4))**2+(B8*SIN(B4))**2)
      RETURN
      END
C
      REAL FUNCTION F3(U)
      REAL       U
```

```
      COMMON     Z,Z1,Z2,T,D1,D2,V1,V2,Z0,C0,P
      T1=T*D2/(Z0**2)
      B1=V1*Z0/(2*D1)
      B2=Z2/Z0
      B3=V2/(V1*P)
      B5=(D1/D2)*(U**2)+(V2*Z0/(2*D2))**2
      B6=U**2/(U**2+((V2*Z0)**2/(4*D1*D2)))
      B7=SQRT(D1/D2)*D1/P*D2/((V1*Z0)**2)
      B8=SQRT(D1/D2)*2/P*D2/V1*U/Z0
      B11=SQRT(-(U/Z0)**2+(V1/(2*D1))**2-V2**2/(4*D1*D2))*Z0
      F3=EXP(-B5*T1)*B6*B7*B11*B11/Z0*COSH(B11*(B2+1))/((B11/B1*
     &    COSH(B11)-(1-B3)*SINH(B11))**2+(B8*SINH(B11))**2)
      RETURN
      END
C
      REAL FUNCTION F4(U)
      REAL U
      COMMON     Z,Z1,Z2,T,D1,D2,V1,V2,Z0,C0,P
      T1=T*D2/(Z0**2)
      B1=V1*Z0/(2*D1)
      B2=Z2/Z0
      B3=V2/(V1*P)
      B5=(D1/D2)*(U**2)+(V2*Z0/(2*D2))**2
      B6=U**2/(U**2+((V2*Z0)**2/(4*D1*D2)))
      B7=SQRT(D1/D2)*D1/P*D2/((V1*Z0)**2)
      B8=SQRT(D1/D2)*2/P*D2/V1*U/Z0
      B4=SQRT((U/Z0)**2-(V1/(2*D1))**2+V2**2/(4*D1*D2))*Z0
      F4=EXP(-B5*T1)*B6*B7*B4*B4/Z0*COS(B4*(B2+1))/((B4/B1*COS(B4)
     &    -(1-B3)*SIN(B4))**2+(B8*SIN(B4))**2)
      RETURN
      END
C
C     FOR THE CALCULATION OF CONVECTION TERM
C
      REAL FUNCTION F5(U)
      REAL       U
      COMMON     Z,Z1,Z2,T,D1,D2,V1,V2,Z0,C0,P
      T1=T*D2/(Z0**2)
      B1=V1*Z0/(2*D1)
      B2=Z2/Z0
      B3=V2/(V1*P)
      B5=(D1/D2)*(U**2)+(V2*Z0/(2*D2))**2
      B6=U**2/(U**2+((V2*Z0)**2/(4*D1*D2)))
      B7=SQRT(D1/D2)*D1/P*D2/((V1*Z0)**2)
      B8=SQRT(D1/D2)*2/P*D2/V1*U/Z0
      B11=SQRT(-(U/Z0)**2+(V1/(2*D1))**2-V2**2/(4*D1*D2))*Z0
      F1=B11*B7*B6*SINH(B11*(B2+1))*EXP(-B5*T1)/((B11/B1*COSH(B11)
     &    -(1-B3)*SINH(B11))**2+(B8*SINH(B11))**2)
      RETURN
      END
C
      REAL FUNCTION F6(U)
      REAL       U
      COMMON     Z,Z1,Z2,T,D1,D2,V1,V2,Z0,C0,P
      T1=T*D2/(Z0**2)
      B1=V1*Z0/(2*D1)
      B2=Z2/Z0
      B3=V2/(V1*P)
      B5=(D1/D2)*(U**2)+(V2*Z0/(2*D2))**2
      B6=U**2/(U**2+((V2*Z0)**2/(4*D1*D2)))
      B7=SQRT(D1/D2)*D1/P*D2/((V1*Z0)**2)
      B8=SQRT(D1/D2)*2/P*D2/V1*U/Z0
      B4=SQRT((U/Z0)**2-(V1/(2*D1))**2+V2**2/(4*D1*D2))*Z0
      F2=B4*B7*B6*SIN(B4*(B2+1))*EXP(-B5*T1)/((B4/B1*COS(B4)
     &    -(1-B3)*SIN(B4))**2+(B8*SIN(B4))**2)
      RETURN
```

```
      END
C
C     FOR THE CALCULATION OF C1
C
      REAL FUNCTION F7(U)
      REAL        U
      COMMON      Z,Z1,Z2,T,D1,D2,V1,V2,Z0,C0,P
      T1=T*D2/(Z0**2)
      B1=V1*Z0/(2*D1)
      B2=Z/Z0
      B3=V2/(V1*P)
      B5=(D1/D2)*(U**2)+(V2*Z0/(2*D2))**2
      B6=U**2/(U**2+((V2*Z0)**2/(4*D1*D2)))
      B7=SQRT(D1/D2)*D1/P*D2/((V1*Z0)**2)
      B8=SQRT(D1/D2)*2/P*D2/V1*U/Z0
      B11=SQRT(-(U/Z0)**2+(V1/(2*D1))**2-V2**2/(4*D1*D2))*Z0
      F1=B11*B7*B6*SINH(B11*(B2+1))*EXP(-B5*T1)/((B11/B1*COSH(B11)
     &    -(1-B3)*SINH(B11))**2+(B8*SINH(B11))**2)
      RETURN
      END
C
C
      REAL FUNCTION F8(U)
      REAL        U
      COMMON      Z,Z1,Z2,T,D1,D2,V1,V2,Z0,C0,P
      T1=T*D2/(Z0**2)
      B1=V1*Z0/(2*D1)
      B2=Z/Z0
      B3=V2/(V1*P)
      B5=(D1/D2)*(U**2)+(V2*Z0/(2*D2))**2
      B6=U**2/(U**2+((V2*Z0)**2/(4*D1*D2)))
      B7=SQRT(D1/D2)*D1/P*D2/((V1*Z0)**2)
      B8=SQRT(D1/D2)*2/P*D2/V1*U/Z0
      B4=SQRT((U/Z0)**2-(V1/(2*D1))**2+V2**2/(4*D1*D2))*Z0
      F2=B4*B7*B6*SIN(B4*(B2+1))*EXP(-B5*T1)/((B4/B1*COS(B4)
     &    -(1-B3)*SIN(B4))**2+(B8*SIN(B4))**2)
      RETURN
      END
C
C     FOR THE CALCULATION OF C2
C
      REAL FUNCTION F9(U)
      REAL        U
      COMMON      Z,Z1,Z2,T,D1,D2,V1,V2,Z0,C0,P
      T1=T*D2/(Z0**2)
      B1=V1*Z0/(2*D1)
      B2=Z1/Z0
      B3=V2/(V1*P)
      B5=(D1/D2)*(U**2)+(V2*Z0/(2*D2))**2
      B6=U**2/(U**2+((V2*Z0)**2/(4*D1*D2)))
      B7=SQRT(D1/D2)*D1/P*D2/((V1*Z0)**2)
      B8=SQRT(D1/D2)*2./P*D2/V1*U/Z0
      B10=D1/(V1*U*Z0)
      B11=SQRT(-(U/Z0)**2+(V1/(2*D1))**2-V2**2/(4*D1*D2))*Z0
      B13=SQRT(D1/D2)
      F1=B6*EXP(-B5*T1)*(2*B7*B11*SINH(B11)*COS(B13*U*B2)+B10*B11*
     &     (B11/B1*COSH(B11)-(1-B3)*SINH(B11))*SIN(B13*U*B2))
     &     /((B11/B1*COSH(B11)-(1-B3)*SINH(B11))**2+(B8*SINH(B11))**2)
      RETURN
      END
C
C
      REAL FUNCTION F10(U)
      REAL        U
      COMMON      Z,Z1,Z2,T,D1,D2,V1,V2,Z0,C0,P
      T1=T*D2/(Z0**2)
```

```
      B1=V1*Z0/(2*D1)
      B2=Z1/Z0
      B3=V2/(V1*P)
      B5=(D1/D2)*(U**2)+(V2*Z0/(2*D2))**2
      B6=U**2/(U**2+((V2*Z0)**2/(4*D1*D2)))
      B7=SQRT(D1/D2)*D1/P*D2/((V1*Z0)**2)
      B8=SQRT(D1/D2)*2./P*D2/V1*U/Z0
      B10=D1/(V1*U*Z0)
      B13=SQRT(D1/D2)
      B4=SQRT((U/Z0)**2-(V1/(2*D1))**2+V2**2/(4*D1*D2))*Z0
      F2=B6*EXP(-B5*T1)*(2*B7*B4*SIN(B4)*COS(B13*U*B2)+B10*B4*
     &     (B4/B1*COS(B4)-(1-B3)*SIN(B4))*SIN(B13*U*B2))
     &     /((B4/B1*COS(B4)-(1-B3)*SIN(B4))**2+(B8*SIN(B4))**2)
      RETURN
      END
```

APPENDIX D

1. Results for Macromolecular Transport

Table D.1. Results for digital image analysis of the experimental data
Tracer: FITC-Dx 70

Time (sec)	IOI	IOI after background subtraction	Gray level after background subtraction	Concentration (mg/ml)
295	7183	1205	12.05	0.155
411	7624	1646	16.46	0.285
731	8109	2131	21.31	0.428
911	8682	2704	27.04	0.597
1119	8787	2809	28.09	0.628
1498	9177	3199	31.99	0.743
1815	9241	3263	32.63	0.762
2100	9353	3375	33.75	0.795
2409	9963	3985	39.85	0.975
2699	10031	4053	40.53	0.995
3001	10167	4189	41.89	1.035
3310	10194	4216	42.16	1.043
3630	10509	4531	45.31	1.136
3955	10529	4551	45.51	1.142
4235	10584	4606	46.06	1.158
4527	10690	4712	47.12	1.189

* Transport parameters determined after regression

$D_1 = 0.87 \times 10^{-11}$ (cm^2/sec), $D_2 = 1.27 \times 10^{-8}$ (cm^2/sec)

$V = 2.03 \times 10^{-8}$ (cm/sec)

Table D.2. Results for digital image analysis of the experimental data

Tracer: FITC-Dx 70

Time (sec)	IOI	IOI after background subtraction	Gray level after background subtraction	Concentration (mg/ml)
305	7173	1195	11.95	0.152
420	7712	1734	17.34	0.311
711	8156	2178	21.78	0.442
927	8668	2690	26.90	0.593
1197	8939	2961	29.61	0.673
1490	9028	3050	30.50	0.699
1832	9570	3592	35.92	0.859
2115	9662	3684	36.84	0.886
2407	9977	3999	39.99	0.979
2681	10299	4321	43.21	1.074
3025	10407	4429	44.29	1.106
3365	10512	4534	45.34	1.137
3624	10563	4585	45.85	1.152
3968	10651	4673	46.73	1.178
4255	10679	4701	47.01	1.186
4547	10712	4734	47.34	1.196

* Transport parameters determined after regression

$D_1 = 0.93 \times 10^{-11}$ (cm^2/sec), $D_2 = 1.32 \times 10^{-8}$ (cm^2/sec)

$V = 2.12 \times 10^{-8}$ (cm/sec)

Table D.3. Results for digital image analysis of the experimental data

Tracer: FITC-Dx 70

Time (sec)	IOI	IOI after background subtraction	Gray level after background subtraction	Concentration (mg/ml)
321	7248	1270	12.70	0.174
435	7828	1805	18.05	0.332
727	8390	2412	24.12	0.511
944	8668	2690	26.90	0.593
1215	8790	2812	28.12	0.629
1499	9262	3284	32.84	0.768
1827	9645	3667	36.67	0.881
2144	9706	3728	37.28	0.899
2409	9824	3846	38.46	0.934
2688	10316	4338	43.38	1.079
3015	10465	4487	44.87	1.123
3346	10550	4572	45.72	1.148
3614	10587	4609	46.09	1.159
3957	10665	4687	46.87	1.182
4232	10695	4717	47.17	1.191
4540	10723	4745	47.45	1.199

* Transport parameters determined after regression

$D_1 = 0.95 \times 10^{-11}$ (cm^2/sec), $D_2 = 1.35 \times 10^{-8}$ (cm^2/sec)

$V = 2.07 \times 10^{-8}$ (cm/sec)

Table D.4. Results for digital image analysis of the experimental data

Tracer: FITC-Dx 70

Time (sec)	IOI	IOI after background subtraction	Gray level after background subtraction	Concentration (mg/ml)
307	7228	1250	12.50	0.168
441	7814	1836	18.36	0.341
736	8350	2372	23.72	0.499
987	8668	2690	26.90	0.593
1238	8790	2812	28.12	0.629
1484	9126	3148	31.48	0.728
1865	9143	3165	31.65	0.733
2126	9397	3419	34.19	0.808
2424	9824	3846	38.46	0.934
2654	10079	4101	41.01	1.009
3046	10129	4151	41.51	1.024
3332	10211	4233	42.33	1.048
3627	10587	4609	46.09	1.159
3942	10665	4687	46.87	1.182
4229	10695	4717	47.17	1.191
4521	10723	4745	47.45	1.199

* Transport parameters determined after regression

$D_1 = 0.85 \times 10^{-11}$ (cm^2/sec), $D_2 = 1.23 \times 10^{-8}$ (cm^2/sec)

$V = 2.01 \times 10^{-8}$ (cm/sec)

Table D.5. Results for digital image analysis of the experimental data

Tracer: FITC-Dx 150

Time (sec)	IOI	IOI after background subtraction	Gray level after background subtraction	Concentration (mg/ml)
310	6855	877	8.77	0.058
611	7075	1097	10.97	0.123
924	7339	1361	13.61	0.201
1221	7526	1548	15.48	0.256
1455	7695	1717	17.17	0.306
1781	7929	1951	19.51	0.375
2002	8092	2114	21.14	0.423
2376	8146	2168	21.68	0.439
2786	8187	2209	22.09	0.451
3022	8258	2280	22.80	0.472
3286	8373	2395	23.95	0.506
3543	8465	2487	24.97	0.536
3902	8567	2589	25.89	0.563
4273	8587	2609	26.09	0.569
4423	8614	2636	26.36	0.577

* Transport parameters determined after regression

$D_1 = 0.25 \times 10^{-11}$ (cm^2/sec), $D_2 = 0.50 \times 10^{-8}$ (cm^2/sec)

$V = 1.37 \times 10^{-8}$ (cm/sec)

Table D.6. Results for digital image analysis of the experimental data

Tracer: FITC-Dx 150

Time (sec)	IOI	IOI after background subtraction	Gray level after background subtraction	Concentration (mg/ml)
322	6875	897	8.97	0.064
631	7312	1334	13.34	0.193
916	7509	1531	15.31	0.251
1215	7570	1592	15.92	0.269
1464	7661	1683	16.83	0.296
1773	8007	2029	20.29	0.398
2097	8146	2168	21.68	0.439
2385	8153	2175	21.75	0.441
2712	8207	2229	22.29	0.457
3053	8282	2304	23.04	0.479
3242	8404	2426	24.26	0.515
3598	8512	2534	25.34	0.547
3911	8587	2609	26.09	0.569
4254	8617	2639	26.39	0.578
4411	8634	2656	26.56	0.583

* Transport parameters determined after regression

$D_1 = 0.26 \times 10^{-11}$ (cm^2/sec), $D_2 = 0.51 \times 10^{-8}$ (cm^2/sec)

$V = 1.41 \times 10^{-8}$ (cm/sec)

Table D.7. Results for digital image analysis of the experimental data

Tracer: FITC-Dx 150

Time (sec)	IOI	IOI after background subtraction	Gray level after background subtraction	Concentration (mg/ml)
331	6868	890	8.90	0.062
653	7244	1266	12.66	0.173
927	7407	1429	14.29	0.221
1205	7773	1795	17.95	0.329
1454	7899	1921	19.21	0.366
1771	7997	2019	20.19	0.395
2099	8126	2148	21.48	0.433
2375	8146	2168	21.68	0.439
2773	8390	2412	24.12	0.511
3064	8485	2507	25.07	0.539
3269	8543	2565	25.65	0.556
3559	8573	2595	25.95	0.565
3942	8600	2622	26.22	0.573
4279	8621	2643	26.43	0.579
4400	8628	2650	26.50	0.581

* Transport parameters determined after regression

$D_1 = 0.28 \times 10^{-11}$ (cm^2/sec), $D_2 = 0.61 \times 10^{-8}$ (cm^2/sec)

$V = 2.51 \times 10^{-8}$ (cm/sec)

Table D.8. Results for digital image analysis of the experimental data

Tracer: FITC-Dx 150

Time (sec)	IOI	IOI after background subtraction	Gray level after background subtraction	Concentration (mg/ml)
334	6960	982	9.82	0.089
659	7312	1334	13.34	0.193
936	7611	1633	16.33	0.281
1286	7702	1724	17.24	0.308
1474	7817	1839	18.39	0.342
1760	7912	1934	19.34	0.370
2082	8082	2104	21.04	0.420
2387	8177	2199	21.99	0.448
2792	8367	2389	23.89	0.504
3055	8448	2470	24.70	0.528
3296	8553	2575	25.75	0.559
3532	8563	2585	25.85	0.562
3932	8580	2602	26.02	0.567
4270	8634	2656	26.56	0.583
4427	8668	2690	26.90	0.593

* Transport parameters determined after regression

$D_1 = 0.30 \times 10^{-11}$ (cm^2/sec), $D_2 = 0.65 \times 10^{-8}$ (cm^2/sec)

$V = 1.81 \times 10^{-8}$ (cm/sec)

Table D.9. Results for digital image analysis of the experimental data

Tracer: FITC-Dx 70 with calcium ionophore A23187

Time (sec)	IOI	IOI after background subtraction	Gray level after background subtraction	Concentration (mg/ml)
180	7587	1609	16.09	0.274
364	8363	2385	23.85	0.503
521	8960	2982	29.82	0.679
741	9889	3911	39.11	0.953
899	10350	4372	43.72	1.089
1087	10533	4555	45.55	1.143
1262	10723	4745	47.45	1.199
1421	10848	4870	48.70	1.236
1621	11123	5145	51.45	1.317
1757	11482	5504	55.04	1.423
1994	11604	5626	56.26	1.459
2160	11970	5992	59.92	1.567
2351	12119	6141	61.41	1.611
2546	12190	6212	62.12	1.632

* Transport parameters determined after regression

$D_1 = 1.80 \times 10^{-11}$ (cm^2/sec), $D_2 = 2.07 \times 10^{-8}$ (cm^2/sec)

$V = 15.1 \times 10^{-8}$ (cm/sec)

Table D.10. Results for digital image analysis of the experimental data

Tracer: FITC-Dx 70 with calcium ionophore A23187

Time (sec)	IOI	IOI after background subtraction	Gray level after background subtraction	Concentration (mg/ml)
188	7672	1694	16.94	0.299
343	8580	2602	26.02	0.567
518	9407	3429	34.29	0.811
732	9756	3778	37.78	0.914
891	9821	3843	38.43	0.933
1077	10458	4480	44.80	1.121
1244	10651	4673	46.73	1.178
1462	10902	4924	49.24	1.252
1642	11153	5175	51.75	1.326
1774	11560	5582	55.82	1.446
1965	11797	5819	58.19	1.516
2143	11977	5999	59.99	1.569
2364	12153	6175	61.75	1.621
2529	12214	6236	62.36	1.639

* Transport parameters determined after regression

$D_1 = 1.81 \times 10^{-11}$ (cm^2/sec), $D_2 = 2.08 \times 10^{-8}$ (cm^2/sec)

$V = 15.2 \times 10^{-8}$ (cm/sec)

Table D.11. Results for digital image analysis of the experimental data

Tracer: FITC-Dx 70 with calcium ionophore A23187

Time (sec)	IOI	IOI after background subtraction	Gray level after background subtraction	Concentration (mg/ml)
174	7594	1616	16.16	0.276
351	8672	2694	26.94	0.594
525	9062	3084	30.84	0.709
719	9523	3545	35.45	0.845
876	10045	4067	40.67	0.999
1089	10534	4556	45.56	1.173
1236	10845	4867	48.67	1.235
1451	10940	4962	49.62	1.263
1622	11119	5141	51.41	1.316
1764	11668	5690	56.90	1.478
1983	11862	5884	58.84	1.535
2198	12041	6063	60.63	1.588
2313	12119	6141	61.41	1.611
2542	12180	6202	62.02	1.629

* Transport parameters determined after regression

$D_1 = 1.79 \times 10^{-11}$ (cm^2/sec), $D_2 = 2.05 \times 10^{-8}$ (cm^2/sec)

$V = 15.9 \times 10^{-8}$ (cm/sec)

Table D.12. Results for digital image analysis of the experimental data

Tracer: FITC-Dx 70 with calcium ionophore A23187

Time (sec)	IOI	IOI after background subtraction	Gray level after background subtraction	Concentration (mg/ml)
195	7597	1619	16.19	0.277
324	8689	2711	27.11	0.599
598	9068	3090	30.90	0.711
728	9536	3558	35.58	0.849
885	10004	4026	40.26	0.987
1111	10699	4721	47.21	1.192
1286	10865	4887	48.87	1.241
1497	10970	4992	49.92	1.272
1663	11136	5158	51.58	1.321
1772	11672	5694	56.94	1.479
1964	11889	5911	59.11	1.543
2127	12045	6067	60.67	1.589
2364	12146	6168	61.68	1.619
2521	12187	6209	62.09	1.631

* Transport parameters determined after regression

$D_1 = 1.90 \times 10^{-11}$ (cm^2/sec), $D_2 = 2.23 \times 10^{-8}$ (cm^2/sec)

$V = 16.4 \times 10^{-8}$ (cm/sec)

Table D.13. Results for digital image analysis of the experimental data

Tracer: FITC-Dx 150 with calcium ionophore A23187

Time (sec)	IOI	IOI after background subtraction	Gray level after background subtraction	Concentration (mg/ml)
199	7261	1283	12.83	0.178
352	8011	2033	20.33	0.399
531	8587	2609	26.09	0.569
720	8723	2745	27.45	0.609
917	8889	2911	29.11	0.658
1121	9360	3382	33.82	0.797
1298	9801	3823	38.23	0.927
1435	9940	3962	39.62	0.968
1629	10011	4033	40.33	0.989
1807	10245	4267	42.67	1.058
1989	10550	4572	45.72	1.148
2157	10567	4589	45.89	1.153
2340	10679	4701	47.01	1.186
2632	10821	4843	48.43	1.228
2704	10848	4870	48.70	1.236

* Transport parameters determined after regression

$D_1 = 0.88 \times 10^{-11}$ (cm^2/sec), $D_2 = 1.22 \times 10^{-8}$ (cm^2/sec)

$V = 16.0 \times 10^{-8}$ (cm/sec)

Table D.14. Results for digital image analysis of the experimental data

Tracer: FITC-Dx 150 with calcium ionophore A23187

Time (sec)	IOI	IOI after background subtraction	Gray level after background subtraction	Concentration (mg/ml)
179	7292	1314	13.14	0.187
364	7936	1958	19.58	0.377
529	8594	2616	26.16	0.571
729	8733	2755	27.55	0.612
926	9000	3022	30.22	0.691
1128	9360	3514	35.14	0.836
1277	9746	3768	37.68	0.911
1464	9953	3975	39.75	0.972
1638	10014	4036	40.36	0.990
1832	10360	4382	43.82	1.092
1997	10631	4653	46.53	1.172
2164	10702	4724	47.24	1.193
2321	10729	4751	47.51	1.201
2644	10801	4823	48.23	1.222
2719	10831	4853	48.53	1.231

* Transport parameters determined after regression

$D_1 = 0.89 \times 10^{-11}$ (cm^2/sec), $D_2 = 1.24 \times 10^{-8}$ (cm^2/sec)

$V = 16.0 \times 10^{-8}$ (cm/sec)

Table D.15. Results for digital image analysis of the experimental data

Tracer: FITC-Dx 150 with calcium ionophore A23187

Time (sec)	IOI	IOI after background subtraction	Gray level after background subtraction	Concentration (mg/ml)
193	7333	1355	13.55	0.199
384	8258	2280	22.80	0.472
595	8621	2643	26.43	0.579
739	8756	2778	27.78	0.619
947	8973	2995	29.95	0.683
1187	9512	3534	35.34	0.842
1246	9617	3639	36.39	0.873
1432	9699	3721	37.21	0.897
1664	9817	3839	38.39	0.932
1886	10153	4175	41.75	1.031
1982	10329	4351	43.51	1.083
2196	10567	4589	45.89	1.153
2372	10723	4745	47.45	1.199
2665	10794	4816	48.16	1.220
2710	10828	4850	48.50	1.230

* Transport parameters determined after regression

$D_1 = 0.79 \times 10^{-11}$ (cm^2/sec), $D_2 = 0.98 \times 10^{-8}$ (cm^2/sec)

$V = 13.8 \times 10^{-8}$ (cm/sec)

Table D.16. Results for digital image analysis of the experimental data

Tracer: FITC-Dx 150 with calcium ionophore A23187

Time (sec)	IOI	IOI after background subtraction	Gray level after background subtraction	Concentration (mg/ml)
208	7407	1429	14.29	0.221
397	8221	2243	22.43	0.461
547	8550	2572	25.72	0.558
739	8617	2639	26.39	0.578
927	8960	2982	29.82	0.679
1084	9478	3500	35.00	0.832
1259	9634	3656	36.56	0.878
1495	9706	3728	37.28	0.899
1662	9831	3853	38.53	0.936
1897	10119	4141	41.41	1.021
1942	10309	4331	43.31	1.077
2188	10597	4619	46.19	1.162
2346	10682	4704	47.04	1.187
2655	10787	4809	48.09	1.218
2731	10834	4856	48.56	1.232

* Transport parameters determined after regression

$D_1 = 0.75 \times 10^{-11}$ (cm^2/sec), $D_2 = 0.95 \times 10^{-8}$ (cm^2/sec)

$V = 14.2 \times 10^{-8}$ (cm/sec)

2. Results for the Calibration Curves

The microvascular calibration curves for FITC-Dx 70 and FITC-Dx 150 are shown in Figures D.1, D.2, D.3, and D.4 at various threshold values (KV). Each point in these figures represents the average of nine experimental determinations at that particular FITC-Dx concentration. For each of the points, the standard deviation was found to be in the range ±1.01 to ±3.43 gray level units. The average standard deviation was found to be ±1.16 gray level units. In general, a linear correlation was found between mean gray level and intravascular FITC-Dx concentration. A typical relationship between mean gray level and FITC-Dx 150 concentration obtained with the 10x objective is shown in Figure D.1. Figure D.2 shows the corresponding curves using the 32x objective. Figures D.3, and D.4 show the calibration curves for FITC-Dx 70 intravascular concentration with different objectives (10x or 32x).

The linear regression equation correlating TV fluorescence intensity (gray level) and *vascular* FITC-Dx 150 concentration (0.4 mg/ml - 3.0 mg/ml; 32x objective; gain = 4.0; KV = 5) was found to be

$$\text{Mean Gray Level} = 48.7\ [\text{Vascular Concentration (mg/ml)}] + 41.4$$

The correlation coefficient for this equation is 0.994. Under the same experimental recording conditions, the correlation coefficient for the linear regression equation applicable to the plasma concentration of FITC-Dx 70 is 0.818.

A linear correlation between gray level and FITC-Dx concentration

was also demonstrated in the interstitial space. The calibration curves for FITC-Dx 70 and 150 in the interstitial space are shown in Figures D.5, D.6, D.7, and D.8 using 10x and 32x objectives at various threshold values. The standard deviation for each point was found to be in the range ±1.11 to ±3.91 gray level units. The average standard deviation was found to be ±2.03 gray level units.

The corresponding regression equation correlating fluorescence intensity and *interstitial* FITC-Dx 150 concentration (0.12 mg/ml - 1.50 mg/ml; 32x objective; gain = 4; KV =6) was found to be

$$\text{Mean Gray Level} = 33.9\ [\text{Tissue Concentration (mg/ml)}] + 6.8$$

This equation has a correlation coefficient of 0.993. This equation was used to determine the interstitial space concentrations at various time in this investigation.

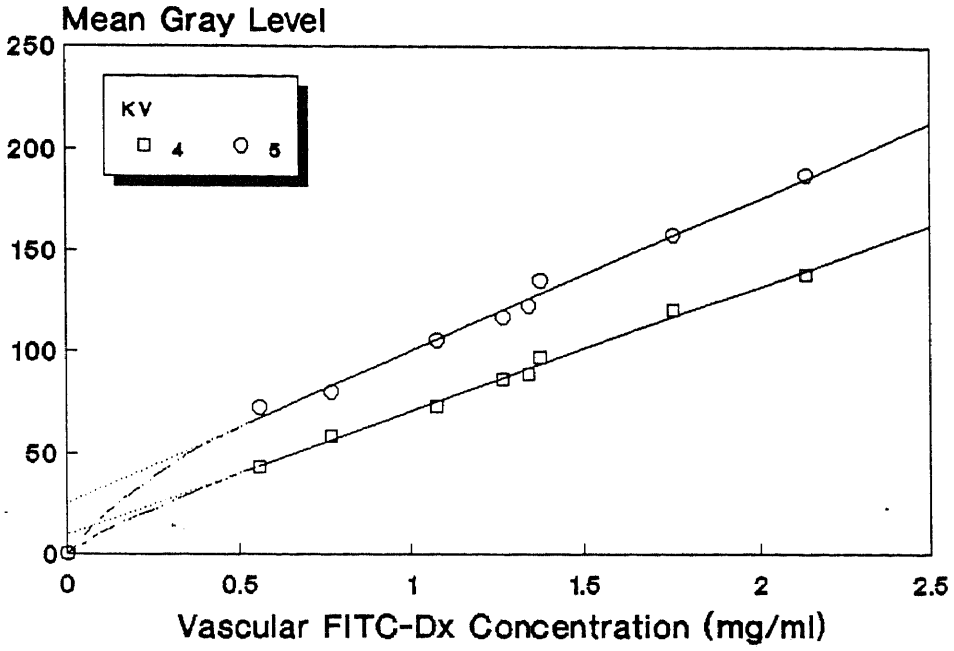

Figure D.1

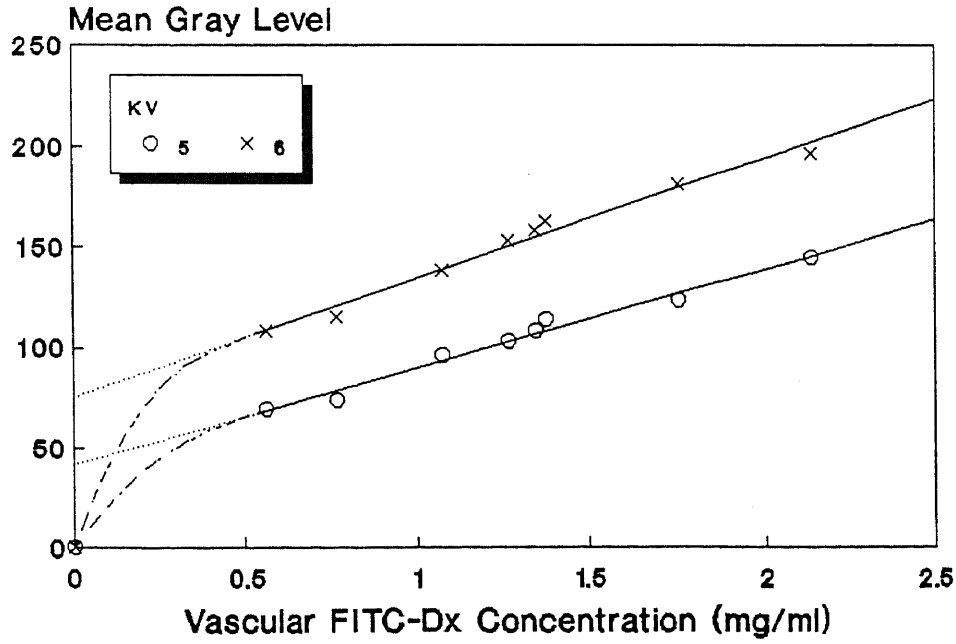

Figure D.2

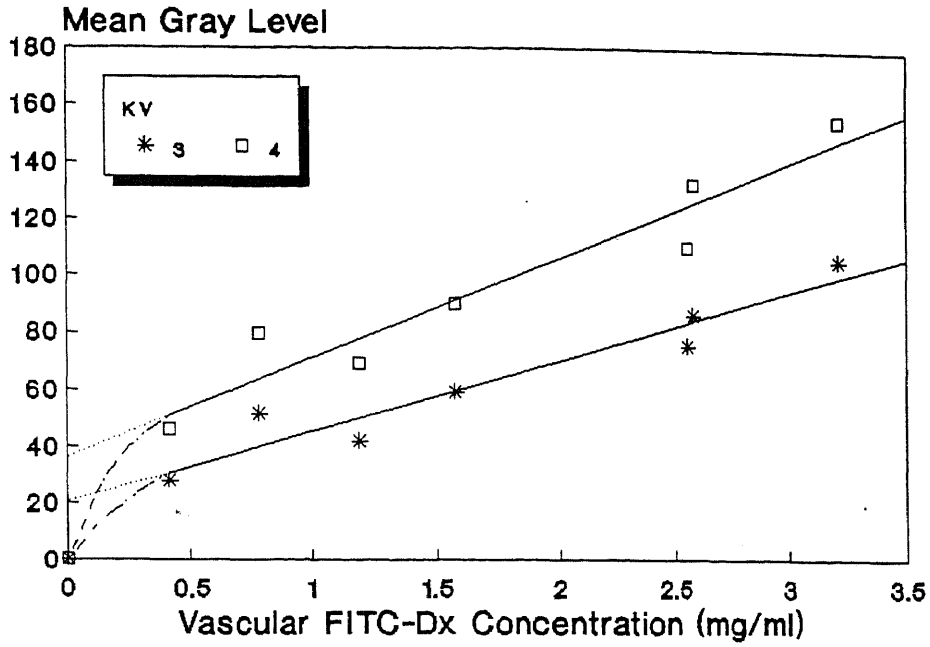

Figure D.3

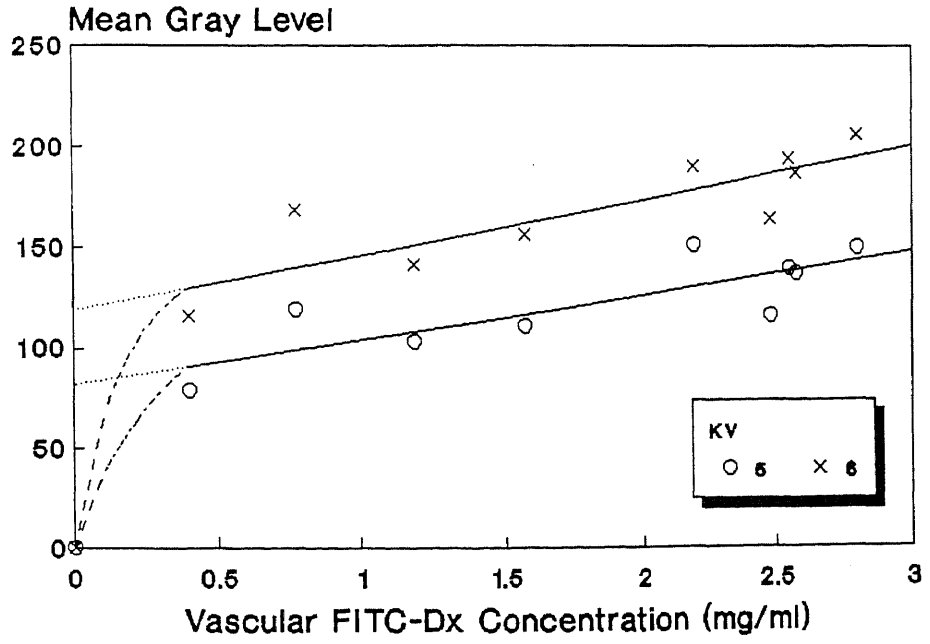

Figure D.4

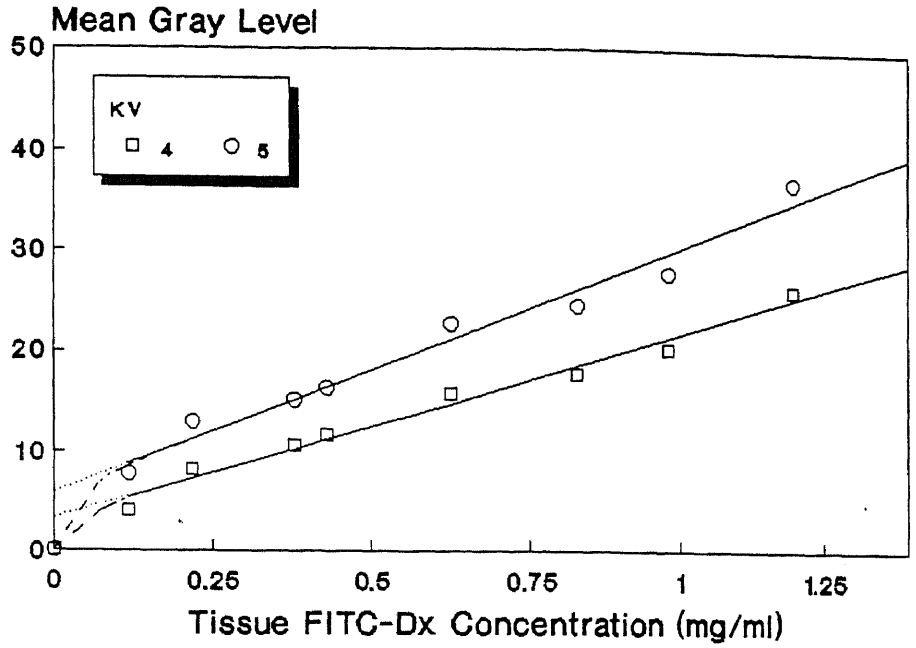

Figure D.5

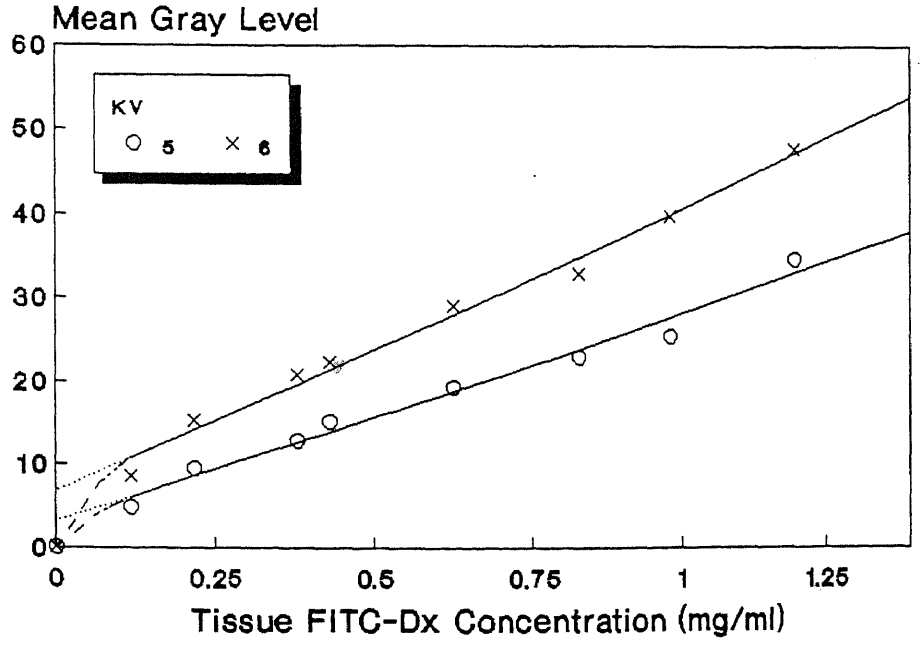

Figure D.6

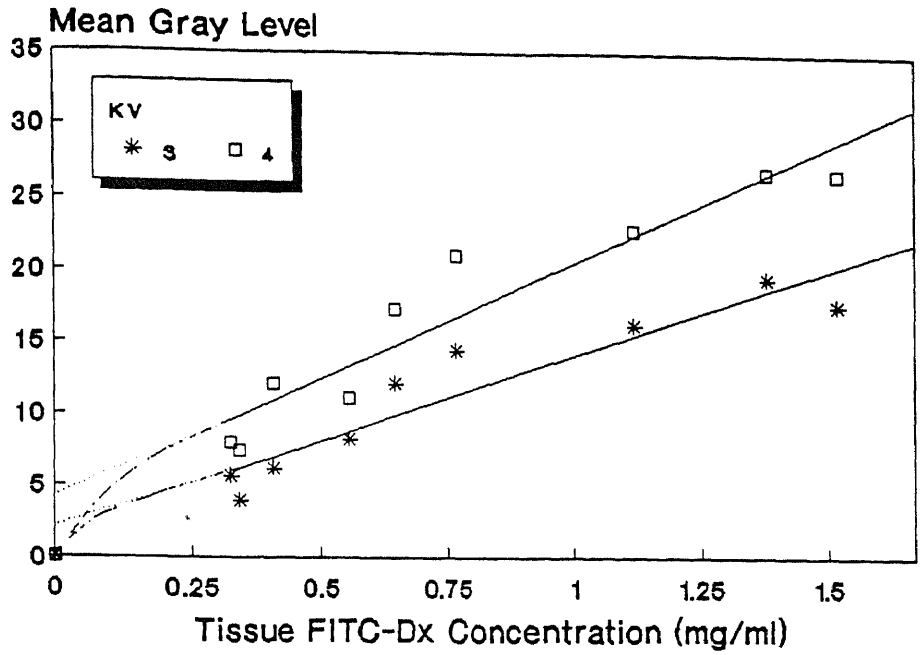

Figure D.7

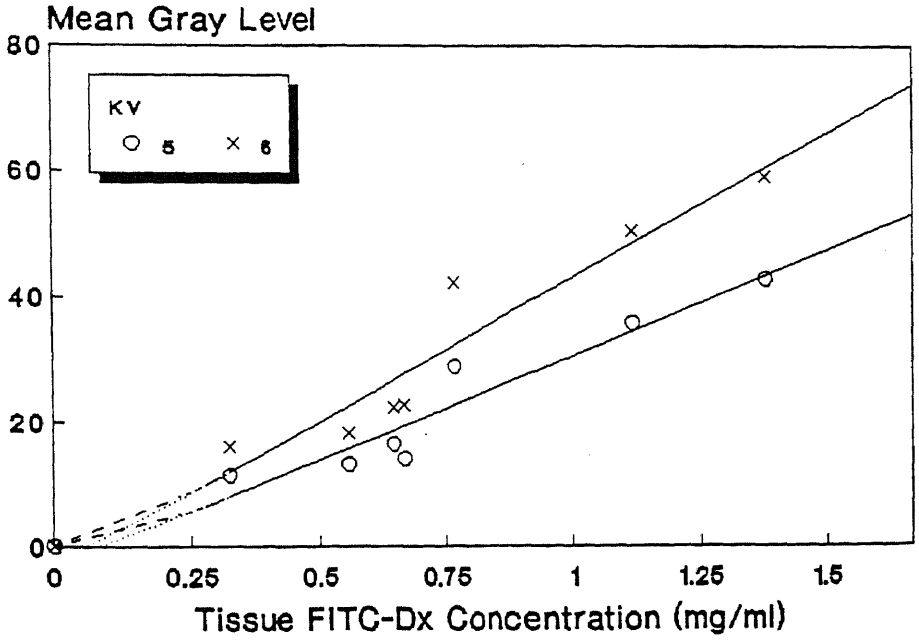

Figure D.8